UC Santa Barbara
UC Santa Barbara Electronic Theses and Dissertations

Title
Growth Optimization of III-N Electronic Devices by Plasma-Assisted Molecular Beam Epitaxy

Permalink
https://escholarship.org/uc/item/5f99w3p4

Author
AHMADI, ELAHEH

Publication Date
2015

Peer reviewed|Thesis/dissertation

eScholarship.org Powered by the California Digital Library
University of California

University of California
Santa Barbara

Growth Optimization of III-N Electronic Devices by Plasma-Assisted Molecular Beam Epitaxy

A dissertation submitted in partial satisfaction of the
requirements for the degree of Doctor of Philosophy

in Electrical and Computer Engineering

by

Elaheh Ahmadi

Committee in charge:
Professor Umesh k. Mishra, Chair
Professor James S. Speck
Professor Nadir Dagli
Professor Steve Denbaars
Professor Debdeep Jena
Dr. Stacia Keller

December 2015

The dissertation of Elaheh Ahmadi is approved:

James S. Speck

Nadir Dagli

Steve Denbaars

Debdeep Jena

Stacia Keller

Umesh Mishra, Chair

October 2015

Growth Optimization of III-N Electronic Devices by Plasma-Assisted Molecular Beam Epitaxy

Copyright 2015

by

Elaheh Ahmadi

Acknowledgments

I feel extremely grateful to Prof. Umesh K. Mishra for giving me the opportunity to work in his group. I am thankful to him for providing direction during my time in his group while offering me plenty of freedom in my daily research. Working under his supervision further ensured me that collaboration and working as a team is the only path to success. Beside being an excellent mentor, Umesh is a great person to seek advice from for personal problems.

I would like to thank prof. James S. Speck for providing me with the opportunity to collaborate with his group members. I am also grateful for the insightful conversations that I had with him during my PhD. Professor Dagli's excellent electromagnetic course was the first class I attended in the first quarter I started at UCSB. Although I had taken other Electromagnetic courses before, non of them taught me as deeply as his classes. I enjoyed every homework and exam problem that I solved in his classes. I am also thankful to Prof. Depdeep Jena for his great electron transportation course. I learnt the foundation for the 2DEG mobility calculations in his class. I would also like to thank my other committee members Prof. Steve Denbaars, and Dr. Stacia Keller for serving as my committee members. Specifically, I appreciate many fruitful discussions that I had with Stacia. Her enthusiasm for learning and understanding was always an inspiration to me.

I had the pleasure to have Dr. Man Hoi Wong as my mentor. Man Hoi taught me how to grow by MBE, and characterize by AFM and XRD. Unfortunately, Man Hoi left very soon after I joined Mishra's group. Dr. Stephen Kaun took over what Man hoi had started. Steve kindly and patiently answered all my questions about

growth and RHEED. He helped me to troubleshoot when my samples were not working. He also improved my writing skills by accurately editing my papers. I would like to acknowledge the other growers on GenII, Brian Mcskimming, Erin Kyle, and Karine Hestroffer, for sharing calibrations and helping with machine maintenance. Working with them made MBE openings (multiple of them) fun and memorable. I also learnt a lot from many fruitful discussions that I had with them about growth and characterization.

I am in awe of John English for all the work he did in the MBE lab to make sure that our growths proceed as smoothly as possible. He is the God of the MBE lab with a superpower that can heal every single problem that encounters to the MBE machine. I'd also like to thank Kurt Olsson for his help in the past year in keeping the MBE lab functioning.

The passion of my group-mates for learning made this journey much enjoyable. I was fortunate to work with many talented nice people in Mishra's group. I learnt a lot from discussions that I had with HEMT project members, Steve W., Brian R., Matt G., Xun, Haoran, and Karine. I am also grateful for the enjoyable discussions that I had with Trey, Geetak and Matt L. about HETs. Trey taught me temperature dependent IV measurements and analyzing diode IV curves. Geetak's optimism when our devices were not working constantly encouraged me to stride forward. I am thankful to Haoran and Cory for providing me with high quality MOCVD GaN templates. I also treasure fruitful discussions that I had with some former members of Mishra's group, Ramya, Shalini, Jing, Jeong (I hope I wrote your name correctly this time), Dan, Ajay, and Nick.

I would also like to thank Ravi shivaraman, and Dr. Feng Wu for performing

all the atom probe tomography and TEM experiments on my samples presented in this thesis.

Having great Persian friends at UCSB helped me to withstand being far from my home country. Specifically, I would like to thank Fateme, Mehran, Ali, Zahra, Amirali, Shahab, Marzie, Said D., Zeinab, Said Sh., Momo, and Mohammad for making my stay in Santa Barbara a memorable one.

I'd like to thank my parents for their unconditional love and support, and for instilling in me the passion for education. During these years they endured the fact that I could not travel to my home country to visit them, and in spite of all the difficulties for obtaining a US visa, they presented themselves at my defense to support me as they always would. I am also thankful to my brothers Amin and Mahdi for being my real trustworthy friends. Amin's eager in physics, and his passion for teaching fascinating physics phenomena in simplified language to Mahdi and I eventually implanted the seed of love for physics in our soul. I would also like to thank my sister in laws Marjan and Parinaz who have been as kind as real sisters to me.

Finally, I am deeply indebted to Hamidreza not just for being a great supportive husband, but also for being an exceptional mentor to me. He taught me almost everything I know about quantum mechanics and solid state today. He was the one who encouraged me to apply to top rank universities in the US, and specifically to UCSB. His passion for science and fervor for the excellence have been always an inspiration to me. I also thank my mother and father in law for raising such a kind, smart, and responsible man.

I dedicate this thesis to my best friend and love of my life, Hamidreza, without whom I would not be here today.

Curriculum Vitae

Education

University of California Santa Barbara, Santa Barbara, CA

PhD Candidate **Sep 2010 - Sep 2015**

- ▷ Electrical Engineering
- ▷ Thesis title: Growth optimization of III-N electronic devices by plasma-assisted molecular beam epitaxy

Sharif University of Technology, Tehran, Iran

Master of Science **Sep 2008 - Sep 2010**

- ▷ Electrical Engineering
- ▷ Thesis title: Cavity quantum electrodynamics in the ultrastrong coupling regime

Sharif University of Technology, Tehran, Iran

Bachelor of Science **Sep 2004 - Jul 2008**

- ▷ Electrical Engineering (Electronics)
- ▷ Thesis title: Physics and modeling of polaritonic devices

Honors and Awards

Nationwide University Entrance Exam for MSc Degree **May 2008**

▷ Ranked 75th among more than 18000 participants

Nationwide University Entrance Exam for BS Degree **May 2004**

▷ Ranked top 50 among more than 390000 participants

16th National Physics Olympiad, Tehran, Iran **Aug 2003**

▷ Bronze Medal

Publications

1. **E. Ahmadi**, D. J. Suntrup, C. Lund, J. S. Speck, U. K. Mishra, "Comparison of reverse leakage current in GaN Schottky diodes grown by plasma-assisted and ammonia molecular beam epitaxy" Submitted to Semiconductor science and Technology

2. G. Gupta, **E. Ahmadi**, K. Hestroffer, E. Acuna, and U.K. Mishra, *"Common Emitter current gain >1 in III-N Hot Electron Transistors with 7nm GaN-InGaN base,"* Electron Device Letters, IEEE,Â 36(5) (2015)

3. **E. Ahmadi**, F. Wu, H. Li, S. W. Kaun, M. Tahhan, K. Hestroffer, S. Keller, J. S. Speck, and U. K. Mishra, *"N-face GaN-AlN-GaN-InAlN and GaN-AlN-AlGaN-GaN-InAlN high-electron-mobility transistor structures grown by plasma-assisted molecular beam epitaxy on vicinal substrates,"* Semicond. Sci. Technol. 30 055012 (2015)

4. **E. Ahmadi**, H. Chalabi, S. W. Kaun, R. Shivaraman, J. S. Speck, and U. K. Mishra, *"Contribution of alloy clustering to limiting the two-dimensional*

electron gas mobility in AlGaN-GaN and InAlN-GaN heterostructures: Theory and experiment.," Journal of Applied Physics, 116(13) (2014)

5. S. W. Kaun, **E. Ahmadi**, B. Mazumdar, F. Wu, E. C. H. Kyle, P. G. Burke, U. K. Mishra, and J. S. Speck, *"GaN-based high-electron-mobility transistor structures with homogeneous lattice-matched InAlN barriers grown by plasma-assisted molecular beam epitaxy,"* Semicond. Sci. Technol. 29 045011 (2014)

6. **E. Ahmadi**, R. Shivaraman, F. Wu, S. Wienecke, S. W. Kaun, K. Hestroffer, S. Keller, J. S. Speck, U. K. Mishra, "Elimination of columnar microstructure in N-face InAlN, lattice-matched to GaN, grown by plasma-assisted molecular beam epitaxy in the N-rich regime." Applied Physics Letters 104 072107 (2014)

7. J. Lu, X. Zheng, M. Guidry, D. Denninghoff, **E. Ahmadi**, S. Lal, S. Keller, S. P. DenBaars, U. K. Mishra, *"Engineering the (In, Al, Ga) N back-barrier to achieve high channel-conductivity for extremely scaled channel-thicknesses in N-polar GaN high-electron-mobility-transistors,"* Applied Physics Letters 104 (9), 092107 (2014)

8. M. H. Wong, S. Keller, S. Dasgupta, Nidhi, D. J. Denninghoff, S. Kolluri, D. F. Brown, J. Lu, N. A. Fichtenbaum, **E. Ahmadi**, U. Singisetti, A. Chini, S. Rajan, S. P. DenBaars, J. S. Speck, U. K. Mishra, *"N-polar GaN epitaxy and high electron mobility transistors,"* Semiconductor Science and Technology 28 (7), 074009 (2013)

9. D. Denninghoff, J. Lu, **E. Ahmadi**, S. Keller, UK Mishra, *"N-polar GaN-InAlN-AlGaN MIS-HEMTs with 1.89 S/mm extrinsic transconductance, 4 A/mm drain current, 204 GHz f T and 405 GHz f max,"* Device Research Conference (DRC), 2013 71st Annual, 197-198 (2013)

10. D. Denninghoff, J. Lu, M Laurent, **E. Ahmadi**, S. Keller, UK Mishra, *"N-polar GaN-InAlN MIS-HEMT with 400-GHz fmax,"* Device Research Conference (DRC), 2012 70th Annual, 151-152 (2012)

11. **E. Ahmadi**, H. Chalabi, A. Arab, S. Khorasani, *"Cavity quantum electrodynamics in the ultrastrong coupling regime,"* Scientia Iranica, 18(3) (2011)

12. **E. Ahmadi**, H. Chalabi, A. Arab, S. Khorasani, *"Revisiting the Jaynes-Cummings-Paul model in the limit of ultrastrong coupling,"* SPIE OPTO, 79461W-79461W-6 (2011)

13. **E. Ahmadi**, H. Chalabi, M. Miri, M. Bayat, S. Khorasani, *"An analytical approach for evaluating the optical spectrum emitted from a strongly coupled single quantum dot photonic-crystal cavity system,"* Proceedings of the SPIE, Volume 7609, pp. 76090F-76090F-9 (2010)

Conference Presentations

1. **E. Ahmadi**, F. Wu, R. Shivaraman, K. Hestroffer, G. Gupta, M. Guidry, S. Keller, J. S. Speck, U. K. Mishra, *"Elimination of Columnar Microstructure in Lattice-Matched N-face InAlN-GaN Heterostructure Grown by Plasma*

Assisted Molecular Beam Epitaxy in N-rich Regime," ICNS conference, Washington DC, US (Aug 2013)

2. **E. Ahmadi**, S. W. Kaun, S. Keller, J. S. Speck, U. K. Mishra, *"The effects of dislocation, alloy disorder and electron-electron collision on the mobility of the two dimensional electron gas in AlGaN/GaN Heterostructures,"* MRS conference, Boston, MA, US (Dec 2013)

3. **E. Ahmadi**, K. Hestroffer, S. W. Kaun, M. Tahhan, H. Li, F. Wu, S. Keller, J. S. Speck, U. K. Mishra, *"N-face InAlN/AlN/GaN High Electron Mobility Transistors Grown by Plasma Assisted Molecular Beam Epitaxy ,"* ICMBE conference, Flag staff, AZ, US (Aug 2014)

4. **E. Ahmadi**, F. Wu, H. Li, S. W. Kaun, M. Tahhan, K. Hestroffer,S. Keller, J. S. Speck, and U. K. Mishra , *"N-face GaN-AlN-GaN-InAlN and GaN-AlN-AlGaN-GaN-InAlN high-electron mobility transistor structures grown by plasma-assisted molecular beam epitaxy on vicinal substrates ,"* CSW conference, Santa Barbara, CA, US (June 2015)

Abstract

Growth Optimization of III-N Electronic Devices by Plasma-Assisted Molecular Beam Epitaxy

by

Elaheh Ahmadi

Doctor of Philosophy in Electrical and Computer Engineering

University of California, Santa Barbara

Professor Umesh k. Mishra, Chair

InAlN has received significant attention due to its great potential for electronic and optoelectronic applications. In particular, $In_{0.18}Al_{0.82}N$ presents the advantage of being lattice-matched to GaN and simultaneously exhibiting a high spontaneous polarization charge, making $In_{0.18}Al_{0.82}N$ attractive for use as the barrier layer in high-electron-mobility transistors (HEMTs). However, in the case of InAlN growth by plasma-assisted molecular beam epitaxy (PAMBE), a strong non-uniformity in the in-plane In distribution was observed for both N-face and metal-face $In_{0.18}Al_{0.82}N$. This compositional inhomogeneity manifests itself as a columnar microstructure with AlN-rich cores (5-10 nm in width) and InN-rich intercolumn boundaries. Because of the large differences between the bandgaps and polarization of InN and AlN, this non-uniformity in InAlN composition could be a source of scattering, leading to mobility degradation in HEMTs. In this work, the growth conditions for high quality lattice-matched InAlN layers on free-standing GaN sub-

strates were explored by plasma-assisted molecular beam epitaxy (PAMBE) in the N-rich regime. The microstructure of N-face InAlN layers, lattice-matched to GaN, was investigated by scanning transmission electron microscopy and atom probe tomography. Microstructural analysis showed an absence of the lateral composition modulation that was previously observed in InAlN films grown by PAMBE. Using same growth conditions for InAlN layer, N-face GaN/AlN/GaN/InAlN high-electron-mobility transistors with lattice-matched InAlN back barriers were grown directly on SiC. A room temperature two-dimensional electron gas (2DEG) mobility of $1100\, cm^2V^{-1}s^{-1}$ and 2DEG sheet charge density of $1.9 \times 10^{13}\, cm^2$ was measured on these devices. However, the threading dislocation density (TDD) of GaN grown directly on SiC by PAMBE ($\approx 2 \times 10^{10}\, cm^{-2}$) is two orders of magnitude higher than GaN grown by MOCVD on SiC or sapphire ($\approx 5 \times 10^{8}\, cm^{-2}$). This high TDD can severely degrade the 2DEG mobility, especially at lower 2DEG sheet densities.

Relatively low TDD ($\approx 5 \times 10^{8}\, cm^{-2}$) on MOCVD-grown GaN substrates motivated us to study the growth of N-face GaN-based HEMT structures with InAlN backbarriers on such substrates. Since on-axis GaN-on-sapphire substrates with low threading dislocation density are not available in the N-face orientation, we explored the growth of InAlN on vicinal (4° miscut along GaN $10\bar{1}0$) GaN-on-sapphire substrates. The microstructure of $In_{0.18}Al_{0.82}N$ layers grown by PAMBE at different temperatures was studied using scanning transmission electron microscopy (STEM). The cross-sectional and plan-view STEM images revealed lateral variations in the InAlN composition along $10\bar{1}0$ (perpendicular to the step edges), in addition to step bunching in InAlN layers thicker than 10 nm. N-face HEMTs with

lattice-matched InAlN backbarriers were then grown on these vicinal substrates with different InAlN thicknesses.

Transmission line measurements showed that step bunching and lateral variation of InAlN composition degraded the 2DEG mobility in the directions parallel and perpendicular to the steps. A 2DEG charge density of $1.1 \times 10^{13}\, cm^{-2}$ and mobility of $1850\, cm^2V^{-1}s^{-1}$ were achieved on a GaN/AlN/InAlN/GaN structure with 7.5 nm thick $In_{0.18}Al_{0.82}N$. By designing a double backbarrier ($In_{0.18}Al_{0.82}N$(7.5 nm)/$Al_{0.57}Ga_{0.43}N$(7 nm)), a 2DEG charge density of $2 \times 10^{13}\, cm^{-2}$ and mobility of $1360\, cm^2V^{-1}s^{-1}$ were attained, which resulted in a sheet resistance of $230\, \Omega/\square$.

Two good measures of the device quality concerning the power loss in power switch and high frequency switch applications are Huang material figure of merit , and Baliga high-frequency figure of merit, respectively, which shows that for any fixed material system, power loss reduces by increasing the mobility of the 2DEG. Therefore, it is very important to understand the source of scattering mechanisms which affect the 2DEG mobility. In this work, we studied effect of decreasing channel thickness or increasing gate reverse bias on charge density and 2DEG mobility in N-face HEMT structure. Our calculations showed that increasing the gate reverse bias and decreasing the channel thickness both reduce the 2DEG mobility. This trend has been observed by experiment as well. Previously, it was believed that increasing the gate reverse bias or decreasing the channel thickness in N-face GaN-based HEMT structures lead to deeper penetration of the 2DEG wavefunction into the barrier, and consequently, higher interface roughness and alloy scattering rates. Although this statement is true, our calculations revealed that the penetration of the 2DEG into the barrier and, therefore, 2DEG mobility limited by

alloy and interface roughness scattering mechanisms do not vary significantly by increasing gate reverse bias or decreasing the channel thickness. therefore, these two scattering mechanisms are not enough to explain the significant drop in the 2DEG mobility observed in experiments. We believe that the charged trap states at the AlGaN-GaN interface, where the 2DEG forms, are responsible for this 2DEG mobility reduction.

Contents

List of Figures xix

List of Tables xxiv

1 Introduction **1**
- 1.1 Material properties of III-N . . . 1
- 1.2 Alloys . . . 5
- 1.3 Polarization . . . 7
- 1.4 Heterostructures . . . 8
- 1.5 Molecular beam epitaxy . . . 9
- 1.6 Synopsis of dissertation . . . 12

2 N-Face HEMT Structures With InAlN as the Backbarrier **14**
- 2.1 Introduction . . . 14
- 2.2 Growth of Homogeneous Lattice-matched InAlN on Free-standing GaN Substrates . . . 19
- 2.3 Protective thin GaN cap on InAlN . . . 25
- 2.4 N-face HEMT structures with InAlN backbarrier on SiC . . . 28
- 2.5 Improvement of the quality of AlN layer using Ga as surfactant . . . 32
- 2.6 Summary . . . 36

3 Growth of Lattice-matched InAlN on vicinal substrates **38**
- 3.1 Introduction . . . 38
- 3.2 Growth and measurement instrumentation . . . 39
- 3.3 HEMT structures with InAlN as the backbarrier . . . 40
- 3.4 Variation of InAlN growth conditions . . . 45
- 3.5 HEMT Structures with Double Backbarriers . . . 47
- 3.6 Summary . . . 49

4 Modeling of 2DEG mobility in HEMT structures **51**
- 4.1 Introduction . . . 51
- 4.2 Procedure . . . 53
- 4.3 Conventional Scattering mechanisms . . . 57
  - 4.3.1 Phonon scattering . . . 57
  - 4.3.2 Ionized background impurity . . . 60
  - 4.3.3 Interface roughness . . . 62

4.3.4 Alloy disorder 64
4.3.5 Remote ionized impurity 66
4.3.6 2DEG mobility considering only conventional scattering mechanisms 67
4.4 Surface state dipoles 68
4.5 Charged interface states at the AlGaN-GaN interface 71
4.6 Total 2DEG mobility and conclusion 74

5 Alloy Clustering Scattering **77**
5.1 Introduction 77
5.2 Derivation 79
5.3 Atom probe tomography analysis 86
5.4 Simulation 87
5.5 Summary 91

6 Analysis of reverse-bias leakagein GaN Schottky diodes **92**

Bibliography **105**

List of Figures

1.2 GaN WZ crystal structure in (a) Ga-face (b)N-face polarizations, showing the spontaneous polarization vector. 2
1.1 Important planes and their corresponding directions in GaN WZ crystal structure[1]. 2
1.3 In-plane lattice constant and bandgap for GaN, InN, AlN and their alloys. Bowing factors of 1, 1.43, and 3.1 have been assumed for calculating the bandgap of AlGaN, InGaN, and InAlN, respectively. 6
1.4 Band diagram of an AlGaN/GaN heterostructure along with polarization charges, and 2DEG formed at the AlGaN-GaN interface. . . 9
1.5 (a) Schematic and (b) Band diagram of an InGaN dipole diode. The polarization dipole introduced by the thin (4nm-thick) InGaN layer pulls up the conduction band in GaN and forms a barrier. 10
1.6 Schematic of a PAMBE machine, showing Knudsen effusion cells and rf plasma source for providing active N. 11

2.1 Plan-view electron micrographs of $In_{0.175}Al_{0.825}N$ showing lateral composition modulation in form of honeycomb microstructure with AlN-rich cores and InN-rich intercolumn boundaries[2]. 15
2.2 Schematic showing the growth dynamics resulting in composition modulation. (a) The growth starts with AlN rich platelets because of low mobility of Al adatoms on the surface, and high rate of In desorption from the surface. (b) In prefers to incorporate along the coalescence edges because of the tnsile stress. (c) columnar microstructures with AlN-rich cores and InN-rich intercolumn boundaries forms[3]. 17
2.3 In III-site distribution taken using APT in a plane perpendicular to the growth direction. The InN mole fraction changes from 8% in the cores to 38% along the intercolumn boundaries[4]. 18
2.4 AFM images of InAlN layers grown at substrate temperature of (a) 480 °C (b) 500 °C (c) 520 °C. 20
2.5 Schematic of InAlN/GaN/AlN/GaN heterostructures grown on N-face free-standing (FS) GaN for structural studies 21
2.6 HAADF image of the InAlN showing a uniform contrast. TEM performed by Feng Wu. 22

2.7 Proxigram map across the GaN/AlN/InAlN interfaces (b) 2D compositional map of In in plane perpendicular to growth direction (c) APT reconstruction of InAlN layer on N-face GaN by PAMBE. APT performed by Ravi Shivaraman. 24
2.8 AFM image of samples grown to study the necessity of having a thin GaN on InAlN before heating up substrate to grow the other following layers in the structure. (a) Sample A: 10 nm of InAlN was grown at 550 °C. The growth was stopped right after InAlN, and the substrate was cooled down. (b) Sample B: 10 nm of InAlN was grown at 550 °C. A Ga wet later was maintained on the surface during heating up substrate to 700 °C for 10 minutes. We made sure that the excess Ga is desorbed from the surface before cooling down the substrate. (c) Sample C: 10 nm of InAlN was grown at 550 °C. Then, the sample was heated up to 700 °C for 10 minutes without any protection, and then cooled down. 27
2.9 Schematic of InAlN/GaN/AlN/GaN HEMT structure grown on C-face SiC for 2DEG mobility studies and HEMT fabrication. There is a Si delta-doped with 1.5×10^{19} cm^{-3} concentration at the back of barrier. 29
2.10 Representative (a)5×5 µm^2 and (b) 2×2 µm^2 AFM images of the HEMT structure grown on C-face SiC as shown in Fig.2.9. The surface has a flower-like morphology with an rms roughness of 0.9 nm in a 2×2 µm^2 area. 30
2.11 (a) DC current-voltage (IV) and (b) Extrinsic conductance as a function of gate voltage for different Drain voltages measured on of the HEMT structure shown in Fig. 2.9 31
2.12 200 ns (filled circles) and 80 ns (filled triangular) pulsed current and DC current (lines) for a HEMT with a nominal gate length of 0.7 µm, a gate-source spacing of 0.5 µm, and a gate-drain spacing of 2 µm, measured (a) in dark (b) under UV. Measurements performed by Matthew Guidry. 32
2.13 Schematic of InAlN/GaN/AlN/GaN HEMT structure grown on C-face SiC for 2DEG mobility studies and HEMT fabrication purpose. The buffer is C-doped to compensate the unintentionally incorporated donors (oxygen). 33
2.14 Temperature dependence of the 2DEG mobility and sheet charge density for GaN/AlN/GaN/InAlN HEMT structure grown on C-face of SiC. 34
2.15 (a) DC current-voltage (IV) measurement of the GaN/InAlN/GaN/AlN/GaN HEMT grown on C-face SiC substrate. (b) Extrinsic conductance as a function of gate voltage for different Drain voltages measured on the GaN/InAlN/GaN/AlN/GaN HEMT grown on C-face SiC substrate. 35
2.16 RF Gm and DC Gm measured for a HEMT with gate width and length of 100 µm and 0.7 µm, respectively, and L_{gs} and L_{gd} of 0.3 µm and 1 µm, respectively. 36

3.1 (a) Schematic of N-face GaN/AlN/GaN/InAlN/GaN HEMT structures grown on vicinal GaN-on-sapphire substrates with 4° miscuts along GaN< $10\bar{1}0$ >, showing substrate temperatures (T_{sub}). The growth was interrupted twice. During the first interruption, the substrate temperature was decreased before growth of InAlN layer. During the second interruption, the substrate temperature was increased to grow the AlN interlayer and the GaN channel. (b) Band diagram of the structure shown in part (a) with a 10-nm-thick InAlN layer. 42
3.2 STEM images of (a) 7.5-nm-thick and (b) 25-nm-thick InAlN layers in N-face GaN/AlN/InAlN/GaN HEMT structures grown on vicinal GaN-on-sapphire substrates. 42
3.3 AFM images of InAlN layers grown at substrate temperatures of (a) 630 °C, (b) 600 °C, (c) 570 °C, and (d) 550 °C with fixed In and Al BEPs. The sample grown at 630 °C was cracked due to excess tensile stress in the AlN layer. 44
3.4 (a) cross-sectional STEM of the a-plane reveals InAlN composition variation in the lateral direction and step-bunching. As demonstrated in the inset, the fluctuations in the composition originate from the step edges and move toward the surface. (b) Cross-sectional STEM of the m-plane reveals uniform composition along m planes. TEM performed by Feng Wu. 46
3.5 Plan-view STEM shows that the Al-rich regions form along GaN < $11\bar{2}0$ > in meandering lines. TEM performed by Feng Wu. . . . 47
3.6 (a) Schematic of N-face GaN/AlN/AlGaN/GaN/InAlN/GaN HEMT structures grown on vicinal GaN-on-sapphire substrates with 4° miscuts along GaN < $10\bar{1}0$ >, showing substrate temperatures (T_{sub}). The growth was interrupted three times. During the first interruption, the substrate temperature was decreased before growth of InAlN layer. During the second interruption, the substrate temperature was increased to grow the AlGaN barrier. During the third interruption, the Al cell temperature was increased to grow the following AlN interlayer. (b) Band diagram of the structure shown in part (a) with 3-nm-thick AlGaN layer. 48

4.1 (a) Schematic and (b) band diagram of a typical N-face HEMT structure with AlGaN as the backbarrier. All the 2DEG mobility calculations shown in this chapter were performed for this structure. 54
4.2 (a) 2DEG wavefunction along with the band diagram near the channel, and (b) charge density for the HEMT structure shown in Fig. 4.1a for different reverse biases applied to the gate. 56
4.3 (a) 2DEG wavefunction along with the band diagram near the channel, and (b) charge density for the HEMT structure shown in Fig. 4.1a for different channel thicknesses. 57
4.4 2DEG mobility limited only by acoustic deformation potential scattering at room temperature in N-face HEMT structure shown in Fig. 4.1a for (a) different gate voltages, and (b) channel thicknesses . . 59

4.5 2DEG mobility limited only by background ionized impurity scattering at room temperature for a background impurity concentration of 3×10^{16} cm^{-3} in N-face HEMT structure shown in Fig. 4.1a for (a) different gate voltages, and (b) channel thicknesses 61
4.6 2DEG mobility limited by Interface roughness scattering at room temperature, assuming $\Delta = 0.5$ nm and $L = 15$nm, in N-face HEMT structure shown in Fig. 4.1a for (a) different gate voltages, and (b) channel thicknesses. 63
4.7 Probability of 2DEG penetration into the alloy barrier in the N-face HEMT structure shown in Fig. 4.1a for (a) different gate biases (b) different channel thicknesses 65
4.8 2DEG mobility limited by alloy scattering at room temperature in N-face HEMT structure shown in Fig. 4.1a for (a) different gate voltages, and (b) channel thicknesses 66
4.9 2DEG mobility limited by remote ionized impurity at room temperature in N-face HEMT structure shown in Fig. 4.1a for (a) different gate voltages, and (b) channel thicknesses. 68
4.10 2DEG mobility at room temperature, calculated considering all conventional scattering mechanisms as a function of (a) gate reverse bias (b) channel thickness. 69
4.11 Schematic of a typical N-face HEMT structure showing the SiN dielectric and surface state dipoles. 70
4.12 2DEG mobility limited by surface state dipoles at room temperature in N-face HEMT structure shown in Fig. 4.1a for (a) different gate voltages, and (b) channel thicknesses. 71
4.13 The Band diagram of N-face HEMT structure showing interface trap state at the AlGaN-GaN interface 72
4.14 2DEG mobility limited by AlGaN-GaN interface states at room temperature in N-face HEMT structure shown in Fig. 4.1a for (a) different gate voltages, and (b) channel thicknesses. 73
4.15 2DEG mobility limited by the charged interface states scattering as a function of interface state density. 74
4.16 2DEG mobility in N-face HEMT structure shown in Fig[fig:HEMT-structure] for (a) different gate voltages, and (b) channel thicknesses. 76

5.1 (a) Band structure of an AlGaN/GaN heterostructure showing the fluctuations in barrier height as a result of fluctuations in the barrier composition. (b) Schematic of ground state fluctuations along the channel. The Fermi level is assumed to be pinned at the surface and is constant along the channel. 80
5.2 To obtain a significant number of sampling points, a 60×60 nm^2 in-plane composition map was generated by combining four 30×30 nm^2 composition maps extracted from different regions in the AlGaN layer 81

5.3 (a) 2D III-site composition map of the in-plane Al distribution in an $Al_{0.15}Ga_{0.85}N$ layer (Black arrows illustrate the directions along which the AC lengths were calculated). (b) AC sequence of digitized data shown in part (a). (c) An example of the power spectrum calculated using both the FFT and AR methods and the fitted Gaussian function. (d) Histogram of AC lengths obtained from different areas on the 2D III-site composition map. 82
5.4 Ground state energy of the 2DEG as a function the alloy composition calculated using BandEng for (a) $Al_{0.27}Ga_{0.73}N$/GaN and (b) $In_{0.18}Al_{0.82}N$/GaN. 83
5.5 Plot of the mobility limited only by alloy clustering in the barrier as a function of the mean amplitude of fluctuations in mole fraction (Δ) for various cluster sizes. This limit is independent of temperature. 86
5.6 Comparison of the effect of alloy clustering on the mobility of 2DEG between AlGaN/GaN and InAlN/GaN heterostructures. The x-axis is the mean amplitude of fluctuations in mole fraction. 88
5.7 Plot of 2DEG mobility limited by alloy clustering as a function of the mean amplitude of fluctuations in mole fraction (Δ) for different AlN interlayer thicknesses in InAlN/AlN/GaN structures. 91

6.1 Growth rate of GaN versus Ga flux for calibration samples grown by PAMBE. The Ga flux needed to achieve stoichiometry at 700 °Cwas determined from this curve to be around 2.2×10^{-7}. 95
6.2 Schematic of the Schottky diode device structure. The ohmic and Schottky metal stacks are also shown. 96
6.3 AFM images of samples grown by PAMBE. (a) PA-A (b) PA-B (c) PA-C (d) PA-D. 96
6.4 AFM images of samples grown by ammonia MBE. (a) NH_3-A (b) NH_3-B 98
6.5 Average leakage current at -5 V. The error bars show the variation of leakage current over 16 devices for each sample. 101
6.6 10 kV panchromatic Cathodoluminescence (CL) images taken on a Lumilog FS GaN substrate showing the non-uniform distribution of the dislocation density. 101
6.7 Current-voltage curves on diodes fabricated on the Schottky structure grown on Lumilog FS GaN, illustrating the variation in the reverse current from diode to diode. The idieality factor of these diodes was 1.02 at room temperature. 103

List of Tables

1.1 matieral properties along with two important figure of merits for measuring the suitability of semiconductors for high-power applications. 4
1.2 lattice parameters for III-nitrides in WZ crystal structures 5
1.3 Spontaneous polarization, piezoelectric constants, and elastic constants for GaN, InN, and AlN. 8

2.1 Ga, In, and Al surface concentrations measured by XPS on three InAlN samples. Sample A was cooled down right after growing InAlN layer. Sample B was protected with Ga wet layer while increasing substrate temperature to 700 °C for 10 minutes. Sample C had no protection while increasing substrate temperature to 700 °C for 10 minutes. 26
2.2 2DEG Charge density, mobility, and sheet resistance in N-face HEMT structures with $In_{0.18}Al_{0.82}N$ as backbarrier grown on C-face SiC. . . 30

3.1 Charge density (n_s), mobility ($\mu_{||}$, $\mu_{\perp}$), and sheet resistance ($R_{,||}$, $R_{,\perp}$) in parallel and perpendicular directions to the steps in N-face GaN/AlN/GaN/InAlN/GaN HEMT structures with different InAlN layer thicknesses grown on vicinal GaN template. 43
3.2 Charge density (n_s), mobility ($\mu_{||}$, $\mu_{\perp}$), and sheet resistance ($R_{,||}$, $R_{,\perp}$) in parallel and perpendicular directions to the steps in N-face GaN/AlN/AlGaN/GaN/InAlN/GaN HEMT structures with different AlGaN layer thicknesses grown on vicinal GaN template. . . . 49

5.1 Materials parameters used in BandEng to calculate the ground state energy. m_e^*/m_e is the ratio of the electron effective mass to the electron mass. E_g, ΔE_c, and ε_r are bandgap, conduction band discontinuity with respect to GaN, and the relative permittivity, respectively. 89

6.1 List of all samples showing Ga flux (Φ_{Ga}), ammonia flow rate, substrate temperature (T_{sub}), substrate TDD, and rms roughness value (r_{rms}). 99

Chapter 1

Introduction

1.1 Material properties of III-N

Crystalline III-Nitrides exist in both wurtzite (WZ) and zinc blende (ZB) structures. Wurtzite is the thermodynamically stable crystal structure for III-nitrides in ambient condition, and is of the interest of this work. This crystal structure has a hexagonal unit cell with two lattice parameters a, and c. There are three important planes in wurtzite nitrides which are of special interest, and called (0001) c-plane, $(11\bar{2}0)$ a-plane, and $(1\bar{1}00)$ m-plane. These three planes with their associated directions are shown in Fig. 1.1.

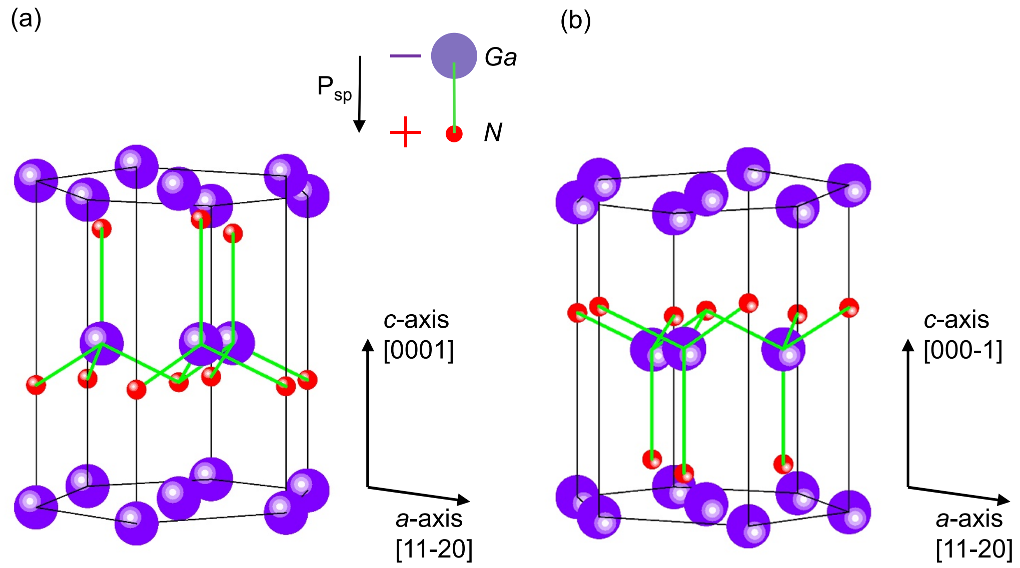

Figure 1.2: GaN WZ crystal structure in (a) Ga-face (b)N-face polarizations, showing the spontaneous polarization vector.

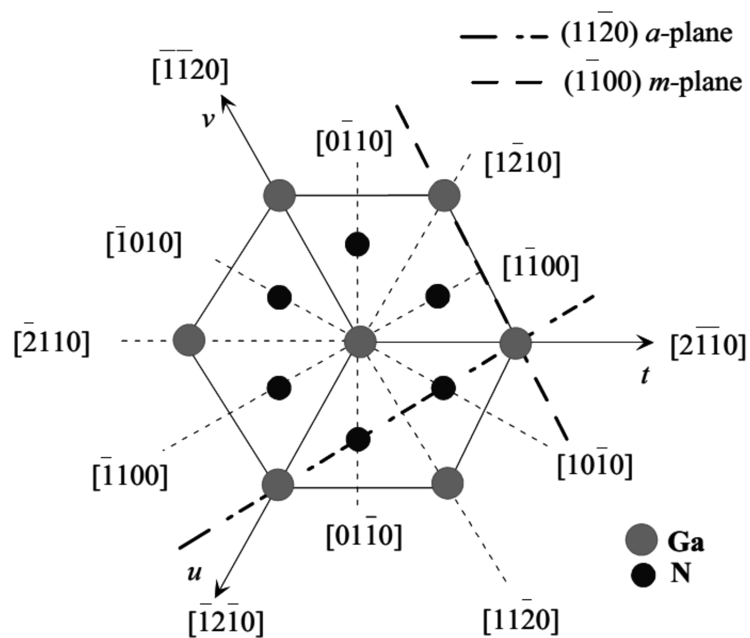

Figure 1.1: Important planes and their corresponding directions in GaN WZ crystal structure[1].

Because of lack of inversion symmetry, WZ III-nitrides exhibit unique polarization effects. Depending on the surface termination III-nitrides have either a group III element (Al, In, Ga) polarity (0001)or a N-polarity ($000\bar{1}$). This is demonstrated in Fig. 1.2. Moreover, they show piezoelectric effects when strained along c-direction. The piezoelectric and spontaneous polarization charges play an important role in designing device structures, and provide us with an extra nob for band diagram engineering. Some interesting examples of this band diagram engineering have been utilized throughout this work for designing high electron mobility transistors (HEMTs) and hot electron transistors (HETs).

GaN and its alloys with InN and AlN have arisen a great deal of interest in last two decades because of their wide range of direct band gap[5, **?**, 6, 7]. This makes them suitable for optoelectronic applications such as laser diodes (LDs)[8, 9, 10, 11], and light emitting diodes (LEDs)[12, 13, 14].

Besides, GaN has a large potential for high power electronics. Because of its high breakdown electric field in addition to high electron saturation velocity, GaN is a great candidate for high-power amplifiers and switches[15, 16, 17]. Johnson figure of merit (JFOM) and Baliga figure of merit (BFOM) are the two most referred figure of merits for measuring the suitability of semiconductors for high-power applications. These two figure of merits along with some other important material properties are shown in table 1.1 for different semiconductors. High FJFOM and BFOM numbers for GaN in comparison with the other semiconductors makes it a promising material system for fabricating high power electronic devices. Although, SiC has breakdown field, and electron saturation velocity nearly close to GaN, it does not provide the same flexibility for designing different kinds of transistors. In

	Si	GaAs	GaP	4H-SiC	Diamond	GaN	AlN
E_G (eV)	1.1	1.4	2.3	3.2	5.5	3.4	6.2
Thermal conductivity ($Wcm^{-1}K^{-1}$)	1.5	0.5	1.1	4.9	20	1.3	3.9
Melting point (K)	1683	1513	1740	2830	3773	2791	3273
Electron saturation velocity (10^7 cm s^{-1})	1	2	1.25	2	2.7	2.5	1.4
Electron mobility ($cm^2V^{-1}s^{-1}$)	1400	8500	350	950	2200	1000	135
Hole mobility ($cm^2V^{-1}s^{-1}$)	600	400	100	120	1600	30	14
Dielectric constant	11.8	12.5	11.1	9.7	5.5	8.9	8.5
Breakdown field (10^5V cm^{-1})	3	6	10	20	100	26	20
JFOM ratio to Si	1	0.93	-	14	-	17	-
BFOM ratio to Si	1	16	-	430	-	990	-

Table 1.1: matieral properties along with two important figure of merits for measuring the suitability of semiconductors for high-power applications.

	GaN	InN	AlN
a_0	0.3189	0.3548	0.3112
c_0	0.51	0.5760	0.4982

Table 1.2: lattice parameters for III-nitrides in WZ crystal structures

contrast, GaN and its alloys with AlN and InN give the possibility of designing complicated heterostructures suitable for HEMTs, HETs and HBTs. Moreover, the possibility of growing GaN-based electronic structures on SiC substrates, which have excellent thermal conductivity, offers another advantage for this material system to be used in power electronics. Fabricating power electronic devices on substrates with high thermal conductivity significantly reduces the amount of material needed as heat sink for cooling purposes, which helps in decreasing the total cost in addition to size of power electronic devices.

1.2 Alloys

Integrating GaN with (AlInGa)N alloys gives a wide space for designing electronic device structures. In this section we briefly discuss the dependence of lattice parameters, bandgap, and polarization parameters on the composition of III-nitride ternary alloys. Lattice parameters of AlN, InN and GaN are listed in table 1.2.

Lattice parameters for III-nitride ternary alloys can be approximated using Vagard's law as shown in Eq. 1.1. In this equation A and B are two different metal elements out of Al, Ga or In.

$$a_{A_xB_{(1-x)}N} = a_{AN}x + a_{BN}(1-x),\ c_{A_xB_{(1-x)}N} = c_{AN}x + c_{BN}(1-x) \tag{1.1}$$

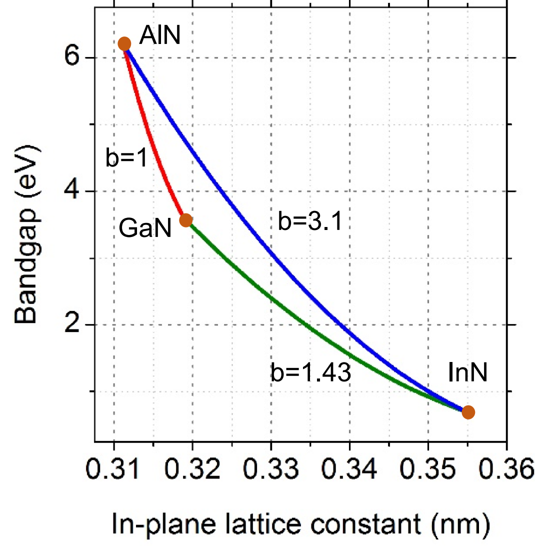

Figure 1.3: In-plane lattice constant and bandgap for GaN, InN, AlN and their alloys. Bowing factors of 1, 1.43, and 3.1 have been assumed for calculating the bandgap of AlGaN, InGaN, and InAlN, respectively.

Bandgap of the ternary alloy $A_xB_{(1\text{-}x)}N$ can be calculated using Eq. 1.2, if the bowing factor (b) is known accurately.

$$E^g_{A_xB_{(1-x)}N} = xE^g_{AN} + (1-x)E^g_{BN} - bx(1-x) \tag{1.2}$$

There is discrepancy among bowing parameters suggested by experimental data in literature. This discrepancy is more severe for InGaN and InAlN alloys. This is because growth of high-quality InN, and, therefore, extracting its physical properties has been challenging. Moreover, the disparity between In and Al/Ga can lead to issues such as phase separation in InGaN or InAlN. In-plane lattice constant

for GaN, InN, AlN and their alloys along with their bandgap are shown in Fig1.3. The least square fit to experimental data gives bowing factors of 1 eV, 3.1 eV, and 1.43 eV for AlGaN, InAlN, and InGaN, respectively[1].

1.3 Polarization

For III-nitrides and their alloys, because of the difference in the electronegativity of metal atom and N atom, there is a local spontaneous polarization along each III-N bond. In an ideal WZ lattice structure, where $c_0/a_0 = 1.633$, the polarization vectors cancel out each other, and the net polarization in the lattice is zero. However, in AlN, GaN, InN, and their alloys, this ratio is deviating from the ideal value, and there is a net spontaneous polarization along $\overrightarrow{c}$ direction. Furthermore, tensile or compressive stress in the lattice produces additional polarization called piezoelectric polarization. Therefore, the net polarization in each layer is the sum of spontaneous and piezoelectric polarizations. Piezoelectric polarizations in directions $\overrightarrow{a}$, and $\overrightarrow{m}$ are zero, and in direction $\overrightarrow{c}$ can be calculated using the following equation:

$$P_z = 2\frac{a - a_0}{a_0}\left(e_{31} - e_{33}\frac{C_{13}}{C_{33}}\right) \tag{1.3}$$

Where a_0, and a are the in-plane lattice parameters of the epitaxial layer when it is strained to the buffer layer (buffer in-plane lattice constant), and when it is relaxed, respectively. e_{31} and e_{33} are the electric piezoelectric coefficients, and C_{13} and C_{33} are the elastic coefficients. The value of aforementioned parameters are listed in table 1.3 for AlN, InN, and GaN. These values can be estimated for

	P_{sp} (C/m^2)	e_{31} (C/m^2)	e_{33} (C/m^2)	C_{13} (10^{12} N/m^2)	C_{33} (10^{12} N/m^2)	E_g(eV)
GaN	-0.029	-0.49	0.73	1.03	3.55	3.4
AlN	-0.081	-0.6	1.46	1.08	3.95	6.0
InN	-0.032	-0.57	0.97	0.96	2.58	0.7

Table 1.3: Spontaneous polarization, piezoelectric constants, and elastic constants for GaN, InN, and AlN.

ternary alloys using a linear combination of their components.

1.4 Heterostructures

Heterostructure is a combination of two or more crystalline semiconductors with different bandgaps, which is, nowadays, an essential part of electronic and optoelectronic device structures. Use of growth techniques such as MBE or MOCVD, by which abrupt interfaces can be achieved, is necessary for fabricating heterostructures.

III-N heterostrcutures are unique in the sense that not only bandgap, but also the polarization changes at the interface of the heterojunction. This gives extra space for designing electronic device structures such as HEMTs, HETs or BJTs. For example, as opposed to conventional semiconductor HEMTs, there is no need for remote doping in III-N HEMTs to provide two dimensional electron gas (2DEG) in the channel. An AlGaN/GaN heterostructure along with its band diagram and the polarization charges are shown in Fig. 1.4. Discontinuity in the polarization

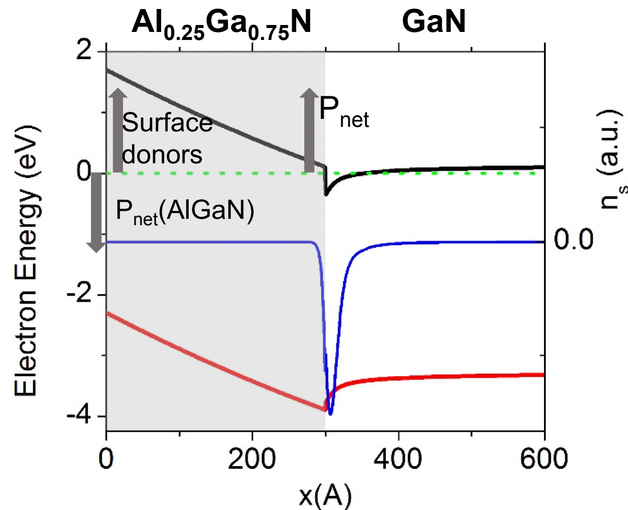

Figure 1.4: Band diagram of an AlGaN/GaN heterostructure along with polarization charges, and 2DEG formed at the AlGaN-GaN interface.

results in a non-zero polarization charge at the interface, and a 2DEG charge, consequently, to satisfy charge neutrality. Donor states at the surface are the source of 2DEG electrons in the channel[18].

Polarization dipole barrier is the other example of using heterostructures in electronic device structures. An example of a polarization dipole is shown in Fig. 1.5. The polarization dipole introduced by 4nm-thick InGaN pulls up the conduction band in GaN, and forms a barrier. This kind of barrier is used in designing HET structures discussed in chapter 6.

1.5 Molecular beam epitaxy

Epitaxial growth of GaN was very challenging for years because of the fact that it needed to be grown on foreign substrates with large lattice mismatches. In 1969, Maruska and Tietjan were able to grow poly-crystalline GaN for the first time

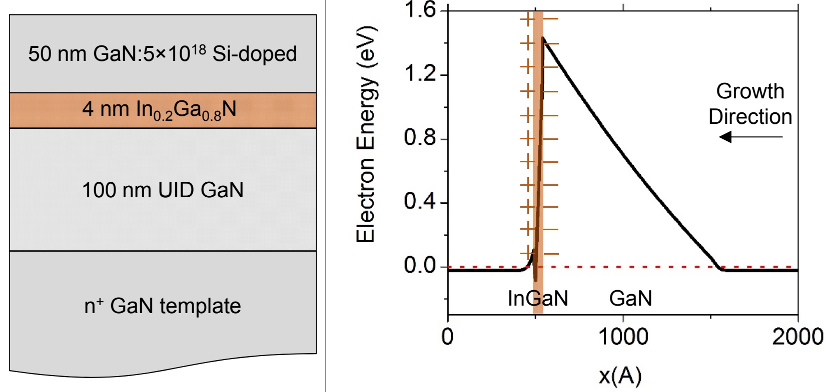

Figure 1.5: (a) Schematic and (b) Band diagram of an InGaN dipole diode. The polarization dipole introduced by the thin (4nm-thick) InGaN layer pulls up the conduction band in GaN and forms a barrier.

using hydride vapor-phase epitaxy[19]. In 1986, using low temperature AlN as the buffer layer, Amano *et al.* succeeded in growing mirror-like GaN on sapphire with relatively low residual impurity concentration ($\sim 1 \times 10^{17}$cm^{-3}) by metal-organic chemical vapor deposition (MOCVD)[20]. Later Nakamura et al.[13] achieved high quality GaN grown on sapphire by MOCVD using low temperature GaN instead of AlN as the buffer layer.

Nowadays, MBE and MOCVD are two common growth techniques which are used widely for epitaxial growth of III-nitirdes. Both these two techniques give us the ability to control the layer thickness with a resolution of few angstroms. The facts that much higher growth rates are achievable by MOCVD in comparison with MBE, and that the machine maintenance is considerably cheaper for the former one make this growth technique the preferred one in industry. Regardless, MBE offers remarkable advantages over MOCVD specially interesting for research purposes.

MBE is an ultra high vacuum growth technique, which allows the use of reflec-

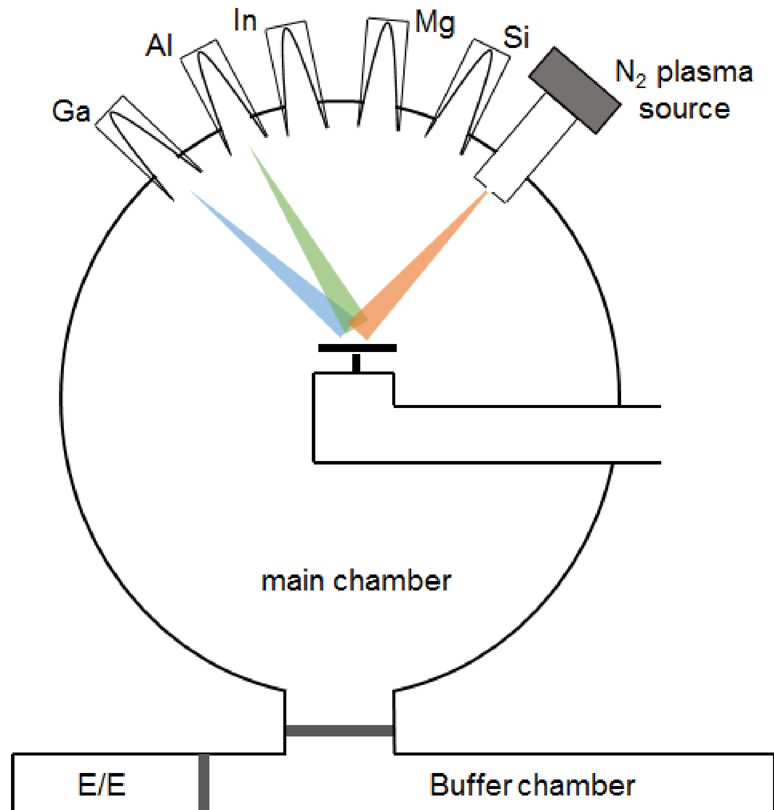

Figure 1.6: Schematic of a PAMBE machine, showing Knudsen effusion cells and rf plasma source for providing active N.

tion high-energy electron diffraction (RHEED) as an in-situ tool for monitoring the growth. The concentration of impurities such as H is much lower in layers grown by MBE. Si-doping with higher concentrations is achievable by this growth technique. Moreover, the fact that the growth temperature is considerably lower in MBE (700 °C) in comparison with MOCVD (1200 °C) makes it a suitable technique for doing regrowths on partially processed epi-structures.

The high vacuum environment in the MBE is maintained using combination of different pump mechanisms such as turbo, ion, and cryo pump. Moreover, the cryopanel around the chamber, chilled using liquid Nitrogen act as a sink for

impurities in the vacuum.

In MBE, metal constituents (Ga, In, Al, mg, Si) are heated in Knudsen effusion cells to sublime. The evaporated metal atoms travel and reach the substrate surface where they interact and form the crystal. Because of high vacuum, atoms have a large mean free path and do not get scattered by other atoms until they reach the substrate. There are two different methods for providing active N in MBE grwoth of III-N materials: radio frequency (RF) plasma, and ammonia. In the former method, active N is provided by N_2 molecules dissociation using RF plasma source, whereas in the latter one, active N is created via thermal decomposition of ammonia at the heated substrate. Fig. 1.6 illustrates a schematic of PAMBE, showing Knudsen effusion cells, RF plasma source and the substrate.

1.6 Synopsis of dissertation

The objective of this dissertation is to develop the growth procedure for In-contained III-N alloys using PAMBE, and utilize them for designing electronic devices. When this work began in 2011, it was believed that InAlN layer grown by PAMBE suffers from lateral variation in composition in "honeycomb" or "columnar" structures. In chapter 2, development of InAlN, lattice-matched to GaN, with uniform composition is explained. In addition, HEMT structures with InAlN backbarrier was designed and fabricated using the developed recipe for growth of InAlN on SiC substrates.

Direct growth of GaN on SiC by PAMBE results in relatively high threading dislocation densities ($\sim 3\times10^{10}$ cm^{-2}). Kaun *et al.* have shown previously that large

TDDs ($\sim 3\times10^{10}$ cm^{-2}) degrade the 2DEG mobility even in the case of high charge densities such as 1.4×10^{13} cm^{-2}. Free-standing GaN substrates are available with TDDs lower than 5×10^{7} cm^{-2}, however these kind of substrates are cost-prohibitive. Moreover, such low TDD is not essential for lateral devices. The other available option was GaN-on-sapphire templates grown by MOCVD on vicinal substrates. In chapter 3, growth of N-face HEMT structures with InAlN backbarrier on vicinal substrates is discussed. Chapter 4 is devoted to calculations of 2DEG mobility in N-face HEMT structures. The question that we tried to address in this chapter is how applying gate reverse bias or reducing channel thickness influence 2DEG charge density and mobility. In chapter 5, we developed a model to calculate the scattering rate from alloy fluctuations, and compared the limiting mobility for this kind of scattering mechanism for Ga-face AlGaN/GaN and InAlN/GaN heterostructures.

Chapter 6 is devoted to development of HET structures using PAMBE. The capability of growing pure AlN and high-In-content InGaN layers by PAMBE was the motivation for utilizing this growth technique for fabricating these structures. To understand the effect of Ga-rich growth condition in PAMBE growth technique on vertical devices, we studied the reverse leakage current of Schottky diodes grown in different conditions and compared the reverse leakage with those grown by ammonia MBE. The results of this study is discussed in chapter 7.

Chapter 2

N-Face HEMT Structures With InAlN as the Backbarrier

2.1 Introduction

GaN-based high-electron-mobility transistors (HEMTs) are particularly attractive for high-power and high-frequency applications due to GaN's large band gap (3.4 eV)[21, 22, 23, 24]. N-face GaN-based HEMTs have several advantages over Ga-face GaN-based HEMTs that make them promising for highly scaled devices. In N-face GaN-based HEMTs, the two-dimensional electron gas (2DEG) forms on top of the barrier, unlike in Ga-face HEMTs where the 2DEG is below the barrier. This is due to the lack of inversion symmetry in the wurtzite crystal structure which results in N-face and Ga-face GaN having opposite polarizations. Formation of the 2DEG above the barrier results in the formation of a natural backbarrier in N-face HEMTs with better confinement of the 2DEG. The enhanced confinement of the 2DEG improves the output resistance and pinch-off of the devices[25]. The charge

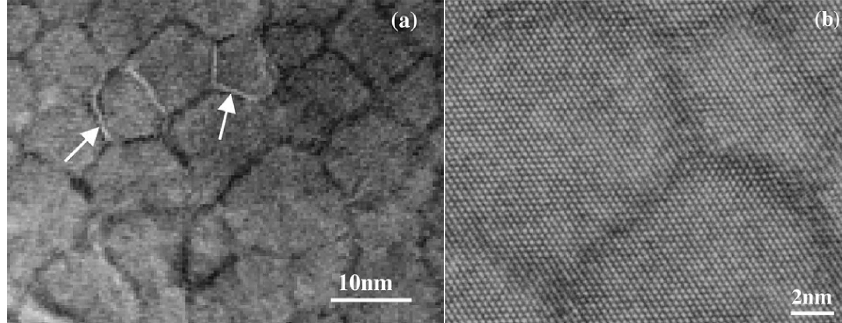

Figure 2.1: Plan-view electron micrographs of $In_{0.175}Al_{0.825}N$ showing lateral composition modulation in form of honeycomb microstructure with AlN-rich cores and InN-rich intercolumn boundaries[2].

centroid of the 2DEG is closer to the gate in N-face GaN-based HEMTs, allowing for better gate control, especially for scaled channels. In addition, as there is no large-bandgap barrier between the free surface and the 2DEG in N-face HEMTs, it is easier to achieve Ohmic contacts with very low resistance[24, 26].

Traditionally, AlGaN has been used as the barrier in both Ga-face and N-face GaN-based HEMTs[21, 27, 28, 29]. To achieve high charge density in AlGaN/GaN heterostructures, the AlN mole fraction or thickness of AlGaN needs to be increased. The thickness of the AlGaN barrier at which cracking occurs due to excess biaxial tensile stress is reduced with increasing AlN mole fraction. In addition, increasing the AlN mole fraction in the AlGaN/GaN heterostructure induces more strain, which may negatively impact device reliability[30]. InAlN is an alternative barrier material. In particular, $In_{0.18}Al_{0.72}N$ is attractive for HEMTs because it is lattice-matched to GaN. $In_{0.18}Al_{0.72}N$ also has a large bandgap of 4.2 eV[31] and high spontaneous polarization. This high spontaneous polarization results in a large polarization discontinuity at the $In_{0.18}Al_{0.72}N$/GaN heterointerface,

which is compensated by a high-density (>2 × 10^{13} cm^{-2}) 2DEG. In this context, excellent DC and RF performances have been demonstrated on both N-face and metal-face $In_{0.18}Al_{0.82}N$/GaN devices grown by metal-organic chemical vapor deposition (MOCVD)[32, 33, 34]. Also, Wong *et.al.*[35] obtained a good quality InAlN lattice matched to GaN with homogeneous composition using ammonia molecular beam epitaxy.

It has been shown[36] that inserting a thin layer of AlN between the alloy barrier and the channel improves the 2DEG mobility. However, the nominal AlN interlayer grown by MOCVD was shown to be an AlGaN layer with less than 50% AlN in practice[37]. It was believed that this can degrade the 2DEG mobility, especially in thin channels, because the 2DEG penetrates farther into the barrier as the channel is scaled down. With PAMBE, AlN interlayers are pure. Therefore, PAMBE is a promising method to obtain high 2DEG mobility in N-face HEMT structures with scaled channels.

However, in the case of InAlN growth by plasma-assisted molecular beam epitaxy (PAMBE), a strong non-uniformity in the in-plane In distribution was observed for both N-face and metal-face $In_{0.18}Al_{0.82}N$. Zhou *et al.*[2] reported for the first time lateral phase separation in InAlN layers grown by PAMBE in the shape of "honeycombs". As shown in Fig. 2.1, High-angle annular-dark-field (HAADF) image revealed that the contrast is contributed to severe modulation in InAlN composition. Such composition inhomogeneity manifested itself as a nanoscale columnar microstructure with AlN-rich cores and InN-rich intercolumn boundaries. This composition modulation in InAlN layers grown by PAMBE was later confirmed by Sahonata *et al.*[3] in 2009. They studied microscopic material quality of InAlN lay-

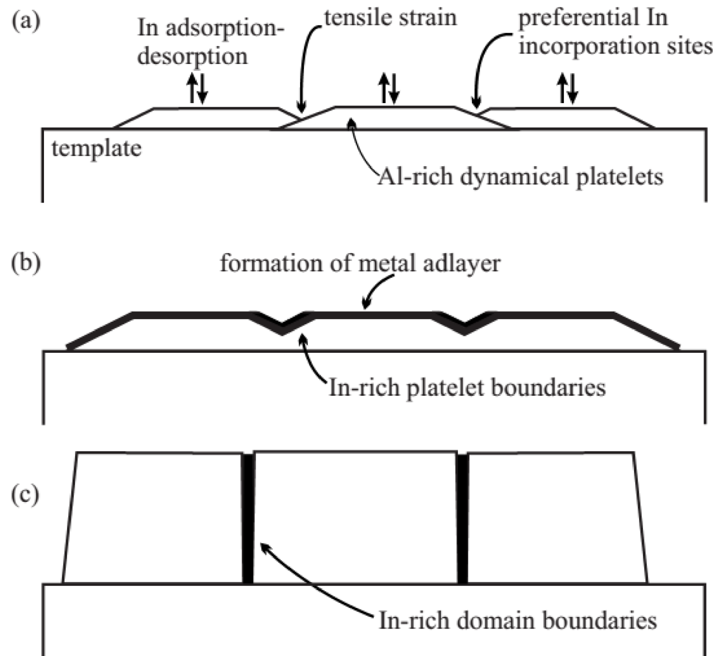

Figure 2.2: Schematic showing the growth dynamics resulting in composition modulation. (a) The growth starts with AlN rich platelets because of low mobility of Al adatoms on the surface, and high rate of In desorption from the surface. (b) In prefers to incorporate along the coalescence edges because of the tnsile stress. (c) columnar microstructures with AlN-rich cores and InN-rich intercolumn boundaries forms[3].

ers having three different compositions grown in metal-rich regime. Their HAADF images revealed a similar honeycomb microstructure. They proposed that the composition modulation is a result of formation of “Al-rich islands” in the beginning of the growth as shown in Fig. 2.2. They claimed that at the onset of islands coalescence, In adatoms prefer to incorporate along the islands coalescence edges because of tensile strain between these islands. In 2012 Choi *et al.*[4] Observed the same composition variation in InAlN layers grown in N-rich regime by PAMBE using different III/N ratios. Atom probe tomography (APT) (Fig. 2.3) analysis of these layers revealed that In mole fraction changes from 36% in the boundaries of columns to 7% in the center of columns. In addition, Dasgupta *et al.*[38] also observed these composition variations in InAlN layers grown in metal-rich regime on N-face.

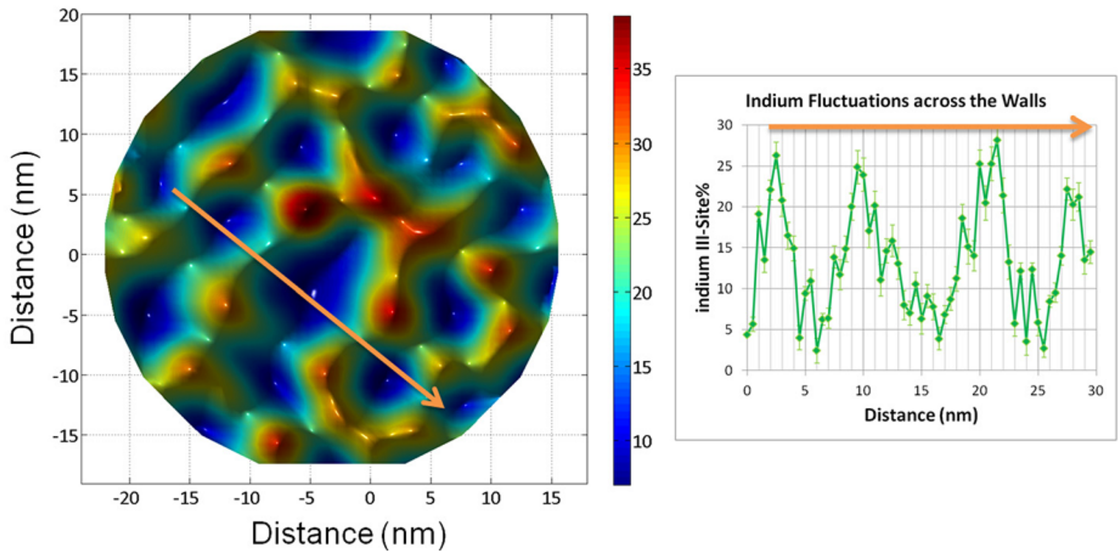

Figure 2.3: In III-site distribution taken using APT in a plane perpendicular to the growth direction. The InN mole fraction changes from 8% in the cores to 38% along the intercolumn boundaries[4].

Because of the large difference between InN and AlN bandgap and polarization, such non-uniformity in InAlN composition could be a source of scattering leading to degradation of the electron mobility in HEMT structures, and therefore, is not desirable.

In this chapter we discuss the growth of N-face lattice-matched InAlN by PAMBE in N-rich regime. By exploring different growth conditions, we were able to achieve InAlN layers with relatevly uniform composition. Thereafter, we grew N-face HEMT structures with lattice-matched InAlN as the back-barrier on SiC. The result of DC and RF characterizations of these HEMTs are shown and discussed in this chapter.

2.2 Growth of Homogeneous Lattice-matched InAlN on Free-standing GaN Substrates

Samples were grown in a Varian Gen-II MBE system, equipped with conventional thermal effusion cells for Al, Ga, and In sources and a Veeco Unibulb radio frequency (rf) plasma N source. The N source consisted of ultrahigh-purity (99.9995%) N_2 gas flowing at 0.3 SCCM through the rf-plasma source with 250 W rf power which corresponded to a growth rate of 250 nm/hr for metal-rich GaN layer. Samples used for structural studies were grown on commercial $(000\bar{1})$ N-face Free-Standing (FS) GaN substrates (Lumilog). All substrates were backside metallized with 500 nm of Ti for uniform thermal contact with the heater. Substrate temperatures were measured by an optical pyrometer calibrated to the melting point of Al.

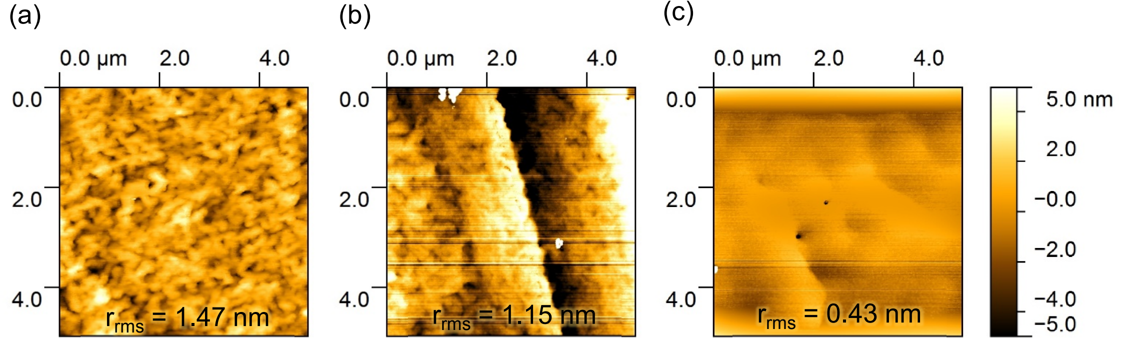

Figure 2.4: AFM images of InAlN layers grown at substrate temperature of (a) 480 °C (b) 500 °C (c) 520 °C.

In the first attempt, I grew a series of InAlN calibration samples, keeping In and Al beam equivalent pressures (BEP) at constant values of 2.4×10^{-8}, and 3.4×10^{-8}Torr, respectively. It was determined From previous calibrations, that the BEP of active N for the above-mentioned plasma conditions was 1.2×10^{-7} Torr. Therefore, the mentioned In and Al BEPs were low enough to assure N-rich growth environment. The substrate temperature was varied from 480 °C to 520 °C to study its effect on InAlN composition and the surface morphology. High resolution x-ray diffraction (HRXRD) symmetric $\omega - 2\theta$ scans were performed across on-axis (0002) reflections using the triple-axis detector to characterize the thickness and composition of the InAlN. According to Vegard's law, the InAlN peak lattice constant was assumed to change linearly with increasing InN mole fraction. The InN mole fraction was measured to be approximately 15% on all three samples. This confirms the fact that In desorption from surface is more or less constant in this substrate temperature range. Atomic force microscopy (AFM) images taken on these three samples showed a clear improvement of surface morphology at higher substrate temperatures (Fig. 2.4).

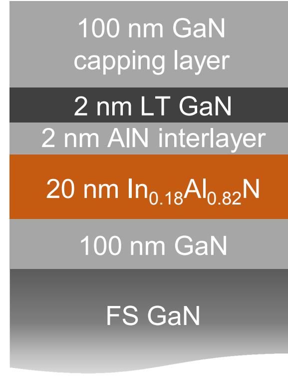

Figure 2.5: Schematic of InAlN/GaN/AlN/GaN heterostructures grown on N-face free-standing (FS) GaN for structural studies

The In and Al fluxes were optimized further at substrate temperature of 550 °C to obtain InAlN with 18% InN mole fraction. These BEPs were determined to be 2.9×10^{-8}, and 3.2×10^{-8} for In and Al, respectively. The coherency of InAlN layer to GaN was confirmed by recording in HRXRD reciprocal space maps (RSMs) around the asymmetric $(10\bar{1}5)$ reflection in co-planar geometry on a sample with 70 nm thick InAlN grown on FS GaN.

Afterwards, the structure shown in Fig. 2.5 was grown for APT and TEM studies. The structure grown for studying the material quality was designed to be similar to the the HEMT structure. The growth was initiated by growing a ~100 nm thick GaN buffer in Ga-rich conditions at a substrate temperature of 700 $^\circ$C to ensure a clean and smooth interface. The substrate temperature was then decreased to 550 $^\circ$C to grow the InAlN layer. The InAlN layer was grown under N-rich conditions using above-mentioned fluxes resulting in a III/V ratio $((f_{In}+f_{Al})/f_N)$ of ~0.4 and $f_{In}/(f_{Al}+f_{In})$ of ~0.2, where f_N is the flux of active

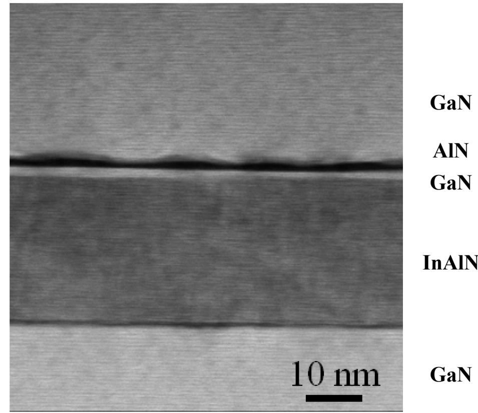

Figure 2.6: HAADF image of the InAlN showing a uniform contrast. TEM performed by Feng Wu.

nitrogen and f_{In} and f_{Al} are the In and Al fluxes, respectively. This was followed by growth of a thin (2 nm) GaN layer at low temperature to prevent the InAlN layer from decomposing during the increase of the substrate temperature for the subsequent growth of the AlN interlayer and the GaN channel (This is explained in more details in next section). The sample was capped with 100 nm GaN to be used as calibration for APT.

TEM samples were prepared by using FEI Helios 600 Dual Beam Focused Ion Beam instrument. Cross-sectional TEM was carried out with a FEI Tecnai G2 Sphera Microscope, operated at 200 kV. APT of the InAlN region was performed using a Cameca Local Electrode Atom Probe 3000X HR to investigate 3-D distribution of In. This technique combines time-of-flight measurement with point projection imaging. The region of interest is strategically positioned at the top of tapering tip approximately 50 nm in radius using a focused-ion-beam lift-out technique. The specimen was cooled to a base temperature of 30 K, and a high

voltage between 4 and 8 kV was applied. Simultaneous pulsing of Nd:YAG laser (532 nm second harmonic and 120 ps pulse width) at 200 kHz with a pulse energy of 0.02 nJ enabled controlled field evaporation of the atoms from the tip surface. The ions follow the electric field lines and reach a position sensitive detector (called the delay line detector) that records the x and y positions of the ions and their time-of-flight. Atoms were successively removed at a rate of 0.008 atoms/pulse, and the analysis was performed along the specimen axis. For the data reconstruction, the specimen was modeled as a hemisphere on a truncated cone. Suitably chosen reconstruction parameters de-magnify the detector coordinates of the ions to give their specimen coordinates. The ion time-of-flight estimates the mass-to-charge ratio. Details of the atom probe instrumentation and reconstruction algorithms are discussed elsewhere[39].

To investigate the structural properties of lattice matched InAlN with GaN, STEM studies were performed in cross-section orientation which is shown in Fig. 2.6. No composition modulation was observed in the InAlN layer as opposed to previous results on samples grown by PAMBE reported in the literature[4, 38, 3, 2]. The relatively rough surface of the AlN interlayer in this particular sample was a result of low temperature growth (700 °C). This issue was resolved later by keeping the Ga shutter open while growing this layer. Ga acts as a surfactant on the surface and reduces the energy barrier for Al atoms to diffuse on the surface[40].

Atom Probe analysis of this structure (Fig. 2.7) revealed that the In spatial distribution follows that depicted from a random alloy-binomial distribution. The

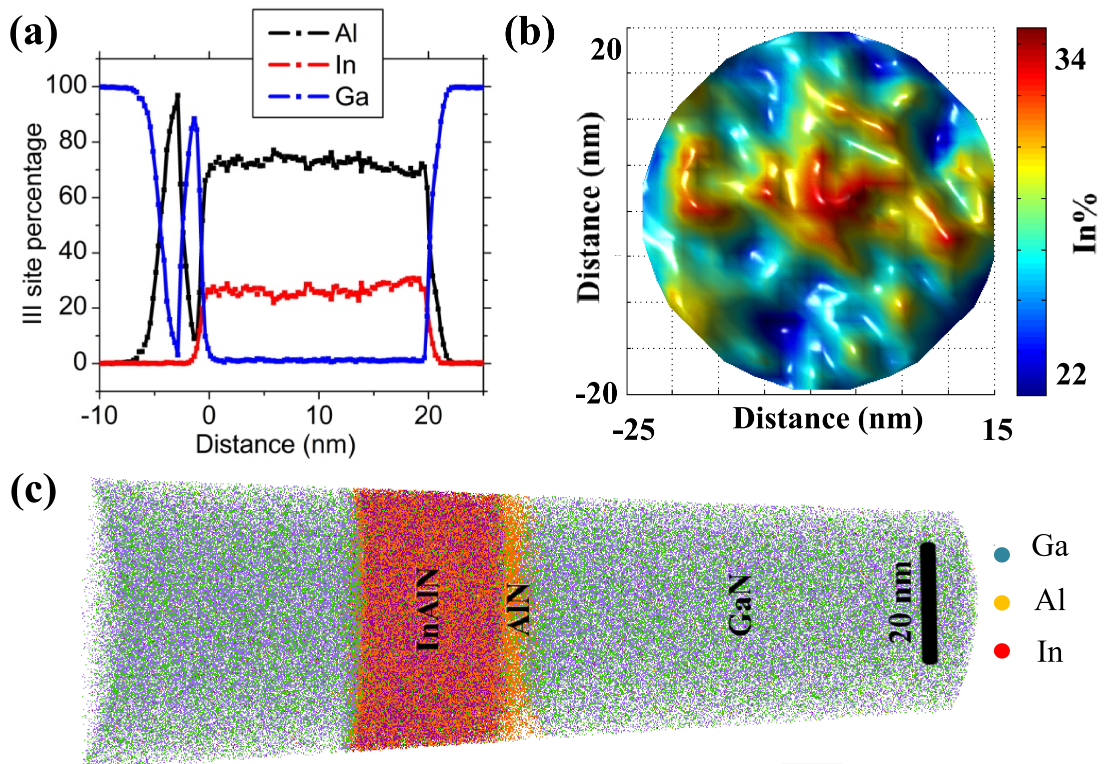

Figure 2.7: Proxigram map across the GaN/AlN/InAlN interfaces (b) 2D compositional map of In in plane perpendicular to growth direction (c) APT reconstruction of InAlN layer on N-face GaN by PAMBE. APT performed by Ravi Shivaraman.

average In composition in the InAlN layer was measured to be ~27% which was higher than the composition assumed by applying Vegard's law to the high resolution x-ray diffraction data ($\omega - 2\theta$ scans) – i.e., we believe that this discrepancy arises from the assumption that the lattice constants of InAlN is changing linearly with InN mole fraction which makes analysis of XRD data inaccurate. Very little In was found in the AlN layer, and a 1D-composition profile taken across the interface indicates an Al content nearing 98% III-site in the AlN layer (Fig. 2.7). Note that some of the elemental intermixing could be due to reconstruction artifacts arising from the large evaporation field differences between GaN and AlN which is most prominent at the center of the reconstruction. 1-D profiles from regions away from the center reveal nearly 100 % AlN.

2.3 Protective thin GaN cap on InAlN

It was explained in the previous section that in order to grow the AlN interlayer and GaN channel on top of InAlN in a HEMT structure, we need a thin GaN cap to protect InAlN from decomposition. We further used X-ray photoelectron spectroscopy (XPS) to study the necessity of GaN cap in protecting InAlN from decomposition.

XPS is considered a non-destructive technique used to study the surface chemistry. In this technique photons with specific energy (E_{photon}) are emitted toward the surface to excite the electronic states of the atom. The kinetic energy of electrons ($E_{kinetic}$) escaped from the surface is then measured by a detector. The binding energy of electron is given by Eq. 2.1.

	Sample A	Sample B	Sample C
Ga %	0	15.71	1.29
In %	6.66	1.89	3.87
Al %	24.66	13.47	29.12
In/(In+Al+Ga)	21%	6%	11%
In/(In+Al)	21%	12%	11%

Table 2.1: Ga, In, and Al surface concentrations measured by XPS on three InAlN samples. Sample A was cooled down right after growing InAlN layer. Sample B was protected with Ga wet layer while increasing substrate temperature to 700 °C for 10 minutes. Sample C had no protection while increasing substrate temperature to 700 °C for 10 minutes.

$$E_{binding} = E_{photon} - (E_{kinetic} + \Phi) \tag{2.1}$$

Where Φ is an adjustable instrument correction factor related to the work function dependent on both detector and the material. XPS can be used to measure the elemental composition of the material at the surface (depth less than 10 nm). Moreover, if combined with ion beam etching, it is possible to measure the composition as a function of depth.

To study the necessity of GaN cap in protecting InAlN from decomposition using XPS technique, three $In_{0.18}Al_{0.82}N$ samples were grown on N-face GaN-on-sapphire templates grown by MOCVD, as explained in the following.

Sample A: 10 nm of InAlN was grown at 550 °C. The growth was stopped right

after InAlN, and the substrate was cooled down.

Sample B: 10 nm of InAlN was grown at 550 °C. A Ga wet later was maintained on the surface during heating up substrate to 700 °C for 10 minutes. We made sure that the excess Ga is desorbed from the surface before cooling down the substrate.

Sample C: 10 nm of InAlN was grown at 550 °C. Then, the sample was heated up to 700 °C for 10 minutes without any protection, and then cooled down.

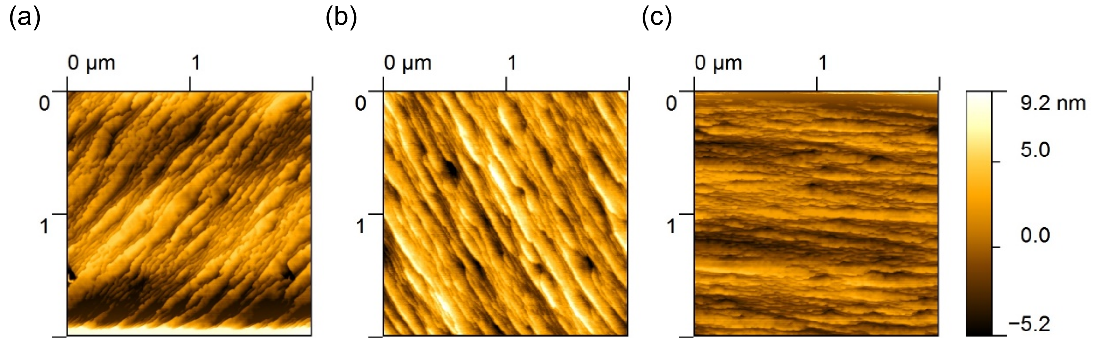

Figure 2.8: AFM image of samples grown to study the necessity of having a thin GaN on InAlN before heating up substrate to grow the other following layers in the structure. (a) Sample A: 10 nm of InAlN was grown at 550 °C. The growth was stopped right after InAlN, and the substrate was cooled down. (b) Sample B: 10 nm of InAlN was grown at 550 °C. A Ga wet later was maintained on the surface during heating up substrate to 700 °C for 10 minutes. We made sure that the excess Ga is desorbed from the surface before cooling down the substrate. (c) Sample C: 10 nm of InAlN was grown at 550 °C. Then, the sample was heated up to 700 °C for 10 minutes without any protection, and then cooled down.

The atomic percentage of Ga, In, and Al measured by XPS is shown in table2.1. Also, to compare the elemental composition of the layer, In to (In+Ga+Al) and In to (In+Al) ratios are shown in this table. On sample A, no Ga peak was detected,

and the InAlN composition was measured to be 21% InN mole fraction, which is close to what was measured from XRD. The small difference could be related to using Vegard's law for exporting the composition from XRD data which makes it inaccurate. On sample B, a large percentage of In atoms were replaced by Ga atoms resulting in a quaternary material InGaAlN. XPS on sample C revealed that heating substrate without any protection results in InAlN decomposition, and, consequently, a lower InN mole fraction in InAlN layer. Fig. 2.8 shows the AFM images on sample A, B, and C. It seems that Ga incorporation on sample B resulted in a smoother surface.

2.4 N-face HEMT structures with InAlN back-barrier on SiC

Using the same growth conditions for the InAlN layer, the HEMT structure shown in Fig. 2.9 was grown directly on C-face of on-axis 6H-SiC. The growth was initiated with an AlN layer grown with an Al/N flux ratio of 0.6 at 740 °C to reduce threading dislocation density and followed by growth of a 600 nm thick GaN buffer at 700 °C. The TDD, estimated from the rocking curve full widths at half maximum of HRXRD ω-scans (Δω) for the GaN ($20\bar{2}1$) reflection, was ~3×10^{10} cm^{-2}. Thereafter, a thin layer of Si doped GaN with a doping concentration of 1.5×10^{19} cm^{-3} was grown, followed by 10 minutes interruption to decrease the substrate temperature to 550 °C. After growth of 26 nm of $In_{0.18}Al_{0.82}N$, a thin GaN cap was grown at the same substrate temperature, followed by an interruption to increase the substrate temperature to 700 °C for the subsequent growth of AlN interlayer and the

Figure 2.9: Schematic of InAlN/GaN/AlN/GaN HEMT structure grown on C-face SiC for 2DEG mobility studies and HEMT fabrication. There is a Si delta-doped with 1.5×10^{19} cm^{-3} concentration at the back of barrier.

GaN channel. It has been shown before that 2 nm AlN between the alloy barrier and GaN channel is critical to achieve high 2DEG mobility[36]. A Ga-wet layer was maintained at the surface during increasing substrate temperature by opening and closing Ga shutter while monitoring the RHEED intensity. Keeping this Ga wet-layer is necessary to prevent incorporation of impurities at the interface.

In this series, the thickness of doping layer was varied, keeping everything else unaltered, to study the effect of 2DEG charge density on its mobility. A representative AFM image of one of these HEMT structures grown on SiC is shown in Fig. 2.10, The device wafer was diced into 7 mm ×7 mm square pieces for Hall measurement in Van der Pauw geometry. The 2DEG charge density, mobility and sheet resistance for three different doped layer thicknesses are reported in table2.2. 2DEG mobilities measured for the charge density of 2.4×10^{13} and 2.7×10^{13} were similar. Whereas, a significant mobility reduction was observed for a 2DEG charge density of 2.9×10^{13}.

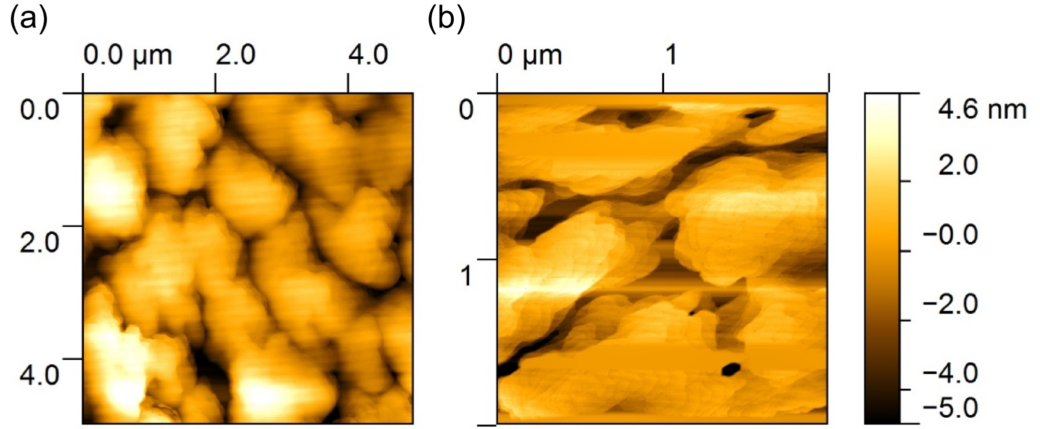

Figure 2.10: Representative (a)5×5 µm^2 and (b) 2×2 µm^2 AFM images of the HEMT structure grown on C-face SiC as shown in Fig.2.9. The surface has a flower-like morphology with an rms roughness of 0.9 nm in a 2×2 µm^2 area.

doping thickness	charge density (cm^{-2})	mobility (cm^2/Vs)	sheet resistance (Ω/□)
4 nm	2.4×10^{13}	786	332
6 nm	2.7×10^{13}	800	290
8 nm	2.9×10^{13}	635	339

Table 2.2: 2DEG Charge density, mobility, and sheet resistance in N-face HEMT structures with $In_{0.18}Al_{0.82}N$ as backbarrier grown on C-face SiC.

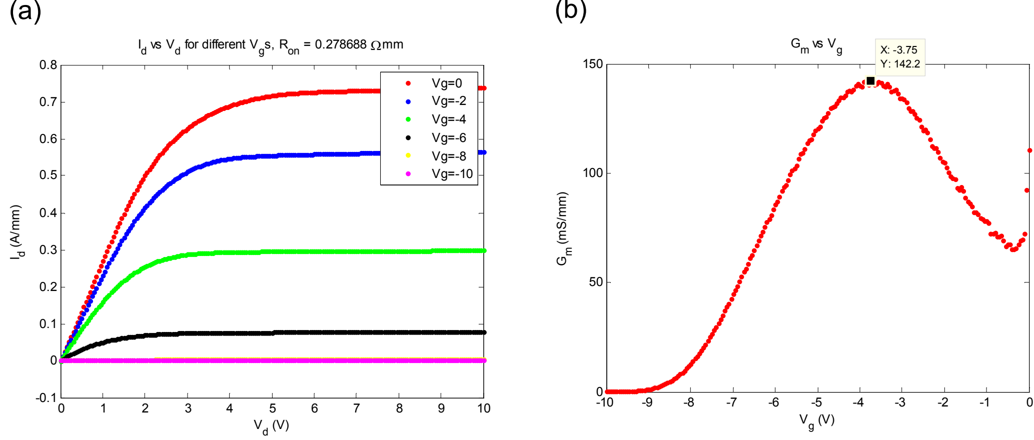

Figure 2.11: (a) DC current-voltage (IV) and (b) Extrinsic conductance as a function of gate voltage for different Drain voltages measured on of the HEMT structure shown in Fig. 2.9

A 5 nm-thick MOCVD SiN layer was deposited on the sample before fabricating HEMTs on it. The thin SiN layer protects the N-face surface from being etched in the developer, acts as the dielectric under the gate, and helps passivating the surface. The epilayer was then processed into HEMT structures. A Ti/Al/Ni/Au (20/120/30/50 nm) multilayer stack, annealed at 820 $^\circ$C for 30s in N_2, was used for the Ohmic source and drain contacts. Mesas were formed with BCl_3/Cl_2 reactive ion etching. Ni/Au/Ni (30/250/50 nm) was used as the gate metallization. The HEMTs were 2×75 µm wide with a nominal gate length of 0.7 µm, a gate-source spacing of 0.3 µm, and a gate-drain spacing of 0.9 µm. The HEMTs showed a DC drain current (I_D) of 0.7 A/mm with a soft pinch-off at VG= -9 V, and maximum G_m of 150 mS/mm (Fig. 2.11).

Pulsed IV measurements, with 80 ns, and 200 ns periods, were also performed on a HEMT with a nominal gate length of 0.7 µm, a gate-source spacing of 0.5 µm, and a gate-drain spacing of 2 µm. These measurements revealed higher pulsed

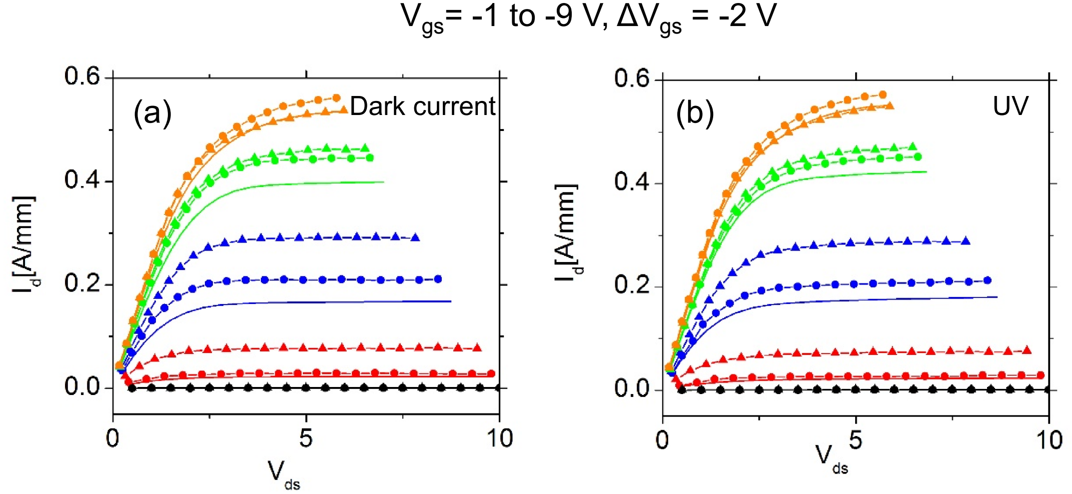

Figure 2.12: 200 ns (filled circles) and 80 ns (filled triangular) pulsed current and DC current (lines) for a HEMT with a nominal gate length of 0.7 µm, a gate-source spacing of 0.5 µm, and a gate-drain spacing of 2 µm, measured (a) in dark (b) under UV. Measurements performed by Matthew Guidry.

current than DC current (anti-dispersion), as illustrated in Fig. 2.12. 80 ns pulsed current is always larger than the DC current, whereas 200 ns pulsed current is larger than DC current for gate voltages (V_G) lower than -4V, and smaller than DC current for V_G higher than -4V. The IV curve measured under UV and dark conditions look almost identical.

2.5 Improvement of the quality of AlN layer using Ga as surfactant

As can be observed in Fig. 2.6, the AlN interlayer in the HEMT structure series with different doping was relatively rough. The reason is that Al adatoms have low mobility on the surface. Therefore, the substrate temperature needed to achieve

Figure 2.13: Schematic of InAlN/GaN/AlN/GaN HEMT structure grown on C-face SiC for 2DEG mobility studies and HEMT fabrication purpose. The buffer is C-doped to compensate the unintentionally incorporated donors (oxygen).

high quality AlN layer is higher (800 °C) than that needed for GaN (700 °C). However, growing AlN interlayer at 800 °C requires a growth interruption at AlN-GaN interface (right where the 2DEG forms) to reduce substrate temperature for growing the subsequent GaN channel. Growth interruption usually results in impurity incorporation, and is not desirable especially where the 2DEG forms. The other option is to grow AlN at the same temperature as GaN while keeping Ga on the surface as surfactant to improve Al adatoms mobility. Ga-N bond energy (2.28 eV) is lower than Al-N bond energy (2.92 eV), which makes it more preferential for N atoms to bond with Al adatoms. Therefore, if there are enough Al atoms to consume all the active N, Ga adatoms only remain on the surface and can be desorbed at the end of growth.

The structure shown in Fig. 2.13, was grown on C-face of SiC. The concentration of unintentionally incorporated oxygen in the GaN buffer layer is sensitive to the MBE chamber purity condition, and may be sometimes higher than expected

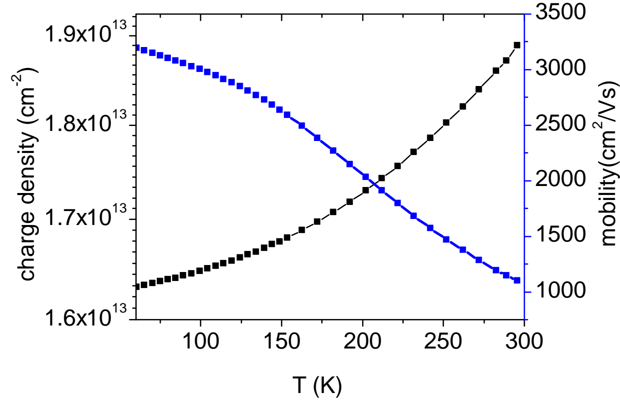

Figure 2.14: Temperature dependence of the 2DEG mobility and sheet charge density for GaN/AlN/GaN/InAlN HEMT structure grown on C-face of SiC.

when the chamber is contaminated. As oxygen is a shallow donor, high oxygen concentration in the buffer layer results in unexpected high charge density in the channel. To avoid this, we developed a C-doped buffer. In this design, there is a 600 nm-thick C-doped GaN layer with C concentration of 5×10^{18} cm^{-3}, followed by 200 nm UID GaN. The rest of the structure was grown as explained in the previous section. Note that there is no Si-doping at the backside of the barrier in this structure.

The device wafer was diced into 7 mm $\times$7 mm square pieces for Hall measurement in Van der Pauw geometry. Annealed In contacts were formed at the corners of the square pieces for Hall measurement. Fig. 2.14 shows the temperature dependence of the 2DEG mobility and sheet charge density. A 2DEG mobility and sheet charge density of 1100 cm^2/Vs and 1.9×10^{13} cm^{-2} were recorded at room temperature, respectively, which corresponds to a sheet resistance of 299 $\Omega/\Box$.

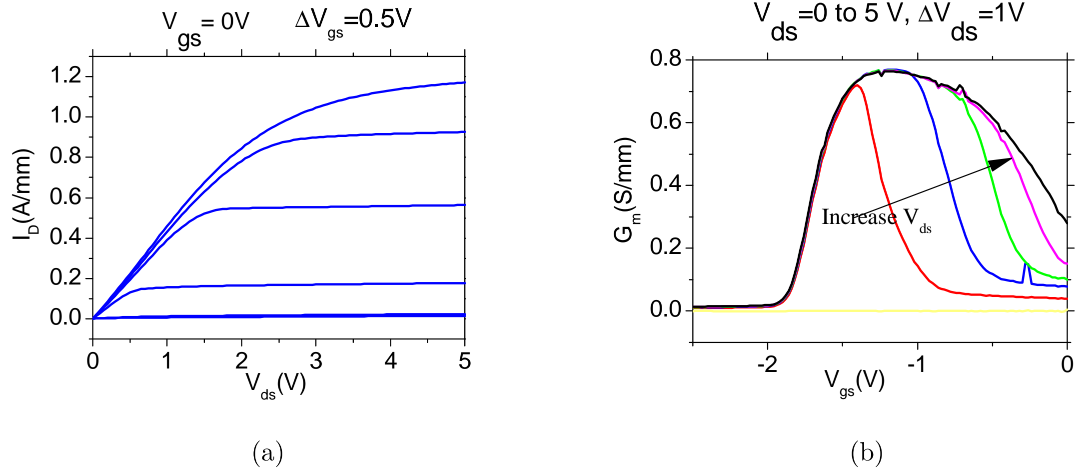

(a)

(b)

Figure 2.15: (a) DC current-voltage (IV) measurement of the GaN/InAlN/GaN/AlN/GaN HEMT grown on C-face SiC substrate. (b) Extrinsic conductance as a function of gate voltage for different Drain voltages measured on the GaN/InAlN/GaN/AlN/GaN HEMT grown on C-face SiC substrate.

The epilayer was then processed into HEMT structures using the same recipe explained in the previous section. The HEMTs were 2×75 μm wide with a nominal gate length of 0.7 μm, a gate-source spacing of 0.3 μm, and a gate-drain spacing of 0.9 μm. The HEMTs showed a DC drain current (I_D) of 1.19 A/mm with a soft pinch-off at VG= -2.5 V (Fig. 2.15a) and maximum G_m of 760 mS/mm (Fig. 2.15b).

Comparing this results with the one demonstrated in the previous section, These HEMTs have surprisingly large G_m, which is unexpected for the above-mentioned gate length, and channel thickness. The pinch off voltage is also unexpectedly small for such high charge density. S-parameter measurements were performed to extract the RF G_m. The results shown in Fig. 2.16 revealed that maximum RF

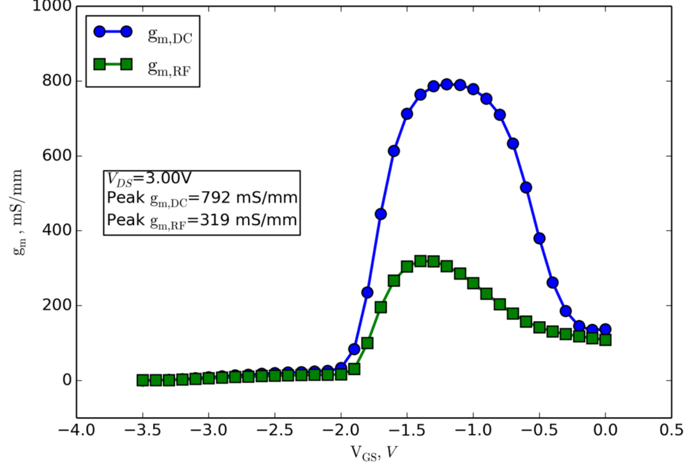

Figure 2.16: RF Gm and DC Gm measured for a HEMT with gate width and length of 100 µm and 0.7 µm, respectively, and L_{gs} and L_{gd} of 0.3 µm and 1 µm, respectively.

G_m is less than half of maximum DC G_m.

Comparing the DC characteristics along with the RF $G_m$on the HEMT with Si delta-doping, discussed in the previous section, with those without Si delta-doping, discussed in this section, we speculate that the unexpected high DC G_m on HEMT without Si-delta doping could be attributed to the hole traps at the backside of InAlN backbarrier. However, making a rigorous conclusion needs further studies.

2.6 Summary

In conclusion, N-face InAlN with homogeneous alloy composition was demonstrated using PAMBE in the N-rich regime. The elimination of the columnar microstructure previously observed in N-rich PAMBE-grown InAlN layers was achieved through increases in the growth temperature and $f_{In}/(f_{Al}+ f_{In})$. A RT 2DEG mobility of 1100 cm^2 /Vs and sheet charge density of 1.9×10^{13} cm^{-2} were

measured in an N-face GaN/AlN/GaN/InAlN heterostructure, and N-face HEMTs with lattice-matched InAlN back barriers were fabricated. These N-face HEMTs exhibited a maximum drain current of 1.19 A/mm and a high DC transconductance of 760 mS/mm.

Chapter 3

Growth of Lattice-matched InAlN on vicinal substrates

3.1 Introduction

In the previous chapter, we presented growth of N-face GaN/AlN/GaN/InAlN HEMT directly on on-axis SiC substrates by PAMBE. A 2DEG charge density of 1.9×10^{13} cm^{-2} and a reasonably high mobility of 1100 cm^2/Vs were demonstrated with these structures[41]. However, the threading dislocation density (TDD) of GaN grown directly on SiC by PAMBE is two orders of magnitude higher (~2×10^{10} cm^{-2}) than GaN grown by MOCVD on SiC or sapphire (~5×10^8 cm^{-2})[36]. This high TDD can severely degrade the 2DEG mobility, especially at lower 2DEG sheet densities[36]. In this work, we studied the growth of N-face GaN-based HEMT structures with InAlN backbarriers on MOCVD-grown GaN templates that had a TDD of ~5×10^8 cm^{-2}.

It has been shown that the growth of N-face GaN on on-axis substrates (both

homoepitaxially and heteroepitaxially) by MOCVD results in the formation of large hexagonal hillocks[5]. Hence, high-quality semi-insulating GaN buffers grown by MOCVD exist only on vicinal substrates[5]. Although a 2° miscut toward sapphire $< 11\bar{2}0 >$ was shown to be sufficient to eliminate hillocks, larger miscut angles (3° and 4°) were shown to be more reliable. The inclination to form higher multisteps increases with increasing miscut angle[42]. Therefore, there is a trade-off between eliminating hillocks and higher multisteps. For this reason, sapphire substrates with only 4° miscuts are usually used to grow N-face GaN-based structures by MOCVD. GaN grown on sapphire substrates with a 4° miscut towards sapphire $< 11\bar{2}0 >$ exhibits a-direction steps that are 4 monolayers in height[5, 43]. These vicinal MOCVD-grown GaN-on-sapphire substrates with 4° miscuts were used for the PAMBE growths presented in this study.

In the following sections, the growth and electrical characterization of GaN/ AlN/GaN/$In_{0.18}Al_{0.82}N$ structures on vicinal substrates are presented and discussed. Thereafter, we study the effects of growth conditions on the quality of the InAlN layers grown on vicinal GaN-on-sapphire substrates. Following that, we report on the electrical characterization of 2DEGs in HEMT structures with double backbarriers, including $In_{0.18}Al_{0.82}N$ and $Al_{0.57}Ga_{0.43}N$.

3.2 Growth and measurement instrumentation

All samples were grown in a Varian Gen-II MBE system, equipped with conventional thermal effusion cells for Al, Ga, and In sources and a Veeco Unibulb radio frequency (rf) plasma source. The N source consisted of ultrahigh-purity

(99.9995%) N_2 gas flowing at 0.7 SCCM through the rf-plasma source with 250 W rf power, which corresponded to a growth rate of 270 nm/hr for metal-rich GaN layers. All substrates were backside metallized with 500 nm of Ti for uniform thermal coupling with the heater. Substrate temperatures were measured by an optical pyrometer calibrated to the melting point of Al. All samples were grown on vicinal semi-insulating GaN templates with 4 $^\circ$ miscut along GaN $< 10\bar{1}0 >$. InAlN layers were characterized with high-resolution x-ray diffraction (HRXRD) using Cu Kα radiation in a PANalytical X'pert Pro MRD. X'pert Epitaxy software was then used to calculate the InN mole fraction of the layer by fitting $\omega - 2\theta$ scans of the GaN (0002) reflection. Atomic force microscopy (AFM) was used to characterize the surface morphology of the samples. STEM specimens were extracted using an FEI Helios 600 Dual Beam Focused Ion Beam instrument. Cross-sectional and plan-view STEM was carried out with an FEI Titan FEG Microscope, operated at 300 kV.

3.3 HEMT structures with InAlN as the back-barrier

HEMT structures (Fig. 6.2) with different InAlN thicknesses were grown. The InAlN layer in these structures was grown at 550 $^\circ$C, using In and Al beam equivalent pressures (BEPs) of 2.9 $\times$ 10^{-8} and 3.2 $\times$ 10^{-8} Torr, respectively. It was demonstrated in previous chapter that InAlN layers grown on on-axis (nominally singular surface) substrates, using the aforementioned growth conditions, have uniform composition[41]. The growth was initiated with a 400-nm-thick C-doped (~1

$\times$ 10^{18} cm^{-3}) GaN layer to compensate for residual Si at the regrowth interface. Because of Si accumulation on the surface of the GaN template, as a consequence of its exposure to the air, there is a high concentration of Si (~1 $\times$ 10^{19} cm^{-3}) incorporated at the regrowth interface. Si is a shallow donor in GaN. C is a deep-level trap[44] or compensating accepter[45] in GaN. Therefore, a thick layer of C-doped GaN is necessary to achieve a semi-insulating GaN buffer. This was followed by the growth of a 50-nm-thick unintentionally-doped (UID) GaN layer. Both C-doped and UID GaN layers were grown in the metal-rich regime at 700 $^\circ$C[6]. Thereafter, the growth was interrupted for 10 min to decrease the substrate temperature to 550 $^\circ$C to grow the $In_{0.18}Al_{0.82}N$ layer, which was followed immediately by 2 nm of GaN grown at the same temperature (LT GaN). This LT GaN interlayer is necessary to prevent decomposition of the InAlN layer while increasing the substrate temperature. The substrate temperature was then increased to 700 $^\circ$C during a second growth interruption. To suppress impurity accumulation on the growth surface, a layer of liquid Ga was maintained on the surface as the substrate temperature was increased[46]. A 2-nm-thick interlayer of pure AlN[37] and 20-nm-thick GaN channel were then grown subsequently at 700 $^\circ$C.

From secondary ion mass spectroscopy that was performed on our samples, the O concentrations in the N-face GaN and InAlN layers were 5×10^{16} cm^{-3} and 1×10^{18} cm^{-3}, respectively. The higher O concentration in the InAlN layer is likely related to the high AlN content. The O concentrations of these layers were similar to those that were measured in Ga-face GaN and InAlN grown by PAMBE.

Transmission line measurement (TLM) and van der Pauw patterns were fabricated using optical lithography. To provide Ohmic contacts, metal stacks of

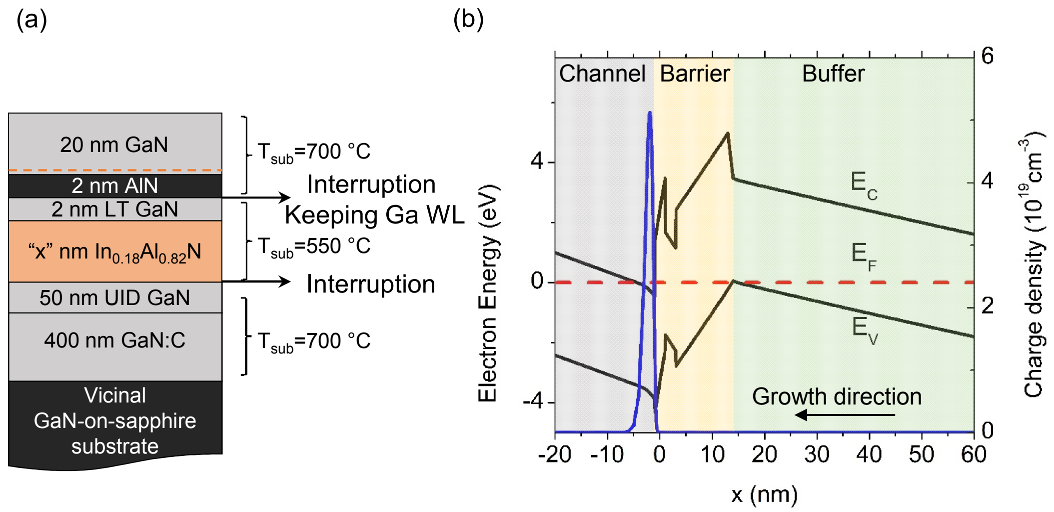

Figure 3.1: (a) Schematic of N-face GaN/AlN/GaN/InAlN/GaN HEMT structures grown on vicinal GaN-on-sapphire substrates with 4° miscuts along GaN$< 10\bar{1}0 >$, showing substrate temperatures (T_{sub}). The growth was interrupted twice. During the first interruption, the substrate temperature was decreased before growth of InAlN layer. During the second interruption, the substrate temperature was increased to grow the AlN interlayer and the GaN channel. (b) Band diagram of the structure shown in part (a) with a 10-nm-thick InAlN layer.

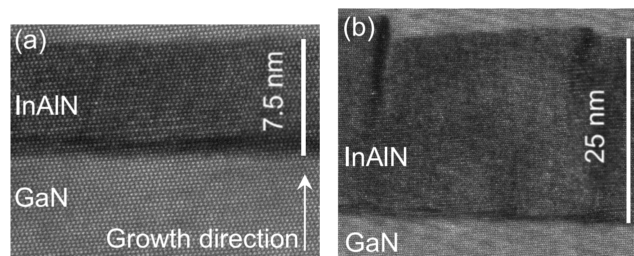

Figure 3.2: STEM images of (a) 7.5-nm-thick and (b) 25-nm-thick InAlN layers in N-face GaN/AlN/InAlN/GaN HEMT structures grown on vicinal GaN-on-sapphire substrates.

InAlN thickness	7.5 nm	16 nm	25 nm
n_s (cm^{-2})	$1.1{\times}10^{13}$	$1.1{\times}10^{13}$	$1.5{\times}10^{13}$
$\mu_{\|\|}$ (cm^2/Vs)	1850	1495	1490
$R_{\square,\|\|}$ ($\Omega/\square$)	307	380	445
$\mu_{\perp}$ (cm^2/Vs)	1721	1273	816
$R_{\square,\perp}$ ($\Omega/\square$)	330	446	510

Table 3.1: Charge density (n_s), mobility ($\mu_{||}$, $\mu_{\perp}$), and sheet resistance ($R_{\square,||}$, $R_{\square,\perp}$) in parallel and perpendicular directions to the steps in N-face GaN/AlN/GaN/InAlN/GaN HEMT structures with different InAlN layer thicknesses grown on vicinal GaN template.

Ti/Al/Ni/Au (200/1200/300/500 Å) were deposited by e-beam evaporation and then annealed at 820 $^\circ$C in an N_2 environment for 30 s. Mesa isolation was performed with a BCl_3/Cl_2 reactive ion etch.

The electrical measurements of HEMT structures grown on vicinal substrates by MOCVD have revealed different electron transport characteristics parallel and perpendicular to the steps[47]. The sheet resistances measured on TLM patterns fabricated perpendicular to the steps are higher than those measured on TLM patterns fabricated parallel to the steps. Hence, to measure the electron mobility parallel and perpendicular to the steps, TLM patterns were fabricated in both directions. TLMs were used to determine the 2DEG sheet resistance parallel and perpendicular to the steps, whereas Hall measurements on van der Pauw patterns provided the 2DEG sheet density. Using the values for 2DEG charge density (n_s)

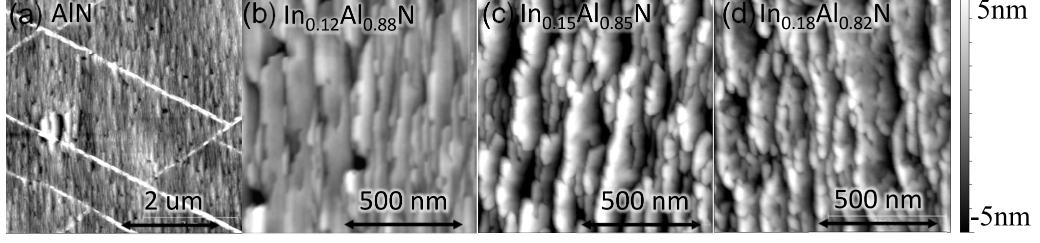

Figure 3.3: AFM images of InAlN layers grown at substrate temperatures of (a) 630 °C, (b) 600 °C, (c) 570 °C, and (d) 550 °C with fixed In and Al BEPs. The sample grown at 630 °C was cracked due to excess tensile stress in the AlN layer.

and parallel (perpendicular) sheet resistance (R_{sh}), the 2DEG mobility (μ) in the parallel (perpendicular) direction was obtained using Eq. 3.1.

$$\mu = 1/(en_sR_{sh}) \tag{3.1}$$

The charge density, mobility and the sheet resistance in both parallel and perpendicular directions on each structure are reported in table 3.1. By increasing the $In_{0.18}Al_{0.82}N$ thickness from 7.5 to 16 nm, the mobility dropped significantly, whereas the charge density remained the same. To understand the reason for decreased mobility with increased $In_{0.18}Al_{0.82}N$ thickness, cross-sectional STEM was performed on the samples with 7.5- and 25-nm-thick $In_{0.18}Al_{0.82}N$, as shown in Fig. 3.2. The surface of the 7.5-nm-thick $In_{0.18}Al_{0.82}N$ was smooth, and no lateral composition variation was observed. With the 25-nm-thick $In_{0.18}Al_{0.82}N$ layer, however, step bunching was evident, and there was lateral variation in the composition of the InAlN layer. This phenomenon has been previously reported in InGaAs layers grown on vicinal substrates[48, 49, 50]. Hiramoto *et al.*[50] attributed the step bunching and lateral composition variation to differences in the tendencies of

group-III adatoms to attach to kink or step sites and differences in their diffusion lengths.

3.4 Variation of InAlN growth conditions

We then explored the effects of substrate temperature on step bunching and lateral variation in the InAlN composition. The growth of samples used for structural studies was initiated with a 100-nm-thick UID GaN layer grown in Ga-rich regime at 700 ˚C. The substrate temperature was then decreased to grow the InAlN layer. In series A, In and Al BEPs of 2.9×10^{-8} and 3.2×10^{-8} Torr, respectively, were fixed, and the substrate temperature was varied from 550 ˚C to 630 ˚C. In, Al, and N shutters were kept open for 30 min on all samples to grow the InAlN layer. AFM images of these samples are shown in Fig. 3.3. A smoother surface was achieved by increasing the substrate temperature. The In incorporation, however, decreased at higher substrate temperatures and reached only 12% in the sample grown at 600 ˚C. In was not incorporated in the sample grown at 630˚C which resulted in cracking due to excess tensile stress in the AlN layer. Accordingly, the In BEP was optimized to achieve lattice-matched InAlN. For this purpose, multiple samples were grown with different In BEP, while the substrate temperature and the Al BEP were fixed at 600 ˚C and 3.2×10^{-8} Torr, respectively. An InAlN layer with an InN mole fraction of 0.18 was achieved at a substrate temperature of 600 ˚C with an In BEP of 4.5×10^{-8} Torr.

Cross-sectional STEM images were recorded near both the $\vec{a}$ (GaN $< 11\bar{2}0 >$) and the $\vec{m}$ (GaN$< 10\bar{1}0 >$) directions on this sample to inspect the uniformity and

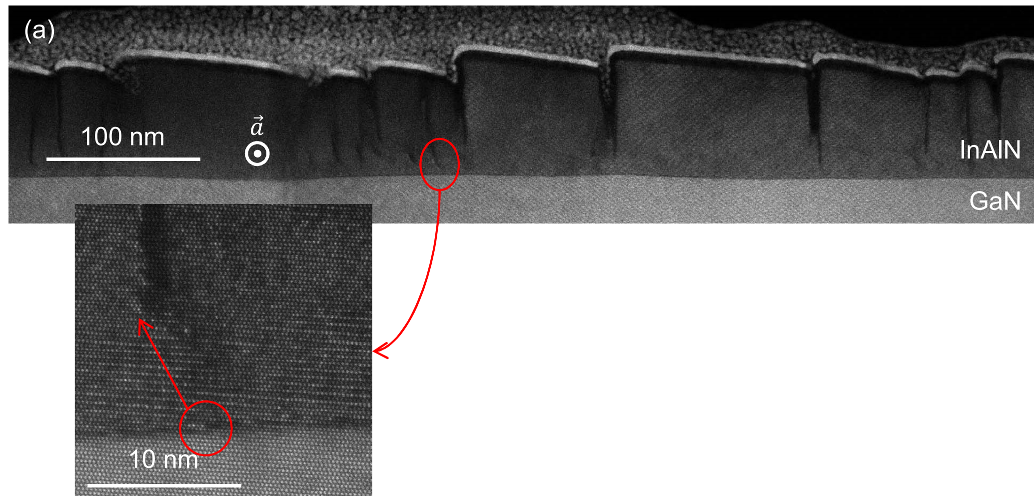

(a)

(b)

Figure 3.4: (a) cross-sectional STEM of the a-plane reveals InAlN composition variation in the lateral direction and step-bunching. As demonstrated in the inset, the fluctuations in the composition originate from the step edges and move toward the surface. (b) Cross-sectional STEM of the m-plane reveals uniform composition along m planes. TEM performed by Feng Wu.

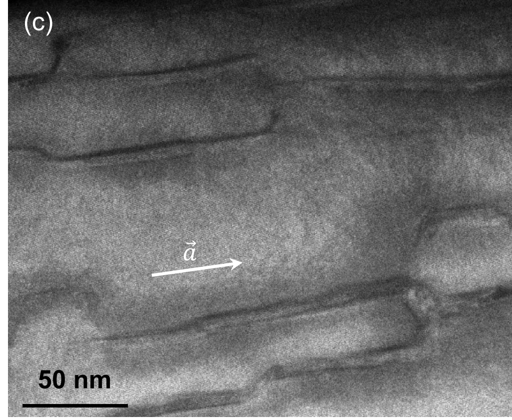

Figure 3.5: Plan-view STEM shows that the Al-rich regions form along GaN $< 11\bar{2}0 >$ in meandering lines. TEM performed by Feng Wu.

quality of InAlN layer (Fig. 3.4a and 3.4b). As illustrated in Fig. 3.4a, there is a lateral variation in InAlN composition along GaN$< 10\bar{1}0 >$ (perpendicular to the steps). Moreover, step bunches with step height as high as 6 nm were formed. On the contrary, the cross-sectional STEM image of the m-plane (parallel to the steps) revealed a smooth InAlN layer with relatively uniform composition. From the plan-view STEM, shown in Fig. 3.5, we can see that the AlN-rich regions in the InAlN layer form along GaN $< 11\bar{2}0 >$ in a meandering shape. Therefore, these composition variations affect the mobility not only in the direction perpendicular to the steps, but also parallel to them.

3.5 HEMT Structures with Double Backbarriers

InAlN grown on vicinal substrates was uniform and smooth for thicknesses lower than ~10 nm. In the next step, the InAlN thickness was limited to only 7.5 nm. However, charge density higher than $\sim 1 \times 10^{13}$ cm^{-2} is not achievable with only

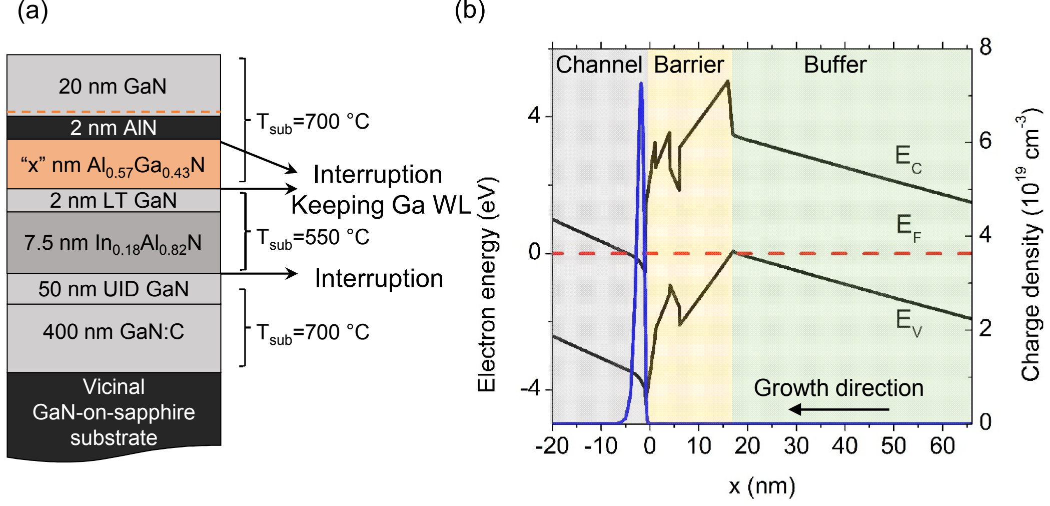

Figure 3.6: (a) Schematic of N-face GaN/AlN/AlGaN/GaN/InAlN/GaN HEMT structures grown on vicinal GaN-on-sapphire substrates with 4° miscuts along GaN $< 10\bar{1}0 >$, showing substrate temperatures (T_{sub}). The growth was interrupted three times. During the first interruption, the substrate temperature was decreased before growth of InAlN layer. During the second interruption, the substrate temperature was increased to grow the AlGaN barrier. During the third interruption, the Al cell temperature was increased to grow the following AlN interlayer. (b) Band diagram of the structure shown in part (a) with 3-nm-thick AlGaN layer.

7.5-nm-thick $In_{0.18}Al_{0.82}N$. Therefore, a double backbarrier, combining InAlN and AlGaN[51], was designed to achieve higher charge densities in the channel.

A series of HEMT structures (Fig. 3.6) with different $Al_{0.57}Ga_{0.43}N$ thicknesses were grown. TLM and van der paw Hall patterns were fabricated on the samples as described in the previous sections. The mobility and sheet resistance in the parallel and perpendicular directions and the charge density on each sample is reported in Table 3.2. The 2DEG charge density increased by increasing $Al_{0.57}Ga_{0.43}N$ thickness from 0 to 5 nm, as expected from the simulations per-

AlGaN thickness	0 nm	3 nm	5 nm	7 nm
n_s (cm^{-2})	1.1×10^{13}	1.3×10^{13}	2.0×10^{13}	2.0×10^{13}
$\mu_{\|\|}$ (cm^2/Vs)	1850	1830	1220	1360
$R_{\square,\|\|}$ ($\Omega/\square$)	307	262	256	230
$\mu_{\perp}$ (cm^2/Vs)	1721	1268	900	1034
$R_{\square,\perp}$ ($\Omega/\square$)	330	379	347	302

Table 3.2: Charge density (n_s), mobility ($\mu_{||}$, $\mu_{\perp}$), and sheet resistance ($R_{\square,||}$, $R_{\square,\perp}$) in parallel and perpendicular directions to the steps in N-face GaN/AlN/AlGaN/GaN/InAlN/GaN HEMT structures with different AlGaN layer thicknesses grown on vicinal GaN template.

formed using BandEng[52]. Although the 2DEG charge density remained constant on samples with 5- and 7-nm-thick $Al_{0.57}Ga_{0.43}N$ layers, the 2DEG mobility slightly improved on the latter one. The reason for this improvement is not well understood, and may just be a result of unintentional variations from sample to sample. Therefore, Using 7-nm-thick AlGaN layer, we were able to attain a sheet resistance of 230 $\Omega/\square$ which is lower than the values previously reported on N-face GaN-based HEMTs grown by MBE[**?**].

3.6 Summary

In summary, we showed that N-face InAlN layers grown by PAMBE on vicinal substrates remain smooth and have uniform composition up to a critical thickness (~10 nm). After reaching this critical thickness, step bunching was evident and

lateral InAlN composition variations arose along the direction perpendicular to the steps. These lateral composition variations degrade the mobility of 2DEG in HEMT structures with thick InAlN backbarriers. After designing a double backbarrier ($In_{0.18}Al_{0.82}N$ (7.5 nm)/ $Al_{0.57}Ga_{0.43}N$ (7 nm)), we were able to achieve a high 2DEG charge density of 2.0×10^{13} cm^{-2} with a mobility of 1360 cm^2/Vs.

Chapter 4

Modeling of 2DEG mobility in HEMT structures

4.1 Introduction

In recent years, GaN-based high-frequency HEMT structures have attracted much attention due to their high frequency and high power handling capabilities[24, 21]. As discussed in previous chapters, N-Face HEMTs structures have several advantages over the traditional Ga-Face devices. The inverted polarity of N-face means that the 2DEG is induced by the back-barrier, rather than the top barrier like in Ga-Face. To maintain a sufficient 2DEG density in either orientation, either a relatively thick Al(In)GaN or a very high Al composition Al(In)GaN charge inducing barrier layer is required. Because this barrier layer is located above the 2DEG (towards the surface) in Ga-Face HEMTs, a trade-off exists between the charge density and the degree to which the barrier layer can be scaled [53]. This trade-off is absent in N-Face devices, allowing aggressive scaling of the transistor

dimensions while maintaining a sufficiently high 2DEG density [33, 51]. The natural back-barrier in N-Face HEMTs improves the 2DEG confinement and leads to both lower output conductance and better pinch-off as well.

Two good measures of the device quality concerning the power loss in power switch and high frequency switch applications are Huang material figure of merit (HMFOM = $E_c\sqrt{\mu}$), and Baliga high-frequency figure of merit (BHFFOM = $\mu.E_c^2.V_G^{1/2}/2V_B^{1/5}$), respectively, which shows that for any fixed material system, power loss reduces by increasing the mobility (μ) of the 2DEG.[54] Therefore, it is very important to understand the source of scattering mechanisms which affect the 2DEG mobility. Although, the 2DEG mobility in Ga-face HEMT structures has been studied extensively[55, 56, 57, 58], few works has been published on calculations of 2DEG mobility in N-face HEMT structure[59, 60].

It has been observed previously that decreasing channel thickness[33, 59] or applying reverse bias[60] to the gate results in a reduction of the 2DEG density in addition to lowering 2DEG mobility, which combine to give significantly higher sheet resistance. Brown *et al.*[60] attributed the reduction in mobility with increasing reverse gate bias in N-Face HEMT structures to alloy scattering. Their calculations revealed that by applying higher gate reverse bias, the electric field in the channel increases significantly, which leads to further penetration of 2DEG wavefunction into the alloy backbarrier, and larger alloy scattering rate. In a separate work Singessiti *et al.*[59] attributed the 2DEG mobility reduction in N-face HEMT structure caused by decreasing the channel thickness to larger interface roughness scattering. Our calculations, discussed in this chapter, show that decreasing the channel thickness or increasing the gate reverse bias in N-face HEMTs

increases interface roughness and alloy scattering rates, however this increase is not significant enough to explain the severe reduction in 2DEG mobility seen at room temperature. We propose charged trap states at the GaN-AlGaN interface [61, 62] as the scattering mechanism responsible for the large reduction in mobility seen with decreasing channel thickness and/or increasing reverse gate bias.

In this chapter, we first discuss the procedure we used to calculate the 2DEG wavefunction needed for scattering rate calculations. Thereafter, we discuss mobility limit associated with each of the conventional scattering mechanisms for N-face HEMT structures at room temperature. The 2DEG mobility, considering the conventional scattering mechanisms, is then calculated as a function of gate reverse bias and channel thickness in N-face HEMTs. Two new scattering mechanisms (surface state dipoles and charged interface state) are then discussed. Thereafter, the 2DEG mobility at room temperature, considering all scattering mechanisms, is calculated as a function of channel thickness and the gate reverse bias.

4.2 Procedure

We used the Born approximation to calculate the matrix elements of each perturbing potential[63, 59]. For an accurate evaluation of the scattering rates, the finite extent of the 2DEG perpendicular to its plane must be accounted for. The Fang-Howard variational wavefunction has been used for this purpose in the past[60]. However, this method does not consider the wavefunction penetration into the barrier. Thus, it is not a suitable approximation for the calculation of interface roughness or alloy disorder scattering. For this reason, a modified version of the

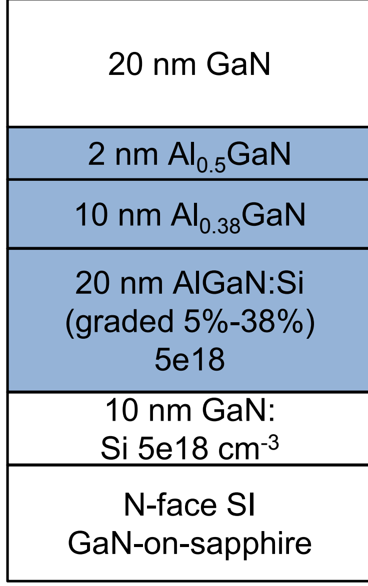

(a)

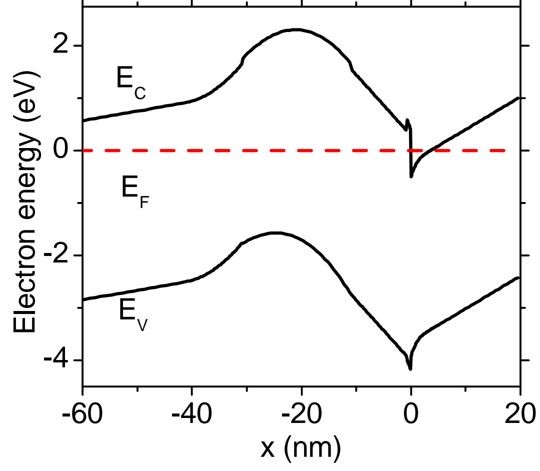

(b)

Figure 4.1: (a) Schematic and (b) band diagram of a typical N-face HEMT structure with AlGaN as the backbarrier. All the 2DEG mobility calculations shown in this chapter were performed for this structure.

Fang-Howard variational wavefunction has been developed, which is given in Eq. 4.1.

$$\begin{aligned} \Psi(z) &= M \exp\left(\frac{\kappa_b z}{2}\right) & z < 0 \\ \Psi(z) &= NC\,(z+z_0)^a \exp\left(-\frac{bz}{2}\right) & z > 0 \end{aligned} \tag{4.1}$$

Here, parameters b, κ_b, z_0, M, and a are commonly derived analytically using variational approximation of ground state and considering the normalization condition and continuity of wavefunction and its derivative at the interface between GaN channel and AlGaN barrier, and are given by the following relations

$$\begin{aligned} \kappa_b &= \tfrac{2\sqrt{2m^*(\Delta E_C - E_0)}}{\hbar} \\ z_0 &= \tfrac{2a}{\kappa_b + b} \\ N &= \sqrt{\tfrac{\kappa_b}{\kappa_b e^{bz_0} + C^2 z_0^{2a}}} \\ M &= NZz_0^a \\ b &= \left(\tfrac{4em^* F(V_G)(2a+1)(2a-1)}{\hbar^2}\right)^{1/3} \end{aligned} \tag{4.2}$$

where m^*, e, and $F(V_G)$ are electron effective mass, electron charge, and electric field in the channel. $C = \sqrt{\frac{b^{2a+1}}{\Gamma(2a+1)}}$ is a normalization constant. This approximation is not always accurate either. For example, in AlGaN/GaN heterostructures with Al content as high as 6% , the ground state energy level calculated from this method is above the barrier, which results in an imaginary value for κ_b. An imaginary value for κ_b, intuitively means that 2DEG is not confined in the channel which is not consistent with the result obtained from BandEng[52](a self-consistent Schrödinger-Poisson solver).

Brown *et al.* used Eq.4.1 to calculate the 2DEG wavefunction formed in N-face HEMT structures under various gate reverse biases. They estimated $F(V_G)$ using Poisson equation, while assuming that it is safe to ignore Schrodinger correction. This resulted in an exaggeration of the effect of reverse bias on the electric field variation in the channel. Particularly, their approach overestimated the penetration of 2DEG into the barrier, and consequently, the effect of alloy scattering on the 2DEG mobility. Therefore, they attributed the 2DEG mobility reduction caused by applying negative gate voltage to larger alloy scattering rate.

In this work, instead of using the above-mentioned approximation, we employed BandEng to obtain the exact wavefunction. The HEMT structure that the 2DEG

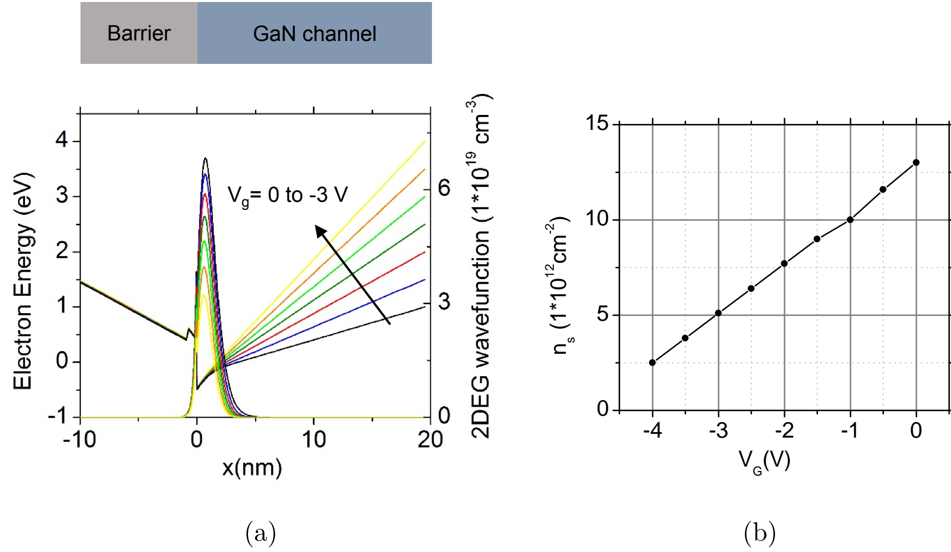

(a)

(b)

Figure 4.2: (a) 2DEG wavefunction along with the band diagram near the channel, and (b) charge density for the HEMT structure shown in Fig. 4.1a for different reverse biases applied to the gate.

mobility calculations were performed for, along with its band diagram are demonstrated in Figs. 4.1a and 4.1b. Fig.4.2a and Fig.4.3a show the 2DEG wave-function, extracted from BandEng, near the channel in the N-face HEMT structure shown in Fig.4.1a for different gate voltages and different channel thicknesses, respectively. As illustrated in these figures, the wavefunction penetration into the barrier does not change significantly with increasing reverse bias (for a channel thickness of 20 nm) or reducing channel thickness (for gate bias of 0 V). Moreover, the electric field in the region where 2DEG forms remains more or less unchanged in both cases. The 2DEG charge density (n_s), however, reduces by increasing the gate reverse bias, or decreasing channel thickness (figures 4.2b and 4.3b).

Using the wavefunction exported from BandEng, the 2DEG mobility was calculated through the Boltzmann transport equation in the relaxation time approx-

imation. We included different scattering mechanisms, namely the scattering from interface roughness, ionized background impurities, acoustic deformations, optical phonons, charged dislocations, alloy disorder, surface state dipole, and interface states. After calculating the limiting mobility for each scattering mechanism, Matthies-sen rule was then applied to combine their influences and calculate the total 2DEG mobility.

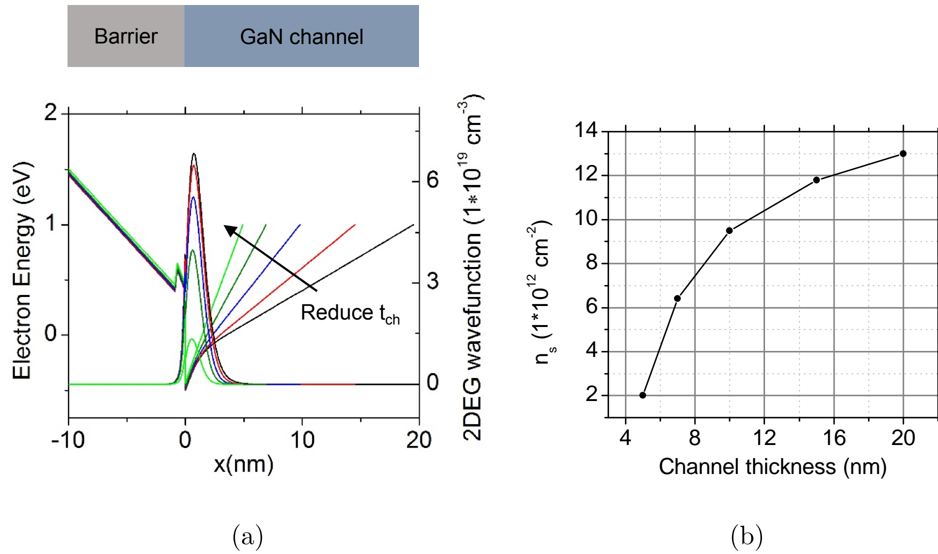

(a) (b)

Figure 4.3: (a) 2DEG wavefunction along with the band diagram near the channel, and (b) charge density for the HEMT structure shown in Fig. 4.1a for different channel thicknesses.

4.3 Conventional Scattering mechanisms

4.3.1 Phonon scattering

Phonons scatter electrons through coupling to both deformation as well as piezoelectric potentials in polar materials. In GaN HEMTs polar optical phonon scattering is typically the dominant scattering mechanism at room temperature. However,

polar acoustic phonon (known as piezoelectric scattering) is negligible in comparison to the acoustic deformation potential scattering. Further, although acoustic phonons have both longitudinal and transverse components, the transverse mode can be ignored safely as it is much weaker than the longitudinal mode. Therefore, we only include polar optical phonon and acoustic deformation potential in our calculations.

The relaxation time approximation is only applicable to describe elastic scattering events, whereas phonon scattering is an inelastic mechanism. Regardless, since the acoustic phonon energy is very low, it can still be assumed as a source of elastic scattering, and the scattering rate can be defined as the following

$$\frac{1}{\tau_{AC}} = \frac{3m^* b a_c^2 k_B T}{16 \rho v_s^2 \hbar^3} \tag{4.3}$$

where ρ, v_s, and a_c are mass density, sound velocity, and the deformation potential of GaN. k_B is the Boltzman constant. The electron mobility at room temperature limited only by acoustic deformation potential scattering was calculated for various gate reverse biases, and channel thicknesses in Figs. 4.4a and 4.4b, respectively. The acoustic phonon scattering rate increases by decreasing charge density. This dependence manifests itself through parameter b in Eq. 4.3.

On the contrary, optical phonons in GaN have high energy (90 meV). In 1993, Gelmont *et al.*[64] introduced an analytical approach to calculate optical phonon momentum relaxation time in the case of wide bandgap semiconductors, such as GaN, for which optical phonon energy is much larger than $k_B T$. In these kinds of semiconductors, because the optical phonon energy is much larger than the

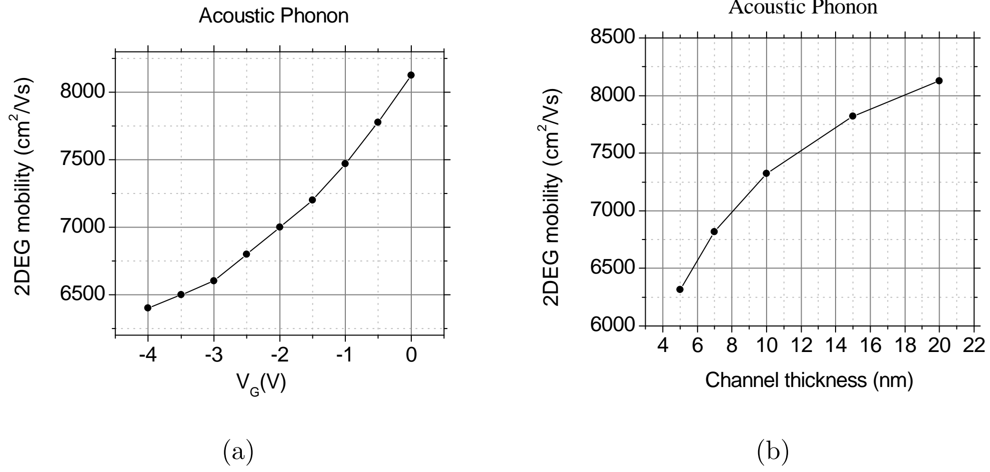

(a) (b)

Figure 4.4: 2DEG mobility limited only by acoustic deformation potential scattering at room temperature in N-face HEMT structure shown in Fig. 4.1a for (a) different gate voltages, and (b) channel thicknesses

electron's thermal energy (even at room temperature), the probability for phonon absorption is much higher than phonon emission. Therefore, the momentum relaxation time can be calculated considering only phonon absorption. Moreover, in 1994[65], it was shown by the same authors that when sub-band levels are close to each other (the difference is smaller than optical phonon energy), the scattering rate of optical phonon in 2DEG can be estimated using the scattering rate of optical phonon in the bulk as shown in Eq.4.4. This is specifically true for GaN since optical phonons have relatively large energy in this material system.

$$\mu_{OP} = \frac{4\pi\kappa^*\varepsilon_0\hbar}{3eNm^*}\left(\frac{2\hbar}{m^*\omega_0\left(1+\hbar\omega_0/E_g\right)}\right)^{1/2}\frac{I_2(\frac{k_BT}{E_g})}{I_1(\frac{k_BT}{E_g})} \tag{4.4}$$

Where e and m^* are the electron charge, and effective mass, respectively. N is the phonon Plank function. $\hbar\omega_0$ is the optical phonon energy. κ^* is the dielectric constant given by $1/\kappa^* = 1/\kappa_\infty - 1/\kappa_0$. $I_1(\gamma)$ and $I_2(\gamma)$ are related to

nonparabolicity and are given by the following relations

$$
\begin{aligned}
I_1(\gamma) &= \int (1+2\gamma x)\sqrt{x(1+\gamma x)}\exp(-x)\,dx \\
I_2(\gamma) &= \int [x(1+\gamma x)]^{3/2}(1+2\gamma x)^{-1}\exp(-x)\,dx.
\end{aligned}
\tag{4.5}
$$

Using the above relations, the electron mobility limited by optical phonon was calculated to be 2400 cm^2/Vs for bulk GaN, which was also used for 2DEG mobility calculation done in this work. This means that optical phonon scattering in GaN-based HEMT structures does not depend on channel thickness or reverse gate bias, and, therefore, charge density (in the range between 2×10^{12}cm^{-2} and 2×10^{13}cm^{-2}, that we are interested in).

Before proceeding with other scattering mechanisms, it is worth noting at the room temperature electron mobility in an ideal GaN-based HEMT structure where all the scattering mechanism are absent, and the 2DEG mobility is limited only by the crystal vibrations (acoustic and optical phonons). In that case, the 2DEG mobility at room temperature is 1745 cm^2/Vs, given by $1/\mu(300K) = 1/\mu_{OP}(300K) + 1/\mu_{AC}(300K)$.

4.3.2 Ionized background impurity

The concentration of unintentional donors (oxygen) in state of the art GaN epitaxy is on the order of 10^{16} cm^{-3}. The scattering rate of ionized background impurities can be calculated as the following[66]

$$
\frac{1}{\tau_{BGI}} = N_{imp}\frac{m^*}{2\pi\hbar^3 k_F^3}\left(\frac{e^2}{2\epsilon_0\epsilon_s}\right)^2 \int_0^{2k_F} dq \frac{F(q)}{(q+q_{TF}G(q))^2}\frac{q}{\sqrt{1-\left(\frac{q}{2k_F}\right)^2}}
\tag{4.6}
$$

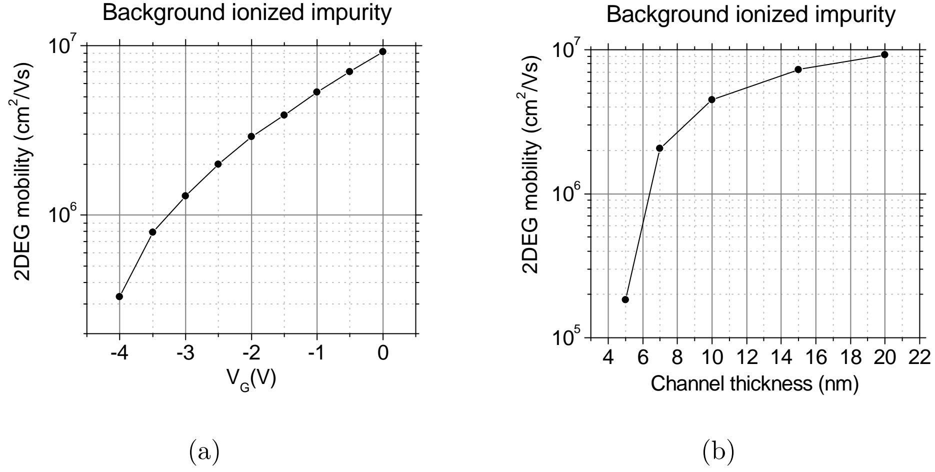

(a) (b)

Figure 4.5: 2DEG mobility limited only by background ionized impurity scattering at room temperature for a background impurity concentration of 3×10^{16} cm^{-3} in N-face HEMT structure shown in Fig. 4.1a for (a) different gate voltages, and (b) channel thicknesses

Where N_{imp} is the concentration of unintentional impurities. $q_{TF} = 2/a_B$, a_B being effective Bohr radius, is the Tomas-Fermi screening wavevector, and takes into account the screening of the scattering potential by the 2DEG. $F(q)$, and $G(q)$ are factors that count for the fact that it is not a delta function and has a finite extent in the z direction, and are given by the following equations.

$$\begin{aligned} F(q) &= \int |\Psi(z)|^2 \exp(-qz)\ dz \\ G(q) &= \int |\Psi(z_1)|^2 |\Psi(z_2)|^2 \exp(-q(z_1 - z_2))\ dz_1 dz_2 \end{aligned} \tag{4.7}$$

Figs.4.5a and 4.5b show the calculated 2DEG mobility limited by background ionized impurity scattering for the HEMT structure shown in Fig.4.1a for different gate biases and channel thicknesses, respectively. The scattering rate by background ionized impurity is higher for lower charge densities, because of less

screening of the scattering potential by electrons. Nonetheless, the scattering rate from background ionized impurity with a concentration of 3×10^{16} cm^{-3} is not high enough to limit the 2DEG mobility at room temperature.

4.3.3 Interface roughness

The GaN channel thickness is not atomically constant along the channel due to thickness fluctuations during epitaxial growth. These fluctuations are random and their statistical properties can be described by the co-variance function defined as $C(\overrightarrow{r}) = \int \Delta(\overrightarrow{r}')\Delta(\overrightarrow{r} - \overrightarrow{r}')d\overrightarrow{r}'$, where $\Delta(\overrightarrow{r}')$ is the thickness fluctuation at point $\overrightarrow{r}'$ in the channel. This co-variance function is commonly assumed as a Gaussian function given by $\Delta^2 \exp(-r^2/L^2)$, where Δ is the root mean square (rms) roughness, and L is the correlation length. Applying the Gaussian function, the scattering potential formed by interface roughness can be derived. This is explained in detail in references[67, 63, 59]. Finally, the scattering rate from interface roughness is given by Eq.4.8.

$$\frac{1}{\tau_{IR}} = \frac{m^* e^4 \Delta^2 L^2}{2\hbar^3 (\epsilon_0 \epsilon_s)^2} (\frac{n_s}{2})^2 \int_0^{2k_F} du \frac{q^4 \exp(-L^2 q^2)}{(q + G(q) q_{TF})^2 \sqrt{4k_F^2 - q^2}} \tag{4.8}$$

The rms surface roughness on N-face HEMT structures grown by MOCVD on vicinal substrates has been reported to be approximately 0.5 nm in a 2×2 µm^2 area[68]. The 2DEG mobility limited by interface roughness as a function of Δ and L has been studied in detail previously[56]. In this work, we assumed $\Delta = 0.5$ nm and $L = 15$ nm for our calculations. The 2DEG mobility limited by interface roughness scattering at room temperature was calculated for the HEMT structure shown in 4.1a for different gate voltages and different channel thicknesses. Re-

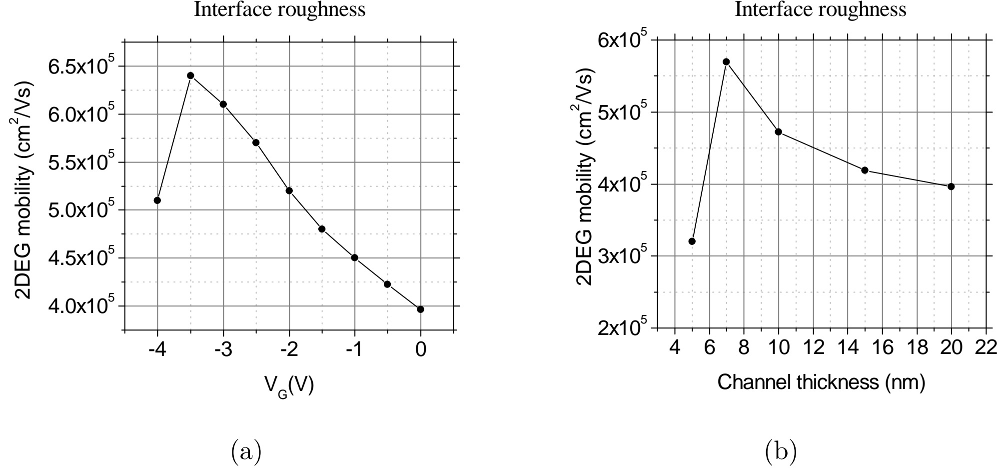

Figure 4.6: 2DEG mobility limited by Interface roughness scattering at room temperature, assuming $\Delta = 0.5$ nm and $L = 15$nm, in N-face HEMT structure shown in Fig. 4.1a for (a) different gate voltages, and (b) channel thicknesses.

sults are shown in 4.6a and 4.6b, respectively. The mobility increases with more negative gate bias and/or decreasing channel thickness up until the most negative gate bias/thinnest channel thickness investigated. At first glance $1/\tau_{IR}$ seems to be directly proportional to n_s^2 and the interface roughness limited 2DEG mobility would be expected to increase monotonically with decreasing charge density. However, the integral in 4.8 is also a function of n_s through k_F. Value of$k_F$drops with increasing charge density and this leads to the non-monotonic behavior seen in 4.6a and 4.6b.

As these calculations revealed, although the 2DEG mobility limited by the interface roughness is a function of gate reverse bias and channel thickness, however its value remains above 4×10^5cm^2/Vs, and therefore does not have a significant effect on the 2DEG mobility at room temperature.

4.3.4 Alloy disorder

In a ternary alloy such as $Al_xGa_{1-x}N$, N atoms occupy the V-sites, and Al and Ga atoms distribute randomly on III-sites in the crystal. This random distribution results in a practically non-periodic crystal, for which Block waves are no more applicable. The virtual crystal approximation has been used to overcome the complexity of extracting physical parameters in these kinds of crystals as explained in ref. [69] . The random distribution of Al and Ga atoms in the crystal leads to fluctuations in the crystal potential, and therefore, is a source of scattering.

In AlGaN/GaN heterostructures such as one shown in Fig.4.1a the 2DEG forms mostly in the binary semiconductor (GaN). However, a small portion of the 2DEG penetrates into the alloy barrier and gets scattered by the alloy scattering. The scattering rate due to alloy disorder is given in Eq.4.9[69].

$$\frac{1}{\tau_{alloy}} = \frac{m^*\Omega_0(V_A - V_B)^2 x(1-x)}{e^2\hbar^3} \times \frac{\kappa_b P_b^2}{2} \tag{4.9}$$

where Ω_0 is the volume of a unit cell of AlGaN, $V_A - V_B$ is the alloy scattering potential that results from the replacement of a Ga atom by an Al one, and is estimated by conduction band discontinuity between AlN and GaN. κ_b and P_b are respectively the decay rate and the probability of wavefunction penetration into the barrier. As explained in the beginning of this chapter, κ_b and P_b should be calculated carefully in order to get a precise approximation of the scattering rate related to the alloy disorder. In [60], the Fang-Howard approximation was used to calculate the 2DEG wavefunction while simultaneously solving the Poisson equation independent of the quantum confinement effect in AlGaN/GaN HEMT

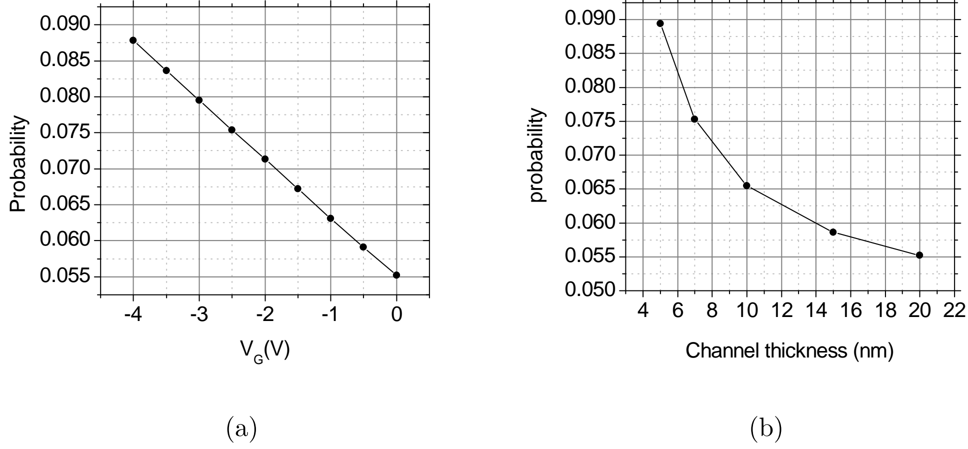

Figure 4.7: Probability of 2DEG penetration into the alloy barrier in the N-face HEMT structure shown in Fig. 4.1a for (a) different gate biases (b) different channel thicknesses

structures under reverse bias. This led to an overestimate of the alloy scattering rate in such structures. In this work, as mentioned earlier, we used BandEng to obtain the 2DEG wavefunction in the channel. The probability of 2DEG penetration into the barrier for the HEMT structure (Fig.4.1a) under reverse bias and for different channel thicknesses were calculated for the 2DEG wavefunctions obtained from BandEng and are shown in Figs.4.7a and 4.7b, respectively. As revealed by these calculations the probability of penetration increases by increasing the applied reverse bias or by decreasing the channel thickness. However, the variation is not as significant as estimated previously by Brown *et al.*[70]

The electron mobility limited by alloy scattering at room temperature was calculated for the N-face HEMT structure shown in Fig.4.1a for various gate reverse biases and channel thicknesses and is shown in Figs.4.8a and 4.8b. Both applying a reverse bias to the gate or reducing the channel thickness results in more 2DEG

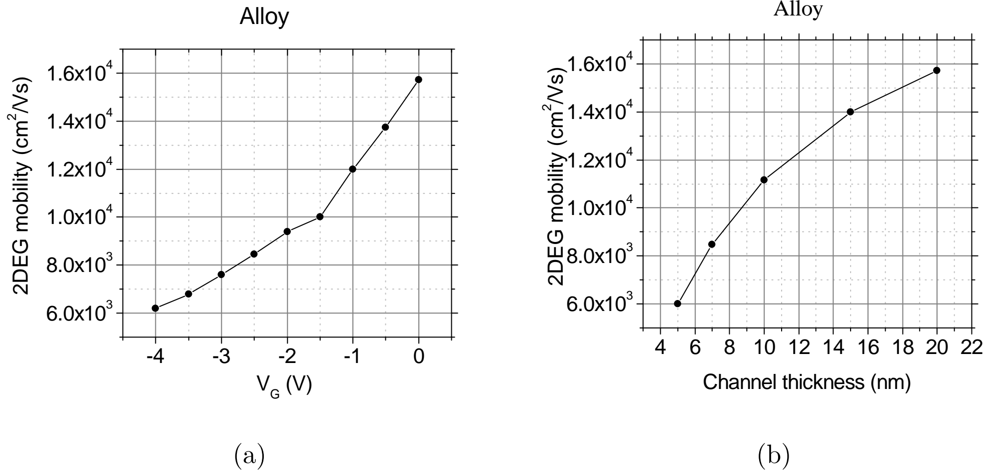

Figure 4.8: 2DEG mobility limited by alloy scattering at room temperature in N-face HEMT structure shown in Fig. 4.1a for (a) different gate voltages, and (b) channel thicknesses

penetration into the alloy barrier and increases the alloy scattering rate.

4.3.5 Remote ionized impurity

As explained in chapter 1, wurtzite III-N has a net spontaneous polarization in $\vec{c}$ direction. Moreover, tensile stress in the AlGaN lattice grown on top of GaN produces additional polarization called piezoelectric polarization. In AlGaN/GaN heterostructures the net polarization at the interface is usually enough to induce a 2DEG with high charge density (1×10^{13}- 2×10^{13}cm^{-3}) in the channel. Notwithstanding, Si-doping of the alloy (AlGaN) barrier is still used in properly designed N-Face HEMT structures [33, 51]. This Si-doping creates shallow donor states which provide electrons to the channel 2DEG. Without Si-doping, the channel 2DEG will still form, however, the electrons will be provided by deep donor states which intrinsically form at the GaN buffer/AlGaN barrier interface during growth.

It has been shown that this results in DC-to-RF dispersion and lower RF output conductance in N-Face HEMTs [71]. Proper Si-doping of the AlGaN barrier eliminates these effects.

The remote doping is usually far from the channel, and does not severely affect the 2DEG mobility at room temperature. Using Eq.4.10[56], the 2DEG mobility limited by remote ionized impurity scattering at room temperature was calculated for the HEMT structure shown in Fig.4.1a, for which the Si-doped layer is located 12 nm away from the 2DEG (t_{spacer} = 12 nm), and the Si-doping concentration (N_{imp}) is 5×10^{18} cm^{-3}. The mobility calculations were performed for different gate biases as well as different channel thicknesses, and the results are shown in Figs.4.9a and 4.9b.

$$\frac{1}{\tau_{RII}} = N_{imp} \frac{m^*}{2\pi\hbar^3 k_F^3} \left(\frac{e^2}{2\epsilon_0\epsilon_s}\right)^2 \int_0^{2k_F} dq \frac{F(q)}{\left(q + q_{TF} G(q)\right)^2} \frac{exp(-2qt_{spacer})q}{\sqrt{1 - \left(\frac{q}{2k_F}\right)^2}} \tag{4.10}$$

4.3.6 2DEG mobility considering only conventional scattering mechanisms

Considering the conventional scattering mechanisms discussed in the previous sections, the 2DEG mobility at room temperature can be calculated from Matthiessen rule given in Eq. 4.11. The 2DEG mobility for the N-face HEMT structure shown in Fig.4.1a was calculated as a function of gate reverse bias and channel thickness (Figs.4.10a and 4.10b). Although the calculated 2DEG mobility, considering all the above-mentioned conventional scattering mechanisms, drops as the charge density decreases, the drop is not as severe as observed from the experimental data. This

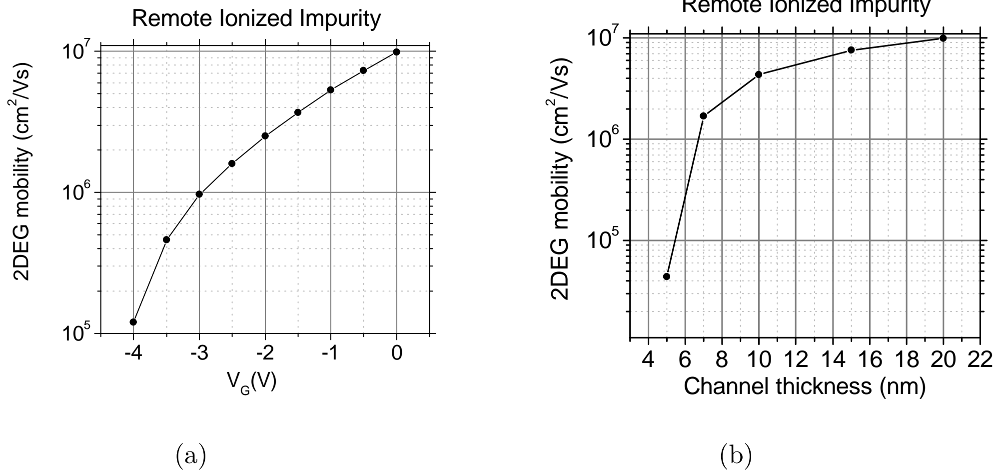

(a) (b)

Figure 4.9: 2DEG mobility limited by remote ionized impurity at room temperature in N-face HEMT structure shown in Fig. 4.1a for (a) different gate voltages, and (b) channel thicknesses.

conspiracy between the experimental results and the calculations suggests that the conventional scattering mechanisms are not enough to explain the huge drop in the 2DEG mobility occurred by decreasing the charge density in N-face HEMT structures. Two new scattering mechanisms, surface state dipoles and charged interface states, are proposed and discussed in the following sections.

$$\frac{1}{\mu} = \frac{1}{\mu_{OP}} + \frac{1}{\mu_{AP}} + \frac{1}{\mu_{IR}} + \frac{1}{\mu_{Alloy}} + \frac{1}{\mu_{RII}} + \frac{1}{\mu_{BII}} \tag{4.11}$$

4.4 Surface state dipoles

As it was discussed previously, there is a large polarization charge at the AlGaN-GaN interface. This bound polarization is only partially compensated by formation of the 2DEG in the channel, and the rest of it is compensated by the charged sur-

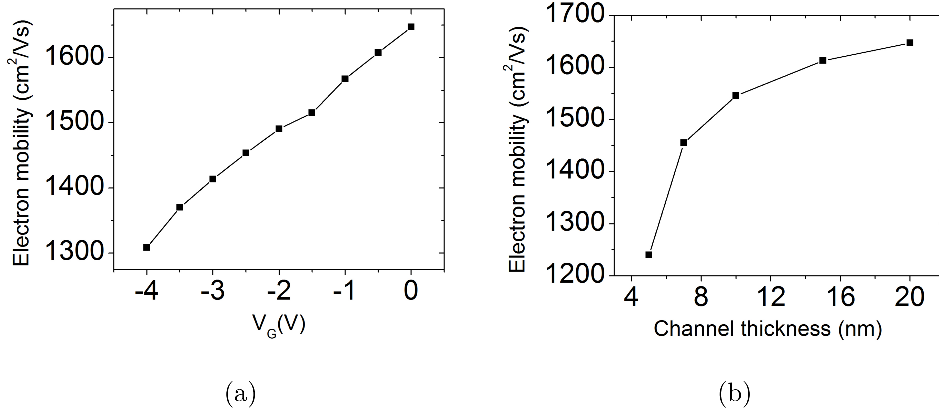

(a) (b)

Figure 4.10: 2DEG mobility at room temperature, calculated considering all conventional scattering mechanisms as a function of (a) gate reverse bias (b) channel thickness.

face states. Although the nature of these surface states is not well-understood yet, extensive dangling bonds and vacancies at the surface have been suggested as the origin of such states[18]. These charged surface states similar to remote ionized impurities are a source of electron scattering. In the case of N-face HEMT structures a dielectric (usually SiN) is deposited on the surface before fabricating transistor patterns to protect the surface from being etched in the developer. Therefore, instead of a sheet of positive charges, there is a sheet of dipoles on the surface as shown in Fig.4.11.

The formula to calculate the scattering rate from surface state dipoles can be derived using a superposition of positive and negative charges, and is given by Eq.4.12.

$$\frac{1}{\tau_{SS}} = N_{SS}\frac{m^*}{2\pi\hbar^3 k_F^3}(\frac{e^2}{\epsilon_0\epsilon_r})\int_0^{2k_F} dq\frac{F(q)e^{-2qt_{ch}}\sinh(\frac{qd}{2})}{(q+q_{TF}G(q))^2}.\frac{q^2}{\sqrt{1-(\frac{q}{2k_F})^2}} \tag{4.12}$$

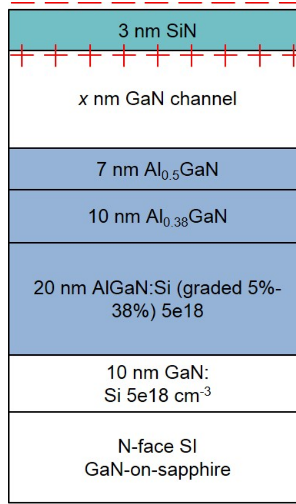

Figure 4.11: Schematic of a typical N-face HEMT structure showing the SiN dielectric and surface state dipoles.

Where d and t_{ch} are the dielectric and channel thicknesses, respectively, and $N_{SS}$is the density of surface state dipoles. The 2DEG mobility limited by surface state dipoles was calculated as a function of channel thickness and the gate reverse bias, and the results are shown in Figs.4.12a and 4.12b, respectively. The density of surface state dipoles was assumed to be 2×10^{12} cm^{-2}for our calculations[18].

The calculated 2DEG mobility revealed that, in the case of thin channels, the surface state dipoles degrades the 2DEG mobility. On the contrary, in the case of 20 nm-thick channel, these dipoles are far from the 2DEG, and their effect on 2DEG mobility at room temperature (even for large gate reverse biases) is negligible.

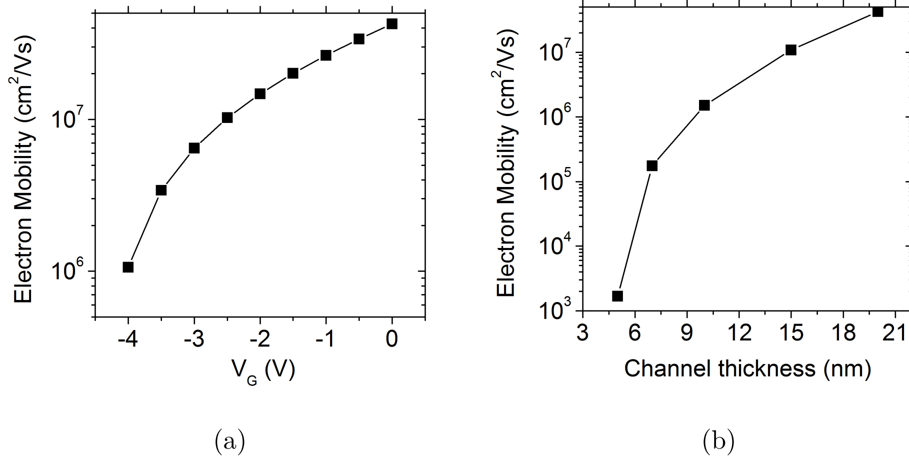

(a) (b)

Figure 4.12: 2DEG mobility limited by surface state dipoles at room temperature in N-face HEMT structure shown in Fig. 4.1a for (a) different gate voltages, and (b) channel thicknesses.

4.5 Charged interface states at the AlGaN-GaN interface

The conductance method was first proposed by Haddara and El-Sayed[72] to measure the trap state density between Si-SiO_2 interface. This method was later adobted by Miller *et al.*[61] to measure the trap state at GaN-AlGaN interface in Ga-face GaN/AlGaN heterostructure. They reported an interface state density of 1×10^{12} cm^{-2} with an energy of 0.3 eV below the conduction band. Recently, Waller *et al.*[62] showed that using conductance method for extracting interface states is valid only for HEMTs with short gate length ($L_G < 10\,\mu m$). Utilizing this method for HEMTs with long gate lengths results in exaggerated interface states. They measured an interface state density of 5×10^{10} cm^{-3} in Ga-face GaN/AlGaN

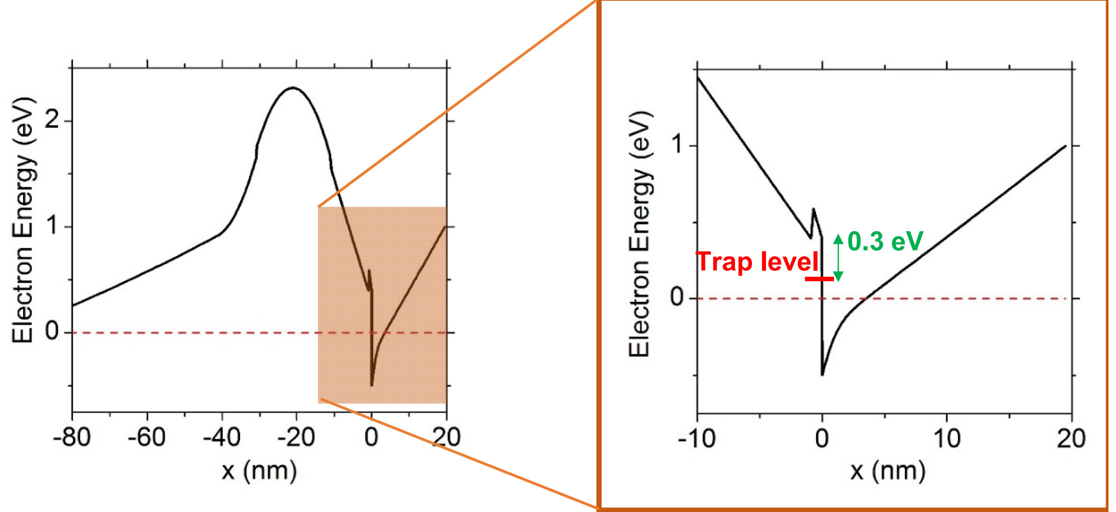

Figure 4.13: The Band diagram of N-face HEMT structure showing interface trap state at the AlGaN-GaN interface

HEMT structures. The reason behind the formation of these interface trap states is still not well-understood. They could be attributed to the AlGaN-GaN intermixing at the interface, or the large density of oxygen unintentionally incoporated into the AlGaN layer.

As shown in Fig.4.13, these trap states are above the fermi level, and therefore, depleted and positively charged. Charged trap states can be modeled similar to remote ionized impurity for the purpose of the 2DEG mobility calculations. The interface state scattering rate is then given by Eq.4.13

$$\frac{1}{\tau_{IS}} = n_{IS}\frac{m^*}{2\pi\hbar^3k_F^3}\left(\frac{e^2}{2\epsilon_0\epsilon_s}\right)^2\int_0^{2k_F}dq\frac{F(q)}{(q+q_{TF}G\left(q\right))^2}\frac{exp(-2qd)q^2}{\sqrt{1-\left(\frac{q}{2k_F}\right)^2}} \quad (4.13)$$

where a sheet of positive charge with a density of n_{IS} was assumed at the AlGaN/GaN interface. d is the distance between the charge centroid and the AlGaN/GaN interface.

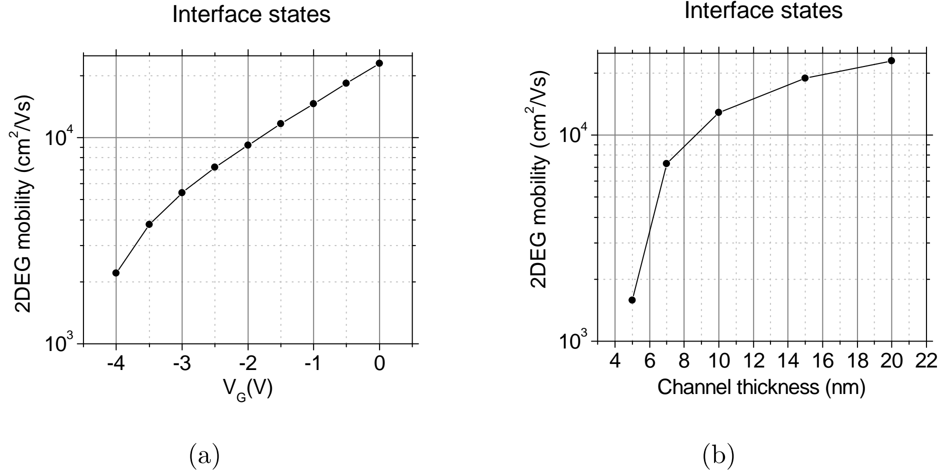

Figure 4.14: 2DEG mobility limited by AlGaN-GaN interface states at room temperature in N-face HEMT structure shown in Fig. 4.1a for (a) different gate voltages, and (b) channel thicknesses.

The 2DEG mobility limited by charged interface states at room temperature for the N-face HEMT structure shown in Fig.4.1a as a function of gate reverse bias and channel thickness was calculated assuming an interface state density of 8×10^{11}cm^{-2}. As the results shown in Figs.4.14a and 4.14b demonstrate, the mobility limited by charged interface states drops as the charge density decreases either by increasing the gate reverse bias or decreasing the channel thickness. This mobility drop is because of less screening of the scattering potential by 2DEG as the charge density decreases. Moreover, the distance between charge centroid and the interface decreases as the channel thickness is decreased or the gate reverse bias is increased which results in larger scattering rate.

The 2DEG mobility limited by interface states as a function of interface state density was also calculated for the HEMT structure shown in Fig.4.1a under gate bias of $V_G = -4$ V. The electron mobility decreases as the interface state density

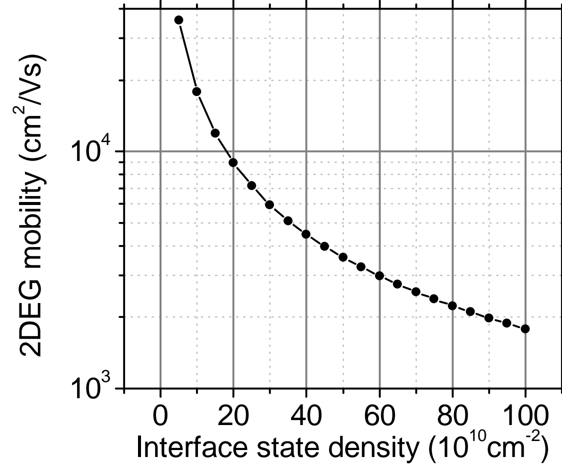

Figure 4.15: 2DEG mobility limited by the charged interface states scattering as a function of interface state density.

increases as shown in Fig.4.15.

4.6 Total 2DEG mobility and conclusion

As mentioned before, we are interested in understanding the effects of gate reverse bias and channel thickness on the electron mobility. In previous section, we studied the effect of these two variations on the 2DEG mobility limited by each scattering mechanism, individually. It was also mentioned that in a perfect GaN-based HEMT structure where the 2DEG mobility is only limited by crystal vibrations, the 2DEG mobility at room temperature is theoretically 1745 cm^2/Vs. Using Matthiessen rule the total 2DEG mobility, considering all the scattering mechanisms, is given by Eq.4.14.

$$\frac{1}{\mu} = \frac{1}{\mu_{OP}} + \frac{1}{\mu_{AP}} + \frac{1}{\mu_{IR}} + \frac{1}{\mu_{Alloy}} + \frac{1}{\mu_{RII}} + \frac{1}{\mu_{BII}} + \frac{1}{\mu_{IS}} + \frac{1}{\mu_{SS}} \tag{4.14}$$

Where μ is the 2DEG mobility, and μ_{OP}, μ_{AP} , μ_{IR} , μ_{Alloy} , μ_{RII} , μ_{BII} , μ_{IS} , and μ_{SS} are the electron mobility limited by optical phonons, acoustic phonons, interface roughness, alloy barrier, remote ionized impurity, background ionized impurity, interface states, and surface state dipoles, respectively. The 2DEG mobility at room temperature for the HEMT structure shown in Fig.4.1a was calculated for different gate voltages, and channel thicknesses, and is shown in Figs.4.16a, and 4.16b, respectively. As illustrated in these figures, increasing the gate reverse bias and decreasing the channel thickness, reduce the 2DEG mobility. This trend has been observed by experiment as well. Previously, it was believed that increasing the gate reverse bias or decreasing the channel thickness in N-face GaN-based HEMT structures lead to deeper penetration of the 2DEG wavefunction into the barrier, and consequently, higher interface roughness and alloy scattering rates. Our calculations revealed that the penetration of the 2DEG into the barrier and, therefore, 2DEG mobility limited by alloy and interface roughness scattering mechanisms do not vary significantly by increasing gate reverse bias or decreasing the channel thickness. Therefore, these two scattering mechanisms are not enough to explain the significant drop in the 2DEG mobility observed in experiments. Rather, our calculations clearly demonstrate that the charged trap states at the AlGaN/GaN channel interface are responsible for the large reduction in 2DEG mobility seen with increasing reverse gate bias and decreasing channel thickness.

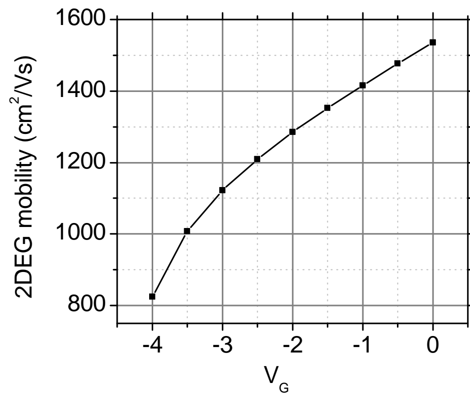

(a)

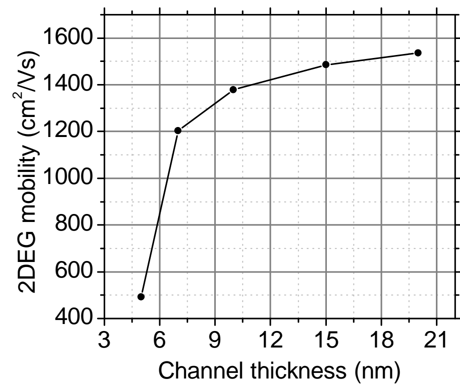

(b)

Figure 4.16: 2DEG mobility in N-face HEMT structure shown in Fig[fig:HEMT-structure] for (a) different gate voltages, and (b) channel thicknesses.

Chapter 5

Alloy Clustering Scattering

5.1 Introduction

In recent years, AlGaN/GaN and InAlN/GaN heterostructures have attracted attention from industries requiring high-power and high-frequency high-electron-mobility transistors (HEMTs).[73, 6, ?] One of the key factors in determining the quality of HEMTs is the mobility of the two-dimensional electron gas (2DEG). Therefore, analysis of the individual scattering mechanisms limiting the 2DEG mobility is paramount. The scattering mechanisms originating from acoustic and optical phonons, interface roughness, threading dislocations[36, 55], and ionized impurities have been studied extensively in the literature.[57, 74] In heterostructures with an alloy channel or barrier, alloy disorder scattering adds to all above-mentioned mechanisms to reduce the mobility. The scattering of electrons in an alloy occurs as a result of random disorder in the alloy composition, which is a well-known phenomenon.[75, 76] In the case of heterostructures with a binary compound semiconductor as the channel, like InAlN/GaN and AlGaN/GaN, the

2DEG is confined mainly in the binary material. However, the tail of the wavefunction still penetrates the ternary barrier because of the finite depth of the quantum well.[60, 69] The mobility of the electrons that penetrate the barrier are influenced by alloy disorder scattering. In addition, an alloy barrier can also affect the mobility of electrons in the binary material via alloy clustering. Alloy clustering, which is generally a consequence of differences in adatom diffusivities during growth, makes the barrier composition non-uniform and locally alters the polarization and conduction band discontinuities along the channel (Fig. 1). This leads to fluctuations in the energy levels of the channel, which behave as a perturbation potential and scatter the electrons in the 2DEG.[77]

Decreasing the gate length of a HEMT is essential to improving its high-frequency operation. As the gate length is reduced, the vertical distance between the gate and channel needs to be reduced to maintain effective gate control.[78] However, minimizing the barrier thickness in conventional Ga-face AlGaN/GaN heterostructures decreases the charge density in the channel, which consequently results in higher sheet resistance. Therefore, the Al content of the barrier needs to be increased as the barrier thickness is reduced to maintain a high charge density in the channel. Experimental data in the literature reveals a poor 2DEG mobility in AlGaN/GaN heterostructures with high Al content.[79, 80] This is contrary to what we expect from calculations of alloy disorder scattering. Despite an increase in interface roughness scattering with higher 2DEG charge density, mobility should not significantly degrade since alloy disorder scattering is reduced. As the Al content of the AlGaN barrier increases, the probability of finding electrons in the alloy barrier decreases, so the mobility of the 2DEG should improve due to reduced

alloy disorder scattering. However, increasing the Al content in the AlGaN barrier increases the likelihood of alloy clustering, which can explain the discrepancy between experimental data and calculations.

InAlN barriers are a promising alternative to AlGaN barriers. $In_{0.18}Al_{0.82}N$ presents the advantage of being lattice-matched to GaN and exhibiting a high spontaneous polarization charge, making it suitable for use as the barrier layer in ultra-scaled HEMTs.[81] However, InAlN needs to be grown at lower temperatures than AlGaN, which reduces adatom diffusivity and increases the probability of alloy clustering. In this article, a model was derived to calculate the 2DEG mobility limited by alloy clustering scattering. We then use atom probe tomography to demonstrate the random nature of the fluctuations in the alloy composition. The limiting mobility from alloy clustering is also calculated for various fluctuation amplitudes and cluster sizes. Moreover, the effect of alloy clustering on limiting the 2DEG mobility is compared for both InAlN/GaN and AlGaN/GaN heterostructures.

5.2 Derivation

In order to model the contribution of alloy clustering to limiting the 2DEG mobility, we followed the approach that was used by H. Sakaki *et al.*[63]. to calculate interface roughness scattering. In the case of interface roughness, changes in the width of quantum well cause fluctuations in the energy levels of the 2DEG, whereas in the case of alloy clustering, variations in the depth of the quantum well change the energy levels. Therefore, a local change in the composition ($\Delta X(r)$) results in

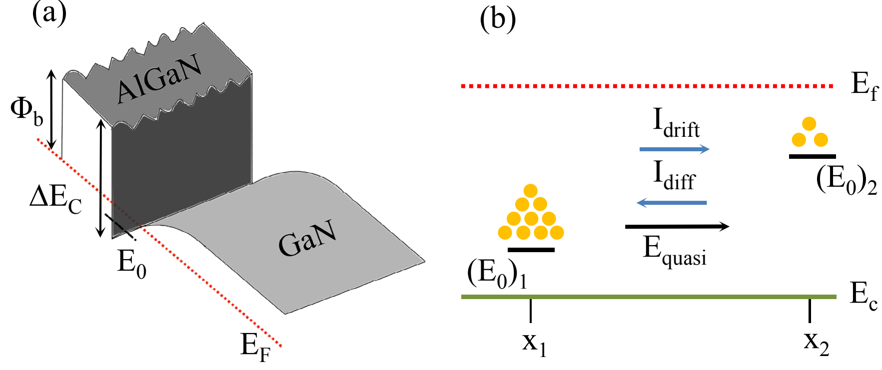

Figure 5.1: (a) Band structure of an AlGaN/GaN heterostructure showing the fluctuations in barrier height as a result of fluctuations in the barrier composition. (b) Schematic of ground state fluctuations along the channel. The Fermi level is assumed to be pinned at the surface and is constant along the channel.

a local variation in the ground state energy ($\Delta E_0(r)$), as shown in Eq. 5.1

$$\Delta E_0(r) = \partial E_0/\partial X \, \Delta X(r) \tag{5.1}$$

where r refers to the position in the heterointerface. It should be noted that we have assumed all electrons in the channel are accumulated in the first sub-band. Therefore, only local variations in the ground state energy are considered. The composition fluctuations can be characterized using the auto-covariance (AC) function, which measures the probability that the compositions at r' and r are the same. Due to the random nature of the fluctuations in composition, this probability should decrease as the distance $r - r'$ increases. Following similar works on interface roughness[63], we assume the AC function can be estimated by a Gaussian function as shown in Eq. 5.2,

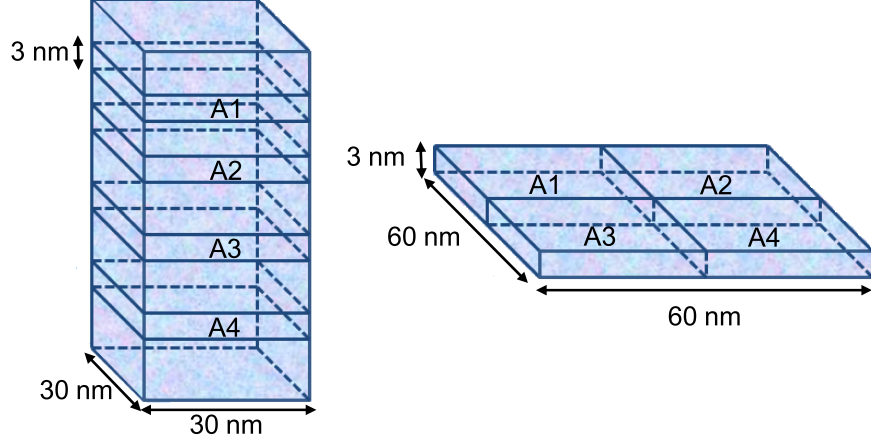

Figure 5.2: To obtain a significant number of sampling points, a 60 × 60 nm^2 in-plane composition map was generated by combining four 30 × 30 nm^2 composition maps extracted from different regions in the AlGaN layer

$$< \Delta X(r)\, \Delta X(r') >= \Delta^2 exp(-\frac{(r-r')^2}{\zeta^2}) \tag{5.2}$$

where Δ and ζ are the amplitude of fluctuations and AC length, respectively. Alloy composition fluctuations can be quantified with atom probe tomography (APT). APT is a destructive technique through which the 3D atomic distribution of heterostructures is mapped[82].

To extract the parameters of the Gaussian distribution shown in Eq. 5.2, we followed the work done by S. M. Goodnick *et al.*[83] in which high-resolution transmission electron microscopy was used to determine interface roughness parameters. Hence, the scattering matrix elements of the perturbation potential can be expressed as

$$M^2_{k'k} = \int exp\left(j\,\overrightarrow{k}'.\overrightarrow{r}\right) \nabla E_0\,(r)\, exp\left(-j\,\overrightarrow{k}.\overrightarrow{r}\right) d^3r \tag{5.3}$$

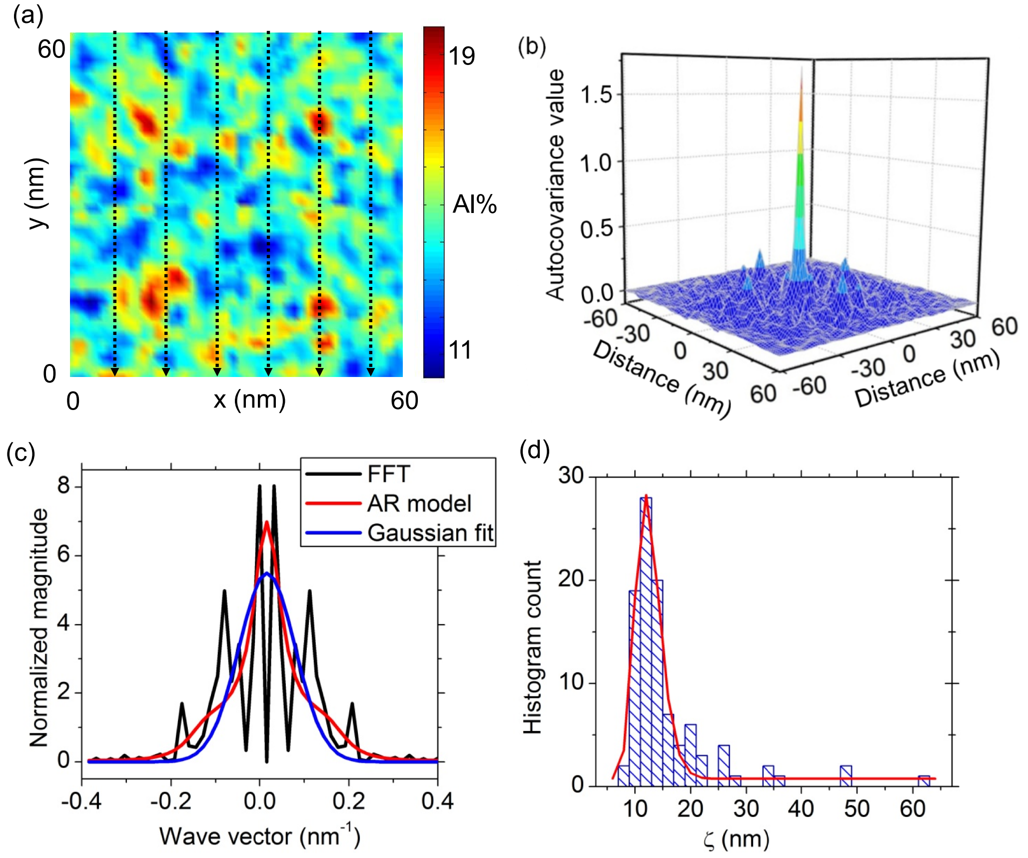

Figure 5.3: (a) 2D III-site composition map of the in-plane Al distribution in an $Al_{0.15}Ga_{0.85}N$ layer (Black arrows illustrate the directions along which the AC lengths were calculated). (b) AC sequence of digitized data shown in part (a). (c) An example of the power spectrum calculated using both the FFT and AR methods and the fitted Gaussian function. (d) Histogram of AC lengths obtained from different areas on the 2D III-site composition map.

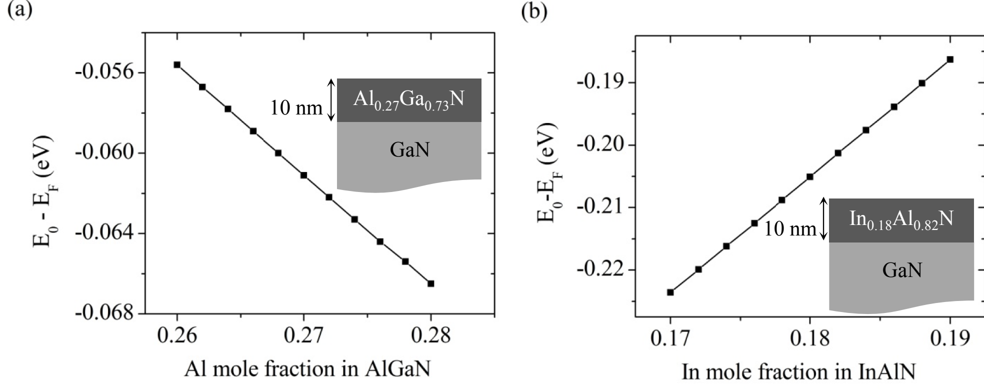

Figure 5.4: Ground state energy of the 2DEG as a function the alloy composition calculated using BandEng for (a) $Al_{0.27}Ga_{0.73}N/GaN$ and (b) $In_{0.18}Al_{0.82}N/GaN$.

which can be simplified to the following equation according to the Fourier transform of a Gaussian function:

$$M^2_{k'k} = \pi \left(\partial E_0/\partial X\right)^2 \, \Delta^2 \, \zeta^2 exp\left(-\left(\zeta^2 q^2\right)/4\right) \tag{5.4}$$

where $\overrightarrow{q} = \overrightarrow{k} - \overrightarrow{k}'$ is the 2D scattering wave vector. In the relaxation time approximation, the momentum relaxation time τ is given by

$$\frac{1}{\tau\left(E\right)} = \left(\frac{1}{4\pi 2}\right)\left(\frac{2\pi}{\hbar}\right)\int M_{k'k}(q)^2 \left(1 - \cos\left(\theta\right)\right)\delta\left(E_0^{k'} - E_0^{k}\right) \tag{5.5}$$

The energy of the electron is assumed to remain unchanged after scattering. The scaling factor $1 - \cos\left(\theta\right)$ takes into account that large-angle scattering has a greater impact on momentum relaxation. Contrary to calculations done by H. Sakaki *et al.* [63], we did not use the Thomas-Fermi screening factor in our calculations. Large angle scattering is dominant since small angle scattering does not significantly decrease the mobility. However, large angle scattering occurs at wave vectors near $2k_F$. These wave vectors correspond to wavelengths comparable

to the inter-electron spacing. Screening is unlikely to be effective at these distances. Moreover, the Thomas-Fermi approximation to the dielectric constant of the electron gas is a quasi-static approximation which is applicable only at long wavelengths ($q/kF << 1$)[84]. Therefore, this is only relevant if we are trying to screen the long-range part of Coulomb interaction[85]. Although, as explained intuitively in the following section, the charge density along the channel rearranges itself as a result of quasi electric field caused by variations in the ground state. This rearrangement can moderate the electron scattering from fluctuations in the barrier composition. Fluctuations in the ground state (E_0) generate a varying quasi-electric field that provides a driving force for electrons to move along the channel. Since the 2DEG charge density (n_s) is proportional to the difference of the Fermi level and the ground state ($E_F - E_0$), the charge density fluctuates with changes in $E_F - E_0$. The gradient in charge density generates a diffusion current in opposition to the drift current generated by the quasi-electric field. Fig. 5.1(b) is a simple illustration of these two currents in the channel. The value of $E_F - E_0$ is larger at x_1 than x_2 which results in higher charge density at x_1. Because of the lower energy state at x_1, electrons at x_2 prefer to move toward x_1. In addition, the gradient in the charge density causes electrons to diffuse from x_1 to x_2. These two currents cancel each other out to balance the driving forces from the quasi-electric field and charge density gradient. The direction and magnitude of this electric field depends on which current is dominant. Depending on the direction of the generated electric field, the conduction band (and consequently the ground state) at x_2 will be either lowered or raised, which results in the screening or exacerbation of fluctuations in the ground state, respectively. The drift current (I_{drift}) and

diffusion current (I_{diff}) that result from the quasi-electric field and gradient in the charge density along the channel, respectively, are defined by the following:

$$I_{drift} = \mu_{tot}(\nabla E_0)/\nabla L,\ I_{diff} = D\frac{q\Delta n_s \times d}{\Delta L} = \mu\frac{k_B T}{q}\frac{q\nabla n_s \times d}{\Delta L} = \mu_{tot}k_B T\frac{\Delta n_s \times d}{\Delta L} \tag{5.6}$$

where μ_{tot} is the total 2DEG mobility considering all scattering mechanisms, ΔL is the lateral distance between two points with different ground states (assumed to be equal to the AC length (ζ)), d is the channel thickness which can be defined as full width at half maximum of the 2DEG wavefunction in AlGaN/GaN heterostructures.

To examine the extent to which this electric field can screen or aggravate the fluctuations in the ground state, we calculated the diffusion and drift currents for a specific variation in the AlGaN composition. As calculated by BandEng[52], a 2% change in the Al mole fraction in the barrier of $Al_{0.27}Ga_{0.73}N$/GaN heterostructure causes a change of 0.0032 eV for $E_0 - E_F$ and 3×10^{11} cm^{-2} for the charge density. The I_{drift} and I_{diff} corresponding to these values are $0.0032\mu_{tot}/\Delta L$ and $0.003\mu_{tot}/\Delta L$, respectively. Hence, these opposing currents are effectively equal, and the screening effect can be safely ignored. We then calculate the limiting mobility using

$$\mu = \frac{e}{m*} < \tau(E) >= \frac{\left(\int \tau(E)\, E\frac{\partial f_0(E)}{\partial E} dE\right)}{\left(\int E\frac{\partial f_0(E)}{\partial E} dE\right)} \tag{5.7}$$

where e and $m*$ are the electron charge and effective mass, respectively, and $f_0(E)$ is the Fermi-Dirac distribution function. As an intuitive explanation, the $E\frac{\partial f_0(E)}{\partial E}$

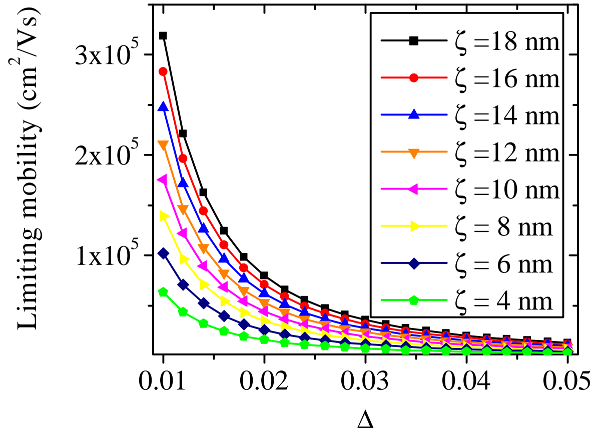

Figure 5.5: Plot of the mobility limited only by alloy clustering in the barrier as a function of the mean amplitude of fluctuations in mole fraction (Δ) for various cluster sizes. This limit is independent of temperature.

term in Eq. 5.7 originates from averaging the momentum relaxation time over the energy of electrons in an attempt to calculate the current density of electrons[86]. Eq. 5.7 can be simplified to $\mu = e\tau(E_F)/m*$ in the case of a 2DEG because all electrons are assumed to move very close to the surface of the Fermi sphere. It should be noted that the mobility limited by alloy clustering is temperature-independent, much like the mobility limited by interface roughness.

5.3 Atom probe tomography analysis

To determine the amplitude and distribution of random composition fluctuations, APT was performed on the $Al_{0.15}Ga_{0.85}N$ electron blocking layer of a commercial c-plane (0001) GaN LED. The in-plane Al distribution in the $Al_{0.15}Ga_{0.85}N$ layer was reconstructed by averaging the Al mole fraction over 3 nm along the c-axis. To obtain a significant number of sampling points, a 60×60 nm^2 in-plane composi-

tion map (Fig. 5.3(a)) was generated by combining four 30×30 nm^2 composition maps extracted from different regions in the AlGaN layer as shown in fig. 5.2. The above-mentioned digitalized data was then used to calculate the 2D AC as demonstrated in Fig. 5.3(b). The root mean square (rms) value of Al composition fluctuations (Δ) was obtained from the zeroth coefficient of the 2D AC sequence and was estimated to be 1.14%. To estimate the AC length, the composition profile was taken along the directions shown in Fig. 5.3(a), and the AC function was calculated for each profile. Since the Fourier transform of the AC function (the power spectrum) is included in the relaxation time formula (Eq. 5.5) rather than the AC function itself, it is preferable to estimate the power spectrum. Fast Fourier transform can be used to calculate the power spectrum. However, it leads to severe fluctuations around the actual power spectrum as demonstrated in Fig. 5.3(c). Therefore, the auto-regressive (AR) model was used for this purpose[83]. The AC lengths (ζ) were then obtained by fitting a Gaussian function to the power spectrums of the 1D composition sequences that were taken along the directions indicated by the arrows in Fig. 5.3(a) The distribution of ζ-values was characterized by a log-normal function and is plotted in Fig. 5.3(d). The AC length was estimated to be 12.3 nm from the expectation value of the log-normal distribution fit.

5.4 Simulation

To study the effect of the aforementioned composition fluctuations on limiting the 2DEG mobility, we assumed an average In (Al) mole fraction of 0.18 (0.27) for In-

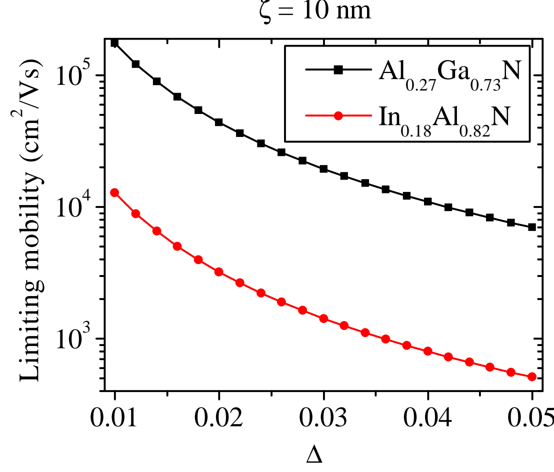

Figure 5.6: Comparison of the effect of alloy clustering on the mobility of 2DEG between AlGaN/GaN and InAlN/GaN heterostructures. The x-axis is the mean amplitude of fluctuations in mole fraction.

AlN (AlGaN) in our calculations. As mentioned previously, the $In_{0.18}Al_{0.82}N$/GaN heterostructure is particularly attractive for HEMTs since it is a nominally stress-free heterostructure and yields a high-density 2DEG. The Al mole fractions of AlGaN barriers in state-of-the-art AlGaN/GaN HEMTs are generally between 0.2 and 0.3, due to the trade-off in charge and mobility[87].

To calculate $\partial E_0/\partial X$, we solved the Schrodinger-Poisson equation self-consistently using BandEng software[52]. The parameters used in calculations for each heterostructure are reported in Table I. The ground state energy of the 2DEG in AlGaN/GaN (InAlN/GaN) were calculated as a function of Al (In) mole fractions around 0.27 (0.18), as shown in Fig. 5.4. $\partial E_0/\partial X$ was then determined from the slope of the curve to be -0.5 eV and 1.85 eV for $Al_{0.27}Ga_{0.73}N$/GaN and $In_{0.18}Al_{0.72}N$/GaN, respectively. By entering these values in Eq. 5.4, we calculated the mobility limited by alloy clustering for different AC lengths and fluctuation

	GaN	$Al_xGa_{1-x}N$	$In_xAl_{1-x}N$
m_e^*/m_e	0.2	0.2+0.2x	0.4-0.29x
E_g(eV)	3.4.	$3.42+1.86x+1x^2$	$6.28-8.51x+3x^2$
ΔE_c(eV)	–	$1.24x+0.66x^2$	$1.9-5.56x+1.96x^2$
ε_r	8.9	8.9+0.4x	8.5+6.8x

Table 5.1: Materials parameters used in BandEng to calculate the ground state energy. m_e^*/m_e is the ratio of the electron effective mass to the electron mass. E_g, ΔE_c, and ε_r are bandgap, conduction band discontinuity with respect to GaN, and the relative permittivity, respectively.

amplitudes.

Fig. 5.5 demonstrates the mobility limited by alloy clustering as a function of fluctuation amplitude for different AC lengths. The mobility limited by alloy clustering decreases as the fluctuation amplitude increases, as expected. Also, from the dependence of matrix elements $M^2_{k'k}$ on ζ shown in Eq. 5.4, we expect the mobility to first decrease with increasing AC length until it reaches a minimum and then start increasing. However, in this work we only calculated the limiting mobility for the AC lengths in the range of 4 to 18 nm, which are more likely to be experimentally observed.

We then compared the significance of alloy clustering to mobility limitation between $In_{0.18}Al_{0.82}N$/GaN and $Al_{0.27}Ga_{0.73}N$/GaN heterostructures in Fig. 5.6. Since the bandgap and polarization difference between AlN and InN is much higher than that between AlN and GaN, fluctuations in InAlN composition affect the mo-

bility more significantly than fluctuations in AlGaN composition. As a result, the limiting mobility for the same fluctuation amplitude and AC length is lower for the InAlN/GaN heterostructure in comparison with the AlGaN/GaN heterostructure. It should be noted that due to the large difference in the atomic size between In and Al and difference in the bonding energy between Al-N and In-N[2], lower growth temperatures are required for InAlN than AlGaN. Poor Al adatom diffusion at low growth temperatures can lead to severe clustering in InAlN which has been shown to result in a honeycomb microstructure in certain conditions[41, 88, 4].

In AlGaN/GaN and InAlN/GaN heterostructures, inserting a thin AlN interlayer at the heterointerface effectively suppresses the penetration of the 2DEG wavefunction into the barrier, consequently enhancing the 2DEG mobility[89]. In this work, we investigated the influence of AlN interlayer on reducing the scattering from alloy clustering. As shown in Fig. 5.7, including a 3-nm-thick AlN layer between the channel and the InAlN barrier enhances the limiting mobility by a factor of 1.6. The barrier height in an InAlN/AlN/GaN HEMT structure is defined solely by the conduction band discontinuity between GaN and AlN. However, the charge density in the channel depends on the composition of InAlN barrier. Thus, variations in InAlN composition can change the charge density in the channel of InAlN/GaN heterostructure and consequently create fluctuations in the ground state energy.

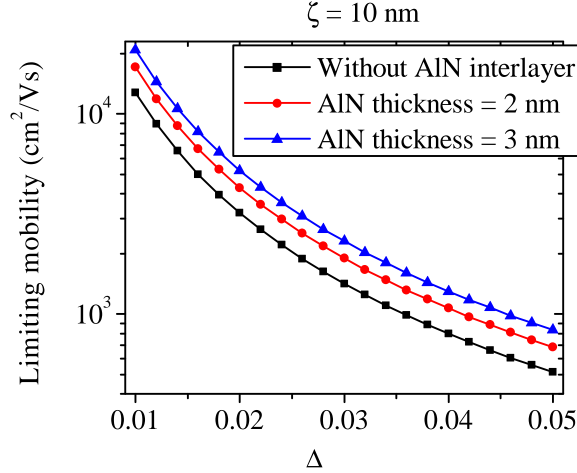

Figure 5.7: Plot of 2DEG mobility limited by alloy clustering as a function of the mean amplitude of fluctuations in mole fraction (Δ) for different AlN interlayer thicknesses in InAlN/AlN/GaN structures.

5.5 Summary

In summary, we calculated the contribution of alloy clustering to limiting the mobility of 2DEG for various structures. Comparisons were also made between limiting mobility of alloy clustering between $Al_{0.27}Ga_{0.73}N$/GaN and $In_{0.18}Al_{0.82}N$/GaN heterostructures, demonstrating that alloy clustering has more influence on limiting the 2DEG mobility in InAlN/GaN heterostructures in comparison to AlGaN/GaN heterostructures for the same auto-correlation length and amplitude of composition fluctuations. We also showed that inserting a thin AlN interlayer between the barrier and the channel increases the mobility limited by alloy clustering. However, the AlN interlayer cannot completely eliminate the scattering from alloy clustering.

Chapter 6

Analysis of reverse-bias leakagein GaN Schottky diodes

Introduction

Minimizing the leakage current through unintentionally doped (UID) GaN layers is essential for both lateral and vertical III-N electronic devices[90, 91, 92, 93]. Previous studies have shown that the magnitude of the leakage current in GaN-based electronic devices grown by both metal organic chemical vapor deposition (MOCVD) and plasma-assisted molecular beam epitaxy (PAMBE) is correlated with the screw component of threading dislocation density [94, 95, 96, 97]. Particularly, Northrup [98] has shown that in the case of Ga-rich growth by PAMBE, Ga-filled screw dislocations are energetically preferred to hollow ones. These Ga-filled cores create electronic states throughout the bandgap which generates leakage paths.

Hsu et al. have shown that the reverse-bias leakage current (RLC) in GaN

Schottky diodes (SD) grown by PAMBE depends on the III/V ratio[95]. Their study revealed that the electrical activity of screw dislocations depends on the growth conditions. In particular, they were able to suppress the leakage current by 2-4 orders of magnitudes by growing GaN in a Ga-lean regime as opposed to a Ga-rich regime. However, growing in a Ga-lean regime resulted in a pitted morphology; this is undesirable in epitaxially grown heterostructures that often include thin layers. Ex-situ treatments such as surface modification with an atomic force microscope, and electrochemical treatment of the diode surface were suggested to decrease the leakage current[99, 100].

There are two different methods for MBE growth of III-N materials: PAMBE and ammonia MBE. PAMBE relies on an N_2 plasma source to supply active N to the substrate surface, where it is adsorbed. In ammonia MBE, active N is created via thermal decomposition of ammonia at the heated substrate.

In the case of ammonia MBE, it was shown that increasing the V/III ratio improves the structural quality of epitaxial GaN[101, 102]. In fact, growing GaN in a metal-rich regime by ammonia MBE results in extremely rough surfaces. Therefore, electronic device structures grown by this method are usually grown in a N-rich regime[103]. Kyle et al.[104] studied the dependence of electron mobility in GaN on the flow rate of ammonia and achieved the highest electron mobility by growing with an ammonia flow rate of 1000 sccm.

It is believed that the vertical leakage in GaN-based devices grown by ammonia MBE is lower than for PAMBE. Since ammonia MBE material is grown in a N-rich regime, Ga atoms do not accumulate along the dislocations and additional conductive pathways do not form. Nonetheless, a systematic comparison of vertical

leakage in devices grown by these two techniques has not yet been completed.

In this work, we study the effect of different growth regimes and dislocation densities on the RLC in GaN Schottky diodes grown by PAMBE. We also study the RLC in Schottky diodes grown by ammonia MBE for two different ammonia flow rates and compare these with samples grown by PAMBE.

Experiment

PAMBE samples (PA-A,B,C,D and E) were grown in a Varian Gen-II MBE system, equipped with conventional Knudsen effusion cells as Ga and Si sources and a Veeco Unibulb radio frequency (rf) plasma N source. The N source consisted of ultrahigh-purity (99.9995%) N_2 gas flowing at 0.7 sccm through the rf-plasma source with 250 W rf power, which corresponded to a growth rate of 4 nm/min for metal-rich GaN layers.

The ammonia samples (NH_3-A and B) were grown in a Veeco Gen 930 molecular beam epitaxy system. The system has conventional effusion cells for Ga and Si. Purified NH_3 was delivered into the growth chamber through an unheated shower-head injector. Ammonia flow rates of 200 and 1000 sccm were used for sample A and B, respectively, to explore the effect of ammonia flow rate on the RLC.

All substrates were backside metallized with 500 nm of Ti for uniform thermal coupling with the heater. Substrate temperatures were measured by an optical pyrometer calibrated to the melting point of Al. All samples in this study except PA-D were grown on GaN-on-sapphire substrates grown by MOCVD with threading dislocation densities (TDD) of $\sim 5 \times 10^8$ cm^{-2}. To study the effect of TDD on

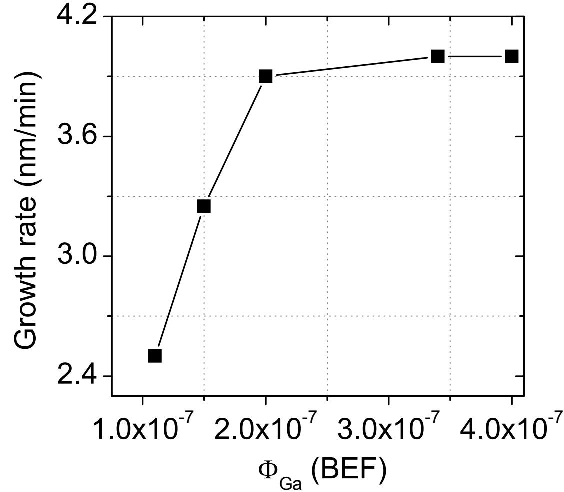

Figure 6.1: Growth rate of GaN versus Ga flux for calibration samples grown by PAMBE. The Ga flux needed to achieve stoichiometry at 700 °Cwas determined from this curve to be around 2.2×10^{-7}.

the RLC, Sample PA-D was grown on a Lumilog free-standing (FS) GaN substrate with a TDD of $\sim 5 \times 10^{7}$ cm^{-2}.

First, five calibration samples were grown by PAMBE using different Ga fluxes at a constant substrate temperature (T_{sub}) of 700 °C to determine the growth rate and the stoichiometry Ga flux[105]. The growth rate as a function of Ga beam equivalent pressure (BEP) is plotted in Fig6.1.

Two samples were grown in N-rich regime for which the growth rate is limited by the metal flux, and the other three samples were grown above stoichiometry (metal-rich), where the growth rate is limited by the available supply of active N. From this curve, the BEP of Ga needed to achieve stoichiometry was determined to be around 2.2×10^{-7} Torr. Ga BEP of 3.4×10^{-7}Torr and 4.0×10^{-7}Torr both corresponds to Ga-rich regime. The former one leads to Ga intermediate regime in which Ga forms an auto-regulated bi-layer on the surface. Whereas, the latter

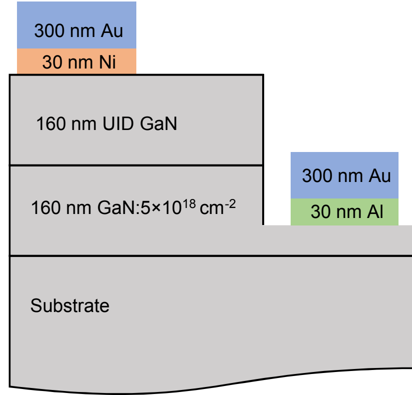

Figure 6.2: Schematic of the Schottky diode device structure. The ohmic and Schottky metal stacks are also shown.

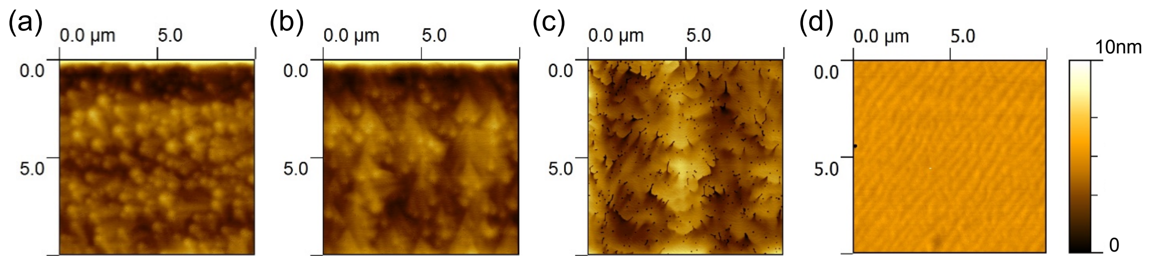

Figure 6.3: AFM images of samples grown by PAMBE. (a) PA-A (b) PA-B (c) PA-C (d) PA-D.

one corresponds to droplet regime for which the Ga flux is more than the required flux for auto-regulation and the excess Ga accumulates into droplets[106].

In the first series, four samples (PA-A, B, C, E) were grown by PAMBE with three different Ga fluxes on GaN-on-sapphire templates. The structure consisted of 160 nm of Si-doped GaN with a Si concentration of $\sim 5\times10^{18}$cm^{-3}, followed by 160 nm of unintentionally-doped (UID) GaN (Fig6.2). For all samples, the Si-doped layer was grown in the Ga-droplet regime and the substrate temperature was 700 °C.

The growth was monitored with reflection high-energy electron diffraction (RHEED). The RHEED pattern remained streaky throughout the growth on all the samples which is a signature of a smooth growth[105, 107]. The UID layer on samples PA-A and PA-E was grown with Ga BEP of 4×10^{-7}. This Ga flux corresponded to growth in a slightly Ga-droplet regime where Ga adatoms accumulate into droplets if not desorbed properly during the growth[108]. For these samples, the intensity of the RHEED pattern became dim at the beginning of the growth, which confirms that the surface was covered in a Ga bilayer[106]. The growth on sample PA-A was interrupted for 30 seconds every 10 minutes to desorb the excess Ga on the surface, and prevent Ga accumulation, whereas sample PA-E was grown without any interruption during the growth. After the growth on sample PA-E was finished, 3 minutes passed before the RHEED intensity started recovering. Still Ga droplets were visible in an optical microscope, and were removed by HCl before diode fabrication. Sample PA-B and PA-C were grown with Ga BEPs of 3.4×10^{-7}Torr and 2.4×10^{-7}Torr which corresponded to the intermediate regime, and around the stoichiometry regime, respectively. On sample PA-B, the RHEED intensity became dim as the growth began and started increasing immediately after the growth was stopped. This verifies that the GaN surface was covered with a bilayer of Ga but the Ga did not form droplets on the surface during growth. The RHEED intensity did not become dim during growth of sample PA-C which implies the Ga coverge was less than a bilayer [106]. A list of all the samples, their growth conditions and substrate material is shown in Table 6.1.

Atomic force microscopy (AFM) images of the sample surfaces are shown in Fig6.3. Samples PA-A and PA-B both have smooth surfaces, with spiral hillock

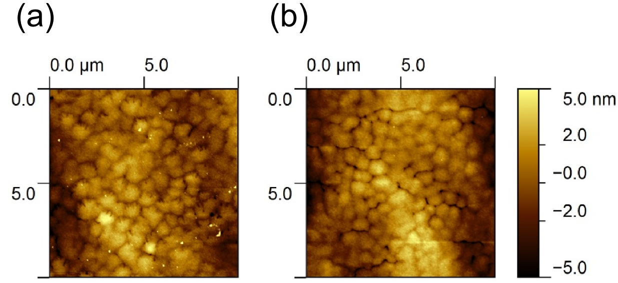

Figure 6.4: AFM images of samples grown by ammonia MBE. (a) NH_3-A (b) NH_3-B

morphology, and root mean square (rms) surface roughness values of 0.77 and 0.63 nm, respectively. Sample PA-C has smooth surface morphology between deep and large pits with an rms roughness value of 0.94nm. Sample PA-D was grown with the same growth conditions as sample PA-A, but on a Lumilog FS GaN substrate. Straight step edges were observed on PA-D and the surface is very smooth with an rms surface roughness of 0.2 nm. All roughness values were measured in a $2 \times 2\ \mu m^2$area.

In the second series, two samples (NH_3-A,B) with the same structure shown in Fig6.2 were grown at a substrate temperature of 820 °C using ammonia as the source of active N. The ammonia flow rates (FR) were set to 200 and 1000 sccm for samples NH_3-A and NH_3-B, respectively, resulting in a N-rich growth regime for both. Therefore, the growth rate is expected to be limited by the Ga flux, and, accordingly, constant on both samples. Nevertheless, the growth rate was measured to be 3.8 nm/min and 2 nm/min for 200 and 1000 sccm FRs, respectively. Reduction in the growth rate with increasing ammonia flow rate has been seen previously by Lang *et al.* [109], and was attributed to the loss of incident Ga through gas-phase scattering processes. The surface morphology

Samples	Φ_{Ga}(Torr)	NH_3 FR (sccm)	T_{sub}	TDD (cm^{-2})	r_{rms}(nm)
PA-A	4.4×10^{-7}	–	700 ºC	$\sim 5 \times 10^{8}$	0.77
PA-B	3.4×10^{-7}	–	700 ºC	$\sim 5 \times 10^{8}$	0.63
PA-C	2.4×10^{-7}	–	700 ºC	$\sim 5 \times 10^{8}$	0.94
PA-D	4.4×10^{-7}	–	700 ºC	$\sim 5 \times 10^{7}$	0.2
PA-E	4.4×10^{-7}	–	700 ºC	$\sim 5 \times 10^{8}$	NA
NH_3-A	–	200	820 ºC	$\sim 5 \times 10^{8}$	0.77
NH_3-B	–	1000	820 ºC	$\sim 5 \times 10^{8}$	0.51

Table 6.1: List of all samples showing Ga flux (Φ_{Ga}), ammonia flow rate, substrate temperature (T_{sub}), substrate TDD, and rms roughness value (r_{rms}).

on both samples appears comparably smooth (see Fig6.4), and the rms surface roughness values were 0.77 and 0.51 nm in 2×2 μm^2area for samples NH_3-A and NH_3-B, respectively.

Diode patterns were fabricated on the samples using conventional optical lithography. Mesa isolation was performed with a BCl_3/Cl_2 reactive ion etch. Metal stacks of Al/Au (30/300 nm) and Ni/Au (30/300 nm) were deposited by e-beam evaporation for Ohmic and Schottky contacts, respectively.

Results and discussion

On each sample 16 diodes with 8 different areas (between 100 and 3636 μm^2) were measured on two different dies. Some variations in the leakage current density were observed from diode to diode on each sample but there was no correlation between

these variations and the diode size.

To properly consider these variations while comparing the leakage current between samples, we took a logarithmic average of the leakage current on all diodes for each sample, given by Eq6.1:

$$\log\left(J_{avg}(V)\right) = 1/N \sum \log\left(J_i\left(V\right)\right) \tag{6.1}$$

,

where $J_i(V)$ is the reverse current on diode i at voltage V and N is the number of diodes measured on each sample. This method was used to calculate the average current because the leakage current can vary by several orders of magnitude from diode to diode, and the data are usually plotted on a semilog scale. Logarithmic averaging provides a more accurate picture of current variations on this scale.

The error bars were defined by calculating the standard deviation of the currents using the following relation:

$$\sigma(V) = exp\left(\sqrt{1/N \sum \left(\log(J_i) - \log(J_{avg})\right)^2}\right) \tag{6.2}$$

.

The average leakage currents on all samples at a reverse bias of -5V are shown in Fig6.5.

Among samples grown by PAMBE on GaN-on-sapphire templates, PA-C has the highest average leakage current. As mentioned previously, this sample was grown in a regime close to stoichiometry, and the surface was not covered with a Ga wetting layer during growth. Secondary ion mass spectroscopy (SIMS) mea-

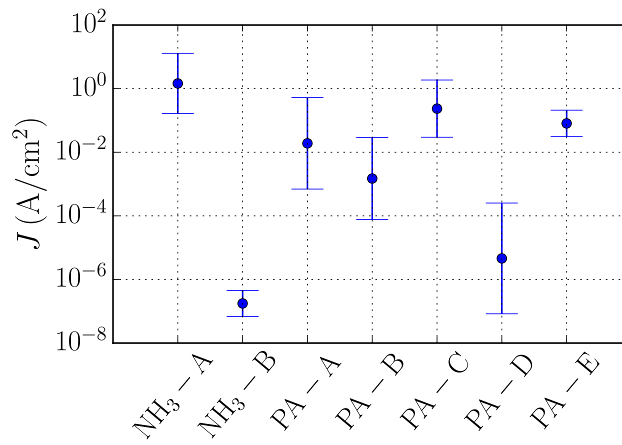

Figure 6.5: Average leakage current at -5 V. The error bars show the variation of leakage current over 16 devices for each sample.

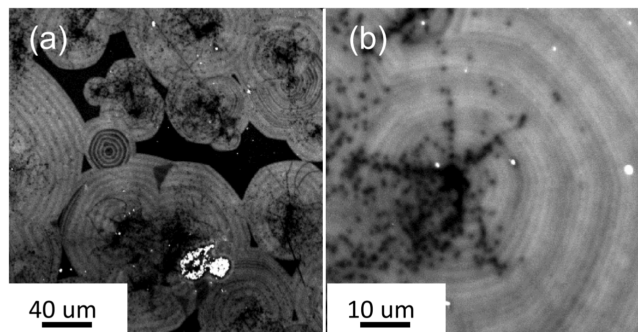

Figure 6.6: 10 kV panchromatic Cathodoluminescence (CL) images taken on a Lumilog FS GaN substrate showing the non-uniform distribution of the dislocation density.

surements on GaN have demonstrated that the presence of a Ga wetting layer on the surface helps to reduce background oxygen incorporation into the crystal during growth. Therefore, it is likely that the oxygen impurity concentration in this sample is higher than the others. Furthermore, oxygen behaves as a shallow donor in GaN, leading to additional band bending in the UID layer, and consequently, higher leakage currents. Comparison between the result of capacitance versus voltage (CV) measurements on sample PA-A, PA-B, and PA-C confirms this hypothesis. The charge density in the UID layer was measured to be 8.6×10^{16} cm^{-3}, 8.4×10^{16} cm^{-3}, and 4.4×10^{17} cm^{-3}on sample PA-A, PA-B, and PA-C, respectively. Therefore, the charge density is almost one order of magnitude higher for sample PA-C in comparison with samples PA-A, and PA-B.

Samples PA-A and PA-E were grown with the same conditions, except that for sample PA-A the growth was interrupted every 10 minutes while for sample PA-E there was no interruption during growth. The average leakage currents on these two samples are very similar. However, there is a larger variation in the leakage current on sample PA-A compared to sample PA-E. As mentioned before, the Ga desorption from the surface was observed via changes in the RHEED pattern intensity. The electron beam in RHEED is directed towards the sample at a grazing angle, and the pattern represents an average of a large sample area. Because of temperature non-uniformity on the substrate, the amount of time required to desorb the excess Ga from the surface varies with location on the sample. Therefore, although according to RHEED, 30 seconds was sufficient to completely desorb the surface Ga, in certain areas excess Ga remains on the surface, and in others, the surface was left without any Ga wetting layer during interruptions, resulting

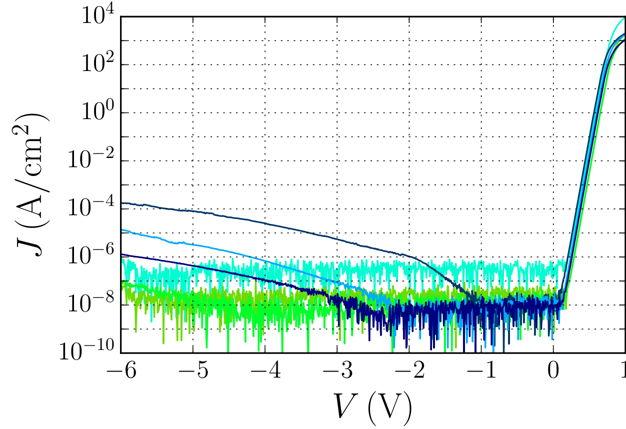

Figure 6.7: Current-voltage curves on diodes fabricated on the Schottky structure grown on Lumilog FS GaN, illustrating the variation in the reverse current from diode to diode. The idiealty factor of these diodes was 1.02 at room temperature.

in a higher oxygen incorporation. Sample PA-B has the lowest average leakage current among samples grown on GaN-on-sapphire substrates using PAMBE. It has previously been shown [95] that growing in Ga-lean conditions helps to reduce the reverse leakage current. However, this introduces pits on the surface, which are not desirable in complicated device structures. Growing in the intermediate regime helps to obtain a pit-free surface while still minimizing the leakage current.

Sample PA-D, which is grown on Lumilog FS GaN, has the largest RLC variations. This may be attributed to the large non-uniformity in dislocation density on the sample, as seen in the cathodoluminescense (CL) image in Fig6.6. The current-voltage (IV) curves for different diodes on sample PA-D is shown in Fig6.7. These diodes had an ideality factor close to 1 (1.02) at room temperature. Diodes with higher leakage currents are very likely those fabricated on areas with higher dislocation density.

Among samples grown by ammonia, sample NH_3-A, which is grown using 200

sccm of ammonia, has the larges high leakage current among all samples, including those grown by PA-MBE. On the other hand, the sample grown with 1000 sccm (NH_3-B) has the lowest and the most uniform leakage. The high leakage on sample NH_3-A may be attributed to the shallow electron trap level at 0.24 eV below the conduction band edge. This trap level is related to the N vacancies and Arehart *et al.*[110]. have shown that the density of this trap level is reduced at higher V/III ratios.

Conclusion

In conclusion, we have shown that by growing in an intermediate III-V ratio regime, we are able to decrease the average reverse leakage current by one order of magnitude, and still have a smooth and pit-free surface. We have also shown that growing by ammonia MBE in a N-rich regime does not always result in lower leakage than PAMBE growth in Ga-rich regime. On the contrary, growing with 200 sccm ammonia results in Schottky diodes with higher leakage current than samples grown by PAMBE. Finally, increasing the ammonia flow to 1000 sccm results in better Schottky diode leakage characteristics than PAMBE devices.

Bibliography

[1] Hadis Morkoc. *Handbook of Nitride Semiconductors and Devices, Materials Properties, Physics and Growth.* John Wiley and Sons, 2009.

[2] Lin Zhou, David J. Smith, Martha R. McCartney, D. S. Katzer, and D. F. Storm. Observation of vertical honeycomb structure in InAlN/GaN heterostructures due to lateral phase separation. *Applied Physics Letters*, 90(8):081917, 2007.

[3] S.-L. Sahonta, G. P. Dimitrakopulos, Th. Kehagias, et al. Mechanism of compositional modulations in epitaxial InAlN films grown by molecular beam epitaxy. *Applied Physics Letters*, 95(2):021913, 2009.

[4] Soojeong Choi, Feng Wu, Ravi Shivaraman, Erin C. Young, and James S. Speck. Observation of columnar microstructure in lattice-matched InAlN/GaN grown by plasma assisted molecular beam epitaxy. *Applied Physics Letters*, 100(23):232102, 2012.

[5] Stacia Keller, Haoran Li, Matthew Laurent, et al. Recent progress in metal-organic chemical vapor deposition of N-polar group-III nitrides. *Semiconductor Science and Technology*, 29(11):113001, November 2014.

[6] Stephen W Kaun, Man Hoi Wong, Umesh K Mishra, and James S Speck. Molecular beam epitaxy for high-performance Ga-face GaN electron devices. *Semiconductor Science and Technology*, 28(7):074001, July 2013.

[7] Raymond S. Pengelly, Simon M. Wood, James W. Milligan, Scott T. Sheppard, and William L. Pribble. A Review of GaN on SiC High Electron-Mobility Power Transistors and MMICs. *IEEE Transactions on Microwave Theory and Techniques*, 60(6):1764–1783, June 2012.

[8] Shuji Nakamura, Masayuki Senoh, Shin-ichi Nagahama, et al. InGaN/GaN/AlGaN-Based Laser Diodes with Modulation-Doped Strained-Layer Superlattices. *Japanese Journal of Applied Physics*, 36(Part 2, No. 12A):L1568–L1571, December 1997.

[9] Shuji Nakamura, Masayuki Senoh, Shin-ichi Nagahama, et al. InGaN/GaN/AlGaN-based laser diodes with modulation-doped strained-layer superlattices grown on an epitaxially laterally overgrown GaN substrate. *Applied Physics Letters*, 72(2):211, January 1998.

[10] Shuji Nakamura, Masayuki Senoh, Shin-ichi Nagahama, et al. Violet InGaN/GaN/AlGaN-Based Laser Diodes with an Output Power of 420 mW. *Japanese Journal of Applied Physics*, 37(Part 2, No. 6A):L627–L629, June 1998.

[11] Mathew C. Schmidt, Kwang-Choong Kim, Robert M. Farrell, et al. Demonstration of Nonpolar m-Plane InGaN/GaN Laser Diodes. *Japanese Journal of Applied Physics*, 46(No. 9):L190–L191, February 2007.

[12] J. J. Wierer, M. R. Krames, J. E. Epler, et al. InGaN/GaN quantum-well heterostructure light-emitting diodes employing photonic crystal structures. *Applied Physics Letters*, 84(19):3885, April 2004.

[13] Shuji Nakamura. GaN Growth Using GaN Buffer Layer. *Japanese Journal of Applied Physics*, 30(Part 2, No. 10A):L1705–L1707, October 1991.

[14] Shuji Nakamura, Masayuki Senoh, and Takashi Mukai. P-GaN/N-InGaN/N-GaN Double-Heterostructure Blue-Light-Emitting Diodes. *Japanese Journal of Applied Physics*, 32(Part 2, No.1A/B):L8–L11, January 1993.

[15] T. Palacios, A. Chakraborty, S. Rajan, et al. High-power AlGaN/GaN HEMTs for Ka-band applications. *IEEE Electron Device Letters*, 26(11):781–783, November 2005.

[16] U.K. Mishra and T.E. Kazior. GaN-Based RF Power Devices and Amplifiers. *Proceedings of the IEEE*, 96(2):287–305, February 2008.

[17] S. Karmalkar and U.K. Mishra. Enhancement of breakdown voltage in AlGaN/GaN high electron mobility transistors using a field plate. *IEEE Transactions on Electron Devices*, 48(8):1515–1521, 2001.

[18] Brianna S. Eller, Jialing Yang, and Robert J. Nemanich. Electronic surface and dielectric interface states on GaN and AlGaN. *Journal of Vacuum Science & Technology A: Vacuum, Surfaces, and Films*, 31(5):050807, June 2013.

[19] H. P. Maruska. THE PREPARATION AND PROPERTIES OF VAPOR-

DEPOSITED SINGLE-CRYSTAL-LINE GaN. *Applied Physics Letters*, 15(10):327, October 1969.

[20] H. Amano, N. Sawaki, I. Akasaki, and Y. Toyoda. Metalorganic vapor phase epitaxial growth of a high quality GaN film using an AlN buffer layer. *Applied Physics Letters*, 48(5):353, February 1986.

[21] S. Kolluri, S. Keller, S. P. DenBaars, and U.K. Mishra. N-Polar AlGaN/GaN MIS-HEMTs on SiC with a 16.7 W/mm power density at 10 GHz using an Al 2O 3 based etch stop technology for the gate recess. In *69th Annual Device Research Conference (DRC)*, pages 2015–16, Santa Barbara, 2011. IEEE, Piscataway, NJ, USA.

[22] V. Zomorrodian, U. K. Mishra, and R.A. York. A High-efficiency class F MMIC power amplifier at 4.0 GHz using AlGaN/GaN HEMT technology. In *IEEE Compound Semiconductor Integrated Circuit Symposium (CSICS)*, page 4 pp., La Jolla, 2012. IEEE, Piscataway, NJ, USA.

[23] Srabanti Chowdhury and Umesh K Mishra. Lateral and Vertical Transistors Using the AlGaN/GaN Heterostructure. *IEEE Transactions on Electron Devices*, 60(10):3060–3066, October 2013.

[24] D. Denninghoff, J. Lu, E. Ahmadi, S. Keller, and U.K. Mishra. N-polar GaN/InAlN/AlGaN MIS-HEMTs with 1.89 S/mm extrinsic transconductance, 4 A/mm drain current, 204 GHz f T and 405 GHz f max. In *71st Annual Device Research Conference (DRC)*, pages 197–8. IEEE, Piscataway, NJ, USA, 2013.

[25] T. Palacios, A. Chakraborty, S. Heikman, et al. AlGaN/GaN high electron mobility transistors with InGaN back-barriers. *IEEE Electron Device Letters*, 27(1):13–15, January 2006.

[26] S. Dasgupta, D. F. Brown, J. S. Speck, and U. K. Mishra. Scaling behavior and velocity enhancement in self-aligned N-polar GaN/AlGaN HEMTs with maximum fT of 163 GHz. In *69th Device Research Conference*, pages 141–142. IEEE, June 2011.

[27] S. Keller, G. Parish, J.J. Xu, et al. Gallium nitride based high power heterojunction field effect transistors: process development and present status at UCSB. *IEEE Transactions on Electron Devices*, 48(3):552–559, March 2001.

[28] Bin Lu and Tomas Palacios. High Breakdown (1500 V) AlGaN/GaN HEMTs by Substrate-Transfer Technology. *IEEE Electron Device Letters*, 31(9):951–953, September 2010.

[29] U.K. Mishra and P. Parikh. AlGaN/GaN HEMTs-an overview of device operation and applications. *Proceedings of the IEEE*, 90(6):1022–1031, June 2002.

[30] C. Lee, L. Witkowski, H.-Q. Tserng, et al. Effects of AlGaN/GaN HEMT structure on RF reliability. *Electronics Letters*, 41(3):155, 2005.

[31] K. S. Kim, A. Saxler, P. Kung, M. Razeghi, and K. Y. Lim. Determination of the band-gap energy of AlInN grown by metal-organic chemical-vapor deposition. *Applied Physics Letters*, 71(6):800, August 1997.

[32] David F Brown, Stacia Keller, Steven P DenBaars, and Umesh K Mishra. N-Polar InAlN/AlN/GaN MIS-HEMTs. *IEEE Electron Device Letters*, 31(8):800–802, August 2010.

[33] Jing Lu, Dan Denninghoff, Ramya Yeluri, et al. Very high channel conductivity in ultra-thin channel N-polar GaN/(AlN, InAlN, AlGaN) high electron mobility hetero-junctions grown by metalorganic chemical vapor deposition. *Applied Physics Letters*, 102(23):232104, 2013.

[34] Jia Guo, Yu Cao, Chuanxin Lian, et al. Metal-face InAlN/AlN/GaN high electron mobility transistors with regrown ohmic contacts by molecular beam epitaxy. *Physica Status Solidi (a)*, 208(7):1617–1619, July 2011.

[35] Man Hoi Wong, Feng Wu, Christophe a. Hurni, et al. Molecular beam epitaxy of InAlN lattice-matched to GaN with homogeneous composition using ammonia as nitrogen source. *Applied Physics Letters*, 100(7):072107, 2012.

[36] Stephen W. Kaun, Peter G. Burke, Man Hoi Wong, et al. Effect of dislocations on electron mobility in AlGaN/GaN and AlGaN/AlN/GaN heterostructures. *Applied Physics Letters*, 101(26):262102, December 2012.

[37] Baishakhi Mazumder, Stephen W. Kaun, Jing Lu, et al. Atom probe analysis of AlN interlayers in AlGaN/AlN/GaN heterostructures. *Applied Physics Letters*, 102(11):111603, March 2013.

[38] Sansaptak Dasgupta, Soojeong Choi, Feng Wu, James S. Speck, and Umesh K. Mishra. Growth, Structural, and Electrical Characterizations of

N-Polar InAlN by Plasma-Assisted Molecular Beam Epitaxy. *Applied Physics Express*, 4(4):045502, March 2011.

[39] B P Geiser, D J Larson, S S A Gerstl, et al. A System for Simulation of Tip Evolution Under Field Evaporation. *Microsc Microanal*, 15(Suppl 2):302–303, 2009.

[40] M. Tchernycheva, L. Nevou, L. Doyennette, et al. Systematic experimental and theoretical investigation of intersubband absorption in GaN-InAlN quantum wells. *Physical Review B*, 73(12):125347, March 2006.

[41] Elaheh Ahmadi, Ravi Shivaraman, Feng Wu, et al. Elimination of columnar microstructure in N-face InAlN, lattice-matched to GaN, grown by plasma-assisted molecular beam epitaxy in the N-rich regime. *Applied Physics Letters*, 104(7):072107, February 2014.

[42] S. Keller, C. S. Suh, N. A. Fichtenbaum, et al. Influence of the substrate misorientation on the properties of N-polar InGaN/GaN and AlGaN/GaN heterostructures. *Journal of Applied Physics*, 104(9):093510, November 2008.

[43] P. Kung, C. J. Sun, A. Saxler, H. Ohsato, and M. Razeghi. Crystallography of epitaxial growth of wurtzite-type thin films on sapphire substrates. *Journal of Applied Physics*, 75(9):4515, May 1994.

[44] J. L. Lyons, A. Janotti, and C. G. Van de Walle. Carbon impurities and the yellow luminescence in GaN. *Applied Physics Letters*, 97(15):152108, October 2010.

[45] A. Armstrong, A. R. Arehart, B. Moran, et al. Impact of carbon on trap states in n-type GaN grown by metalorganic chemical vapor deposition. *Applied Physics Letters*, 84(3):374, January 2004.

[46] Stephen W. Kaun, Man Hoi Wong, Sansaptak Dasgupta, et al. Effects of Threading Dislocation Density on the Gate Leakage of AlGaN/GaN Heterostructures for High Electron Mobility Transistors. *Applied Physics Express*, 4(2):024101, January 2011.

[47] S. Keller, C. S. Suh, Z. Chen, et al. Properties of N-polar AlGaN/GaN heterostructures and field effect transistors grown by metalorganic chemical vapor deposition. *Journal of Applied Physics*, 103(3):033708, February 2008.

[48] Masanori Shinohara and Naohisa Inoue. Behavior and mechanism of step bunching during metalorganic vapor phase epitaxy of GaAs. *Applied Physics Letters*, 66(15):1936, April 1995.

[49] Mina Yoon, Ho Lee, Wei Hong, et al. Dynamics of Step Bunching in Heteroepitaxial Growth on Vicinal Substrates. *Physical Review Letters*, 99(5):055503, August 2007.

[50] K. Hiramoto, T. Tsuchiya, M. Sagawa, and K. Uomi. Multistep formation and lateral variation in the In composition in InGaAs layers grown by metalorganic vapor phase epitaxy on (001) vicinal GaAs substrates. *Journal of Crystal Growth*, 145(1-4):133–139, December 1994.

[51] Jing Lu, Xun Zheng, Matthew Guidry, et al. Engineering the (In, Al, Ga)N back-barrier to achieve high channel-conductivity for extremely scaled

channel-thicknesses in N-polar GaN high-electron-mobility-transistors. *Applied Physics Letters*, 104(9):092107, March 2014.

[52] Michael Grundmann. BandEng.

[53] Yifei Zhang, I. P. Smorchkova, C. R. Elsass, et al. Charge control and mobility in AlGaN/GaN transistors: Experimental and theoretical studies. *Journal of Applied Physics*, 87(11):7981, June 2000.

[54] Alex Q Huang. New unipolar switching power device figures of merit. *Electron Device Letters, IEEE*, 25(5):298–301, 2004.

[55] Debdeep Jena, Arthur C. Gossard, and Umesh K. Mishra. Dislocation scattering in a two-dimensional electron gas. *Applied Physics Letters*, 76(13):1707, 2000.

[56] D Jena, I Smorchkova, AC Gossard, and UK Mishra. Electron Transport in III–V Nitride Two-Dimensional Electron Gases. *physica status solidi (b)*, 228(2):617–619, 2001.

[57] M. Gurusinghe, S. Davidsson, and T. Andersson. Two-dimensional electron mobility limitation mechanisms in AlxGa1-xN/GaN heterostructures. *Physical Review B*, 72(4):045316, July 2005.

[58] D Zanato, S Gokden, N Balkan, BK Ridley, and WJ Schaff. The effect of interface-roughness and dislocation scattering on low temperature mobility of 2D electron gas in GaN/AlGaN. *Semiconductor science and technology*, 19(3):427, 2004.

[59] Uttam Singisetti, Man Hoi Wong, and Umesh K Mishra. Interface roughness scattering in ultra-thin N-polar GaN quantum well channels. *Applied Physics Letters*, 101(1):012101, 2012.

[60] David F. Brown, Siddharth Rajan, Stacia Keller, et al. Electron mobility in N-polar GaN/AlGaN/GaN heterostructuress. *Applied Physics Letters*, 93(4):042104, 2008.

[61] EJ Miller, XZ Dang, HH Wieder, et al. Trap characterization by gate-drain conductance and capacitance dispersion studies of an AlGaN/GaN heterostructure field-effect transistor. *Journal of applied physics*, 87(11):8070–8073, 2000.

[62] William M Waller, Serge Karboyan, Michael J Uren, et al. Interface State Artefact in Long Gate-Length AlGaN/GaN HEMTs. *IEEE Transaction on Electron Devices*, 62(8):2464, 2015.

[63] H. Sakaki, T. Noda, K. Hirakawa, M. Tanaka, and T. Matsusue. Interface roughness scattering in GaAs/AlAs quantum wells. *Applied Physics Letters*, 51(23):1934, 1987.

[64] B Gelmont, K Kim, and M Shur. Monte Carlo simulation of electron transport in gallium nitride. *Journal of applied physics*, 74(3):1818–1821, 1993.

[65] BL Gelmont, M Shur, and M Stroscio. Polar optical-phonon scattering in three-and two-dimensional electron gases. *Journal of applied physics*, 77(2):657–660, 1995.

[66] John H. Davies. *The Physics of Low-dimensional Semiconductors: An Introduction.* Cambridge University Press, 1998.

[67] Shinya Yamakawa, Hiroaki Ueno, Kenji Taniguchi, et al. Study of interface roughness dependence of electron mobility in Si inversion layers using the Monte Carlo method. *Journal of applied physics*, 79(2):911–916, 1996.

[68] Jing. *Design and Epitaxial Growth of Ultra-scaled N-polar GaN/(In, Al, Ga) N HEMTs by Metal Organic Chemical Deposition and Device Characterization.* PhD thesis, UC-Santa Barbara, 2014.

[69] Gerald Bastard. *Wave mechanics applied to semiconductor heterostructures.* Les Editions de Physique, 1988.

[70] David F. Brown. *Growth of nitrogen-polar gallium nitride-based materials and high electron mobility transistors by metal organic chemical vapor deposition.* PhD thesis, UC-Santa Barbara, 2010.

[71] Man Hoi Wong, Uttam Singisetti, Jing Lu, James S Speck, and Umesh K Mishra. Anomalous output conductance in N-polar GaN high electron mobility transistors. *Electron Devices, IEEE Transactions on*, 59(11):2988–2995, 2012.

[72] Hisham S Haddara and Mohamed El-Sayed. Conductance technique in MOSFETs: Study of interface trap properties in the depletion and weak inversion regimes. *Solid-state electronics*, 31(8):1289–1298, 1988.

[73] Sansaptak Dasgupta, Jing Lu, James S. Speck, and Umesh K. Mishra. Self-Aligned N-Polar GaN/InAlN MIS-HEMTs With Record Extrinsic Transcon-

ductance of 1105 mS/mm. *IEEE Electron Device Letters*, 33(6):794–796, June 2012.

[74] A. Asgari, S. Babanejad, and L. Faraone. Electron mobility, Hall scattering factor, and sheet conductivity in AlGaN/AlN/GaN heterostructures. *Journal of Applied Physics*, 110(11):113713, December 2011.

[75] Fukunobu Oosaka, Takuo Sugano, Yoichi Okabe, and Yutaka Okada. Scattering of Electrons by Potential Clusters in Ternary Alloy Semiconductor. *Japanese Journal of Applied Physics*, 15(12):2371–2380, December 1976.

[76] Arlyn Asch and George Hall. Quantum Theory of the Residual Electrical Resistivity of Disordered Alloys. *Physical Review*, 132(3):1047–1057, November 1963.

[77] Changbo Liu, Guijuan Zhao, Guipeng Liu, et al. Scattering due to large cluster embedded in quantum wells. *Applied Physics Letters*, 102(5):052105, 2013.

[78] Gregg H. Jessen, Robert C. Fitch, James K. Gillespie, et al. Short-Channel Effect Limitations on High-Frequency Operation of AlGaN/GaN HEMTs for T-Gate Devices. *IEEE Transactions on Electron Devices*, 54(10):2589–2597, October 2007.

[79] S. Arulkumaran, T. Egawa, H. Ishikawa, and T. Jimbo. Characterization of different-Al-content AlxGa1-xN/GaN heterostructures and high-electron-mobility transistors on sapphire. *Journal of Vacuum Science & Technology B: Microelectronics and Nanometer Structures*, 21(2):888, 2003.

[80] Guowang Li, Yu Cao, Huili Grace Xing, and Debdeep Jena. High mobility two-dimensional electron gases in nitride heterostructures with high Al composition AlGaN alloy barriers. *Applied Physics Letters*, 97(22):222110, 2010.

[81] Han Wang, Jinwook W Chung, Xiang Gao, Shiping Guo, and Tomas Palacios. High Performance InAlN / GaN HEMTs on SiC Substrate. In *CS MANTECH conference*, pages 4–7, Portland, Oregan, USA, 2010.

[82] Nabil Dawahre, Gang Shen, Steven N. Renfrow, Seongsin M. Kim, and Patrick Kung. Atom probe tomography of AlInN/GaN HEMT structures. *Journal of Vacuum Science & Technology B: Microelectronics and Nanometer Structures*, 31(4):041802, 2013.

[83] S. Goodnick, D. Ferry, C. Wilmsen, et al. Surface roughness at the Si(100)-SiO2 interface. *Physical Review B*, 32(12):8171–8186, December 1985.

[84] Charles Kittel. *Quantum theory of solids.* Wiley, 2nd edition, 1963.

[85] S. Das Sarma and E. H. Hwang. Short-range disorder effects on electronic transport in two-dimensional semiconductor structures. *Physical Review B*, 89(12):121413, March 2014.

[86] David K. Ferry, Stephen M. Goodnick, and Jonathan Bird. *Transport in Nanostructures.* Cambridge University Press, 2009.

[87] I P Smorchkova, C R Elsass, J P Ibbetson, et al. Polarization-induced charge and electron mobility in AlGaN / GaN heterostructures grown by plasma-

assisted molecular-beam epitaxy. *Journal of Applied Physics*, 86(8):4520–4526, 1999.

[88] Stephen W Kaun, Elaheh Ahmadi, Baishakhi Mazumder, et al. GaN-based high-electron-mobility transistor structures with homogeneous lattice-matched InAlN barriers grown by plasma-assisted molecular beam epitaxy. *Semiconductor Science and Technology*, 29(4):045011, April 2014.

[89] Stephen W. Kaun, Man Hoi Wong, Umesh K. Mishra, and James S. Speck. Correlation between threading dislocation density and sheet resistance of AlGaN/AlN/GaN heterostructures grown by plasma-assisted molecular beam epitaxy. *Applied Physics Letters*, 100(26):262102, June 2012.

[90] L. McCarthy, I. Smorchkova, H. Xing, et al. Effect of threading dislocations on AlGaN/GaN heterojunction bipolar transistors. *Applied Physics Letters*, 78(15):2235, April 2001.

[91] Yu Saitoh, Kazuhide Sumiyoshi, Masaya Okada, et al. Extremely Low On-Resistance and High Breakdown Voltage Observed in Vertical GaN Schottky Barrier Diodes with High-Mobility Drift Layers on Low-Dislocation-Density GaN Substrates. *Applied Physics Express*, 3(8):081001, July 2010.

[92] Donald J. Suntrup, Geetak Gupta, Haoran Li, Stacia Keller, and Umesh K. Mishra. Measurement of the hot electron mean free path and the momentum relaxation rate in GaN. *Applied Physics Letters*, 105(26):263506, December 2014.

[93] Geetak Gupta, Elaheh Ahmadi, Karine Hestroffer, Edwin Acuna, and

Umesh K. Mishra. Common Emitter Current Gain >1 in III-N Hot Electron Transistors With 7-nm GaN/InGaN Base. *IEEE Electron Device Letters*, 36(5):439–441, May 2015.

[94] E. G. Brazel, M. a. Chin, and V. Narayanamurti. Direct observation of localized high current densities in GaN films. *Applied Physics Letters*, 74(16):2367, 1999.

[95] J. W. P. Hsu, M. J. Manfra, D. V. Lang, et al. Inhomogeneous spatial distribution of reverse bias leakage in GaN Schottky diodes. *Applied Physics Letters*, 78(12):1685, 2001.

[96] J. W. P. Hsu, M. J. Manfra, S. N. G. Chu, et al. Effect of growth stoichiometry on the electrical activity of screw dislocations in GaN films grown by molecular-beam epitaxy. *Applied Physics Letters*, 78(25):3980, 2001.

[97] J. W. P. Hsu, M. J. Manfra, R. J. Molnar, B. Heying, and J. S. Speck. Direct imaging of reverse-bias leakage through pure screw dislocations in GaN films grown by molecular beam epitaxy on GaN templates. *Applied Physics Letters*, 81(1):79, 2002.

[98] John E. Northrup. Screw dislocations in GaN: The Ga-filled core model. *Applied Physics Letters*, 78(16):2288, April 2001.

[99] E. J. Miller, D. M. Schaadt, E. T. Yu, et al. Reduction of reverse-bias leakage current in Schottky diodes on GaN grown by molecular-beam epitaxy using surface modification with an atomic force microscope. *Journal of Applied Physics*, 91(12):9821, 2002.

[100] E. J. Miller, D. M. Schaadt, E. T. Yu, et al. Reverse-bias leakage current reduction in GaN Schottky diodes by electrochemical surface treatment. *Applied Physics Letters*, 82(8):1293, 2003.

[101] N. Grandjean, M. Leroux, J. Massies, M. Mesrine, and M. Laugt. Molecular Beam Epitaxy of GaN under N-rich Conditions using NH3. *Japenese Journal of Applied Physics*, 38(2A):618–621, 1999.

[102] A. L. Corrion, F. Wu, and J. S. Speck. Growth regimes during homoepitaxial growth of GaN by ammonia molecular beam epitaxy. *Journal of Applied Physics*, 112(5):054903, September 2012.

[103] Stephen W Kaun, Baishakhi Mazumder, Micha N Fireman, et al. Pure AlN layers in metal-polar AlGaN/AlN/GaN and AlN/GaN heterostructures grown by low-temperature ammonia-based molecular beam epitaxy. *Semiconductor Science and Technology*, 30(5):055010, May 2015.

[104] Erin C. H. Kyle, Stephen W. Kaun, Peter G. Burke, et al. High-electron-mobility GaN grown on free-standing GaN templates by ammonia-based molecular beam epitaxy. *Journal of Applied Physics*, 115(19):193702, May 2014.

[105] G. Koblmu?ller, S. Ferna?ndez-Garrido, E. Calleja, and J. S. Speck. In situ investigation of growth modes during plasma-assisted molecular beam epitaxy of (0001) GaN. *Applied Physics Letters*, 91(16):161904, October 2007.

[106] C. Adelmann, J. Brault, D. Jalabert, et al. Dynamically stable gallium

surface coverages during plasma-assisted molecular-beam epitaxy of (0001) GaN. *Journal of Applied Physics*, 91(12):9638, May 2002.

[107] A. R. Smith. Wurtzite GaN surface structures studied by scanning tunneling microscopy and reflection high energy electron diffraction. *Journal of Vacuum Science & Technology A: Vacuum, Surfaces, and Films*, 16(3):1641, May 1998.

[108] C. Poblenz, P. Waltereit, and J. S. Speck. Uniformity and control of surface morphology during growth of GaN by molecular beam epitaxy. *Journal of Vacuum Science & Technology B: Microelectronics and Nanometer Structures*, 23(4):1379, July 2005.

[109] J.R. Lang and J.S. Speck. NH3-rich growth of InGaN and InGaN/GaN superlattices by NH3-based molecular beam epitaxy. *Journal of Crystal Growth*, 346(1):50–55, May 2012.

[110] a. R. Arehart, a. Corrion, C. Poblenz, et al. Deep level optical and thermal spectroscopy of traps in n-GaN grown by ammonia molecular beam epitaxy. *Applied Physics Letters*, 93(11):112101, 2008.